Seismic monitoring of CO_2 sequestration – effects of saturation, pressure and temperature

Vegard Michael Solheim

Thesis for the degree
Master of Science

Department of Earth Science

University of Bergen

June 2021

Abstract

Time-lapse seismic monitoring of carbon sequestration at Sleipner has revealed the seismic signature of injecting CO_2 into the shallow Utsira reservoir. Several bright spot anomalies have occurred within the reservoir unit on the seismic image due to the elevated acoustic impedance contrast between the softer gas sands and stiffer intra-layering shales overlaying and blocking the upward migration of the injected CO_2. Based on the fact that Utsira represents a thick and highly porous reservoir, the seismic reflections and amplitudes are highly sensitive to fluid saturation. As a result, amplitude anomalies are abnormally strong and exclusively influenced by gas injections and less by temperature or pressure alternations for shallow, highly porous and unconsolidated sandstone reservoirs.

Seismic attributes have been used to evaluate and provide more certainty to the seismic interpretation, as the attributes are able to correlate the observed amplitude changes to changes in lithology, fluid type and saturation, porosity and pressure. Amplitude versus offset (AVO) and bright spot analysis, intercept versus gradient crossplot, and rock physics templates (RPT) represent the seismic attributes presented in this thesis. The attributes are derived from a calibrated rock physics model (RPM) and proves the importance of RPM's role of linking geology to geophysical responses to obtain accurate and representative results.

This thesis also presents synthetic responses to various hypothetical geological scenarios related to carbon sequestration, thus providing a wider understanding of how seismic reflections and amplitudes might vary laterally or vertically from well log measurements, or for other carbon storage projects with a slightly different geological setting than Utsira.

This work demonstrates the importance of understanding rock physics to connect seismic data to geology. It also shows the value of calibrating usable well log data when creating an RPM. Ultimately, the benefit of doing rock physics modelling as well as seismic modelling and use attributes to aid the interpretation and improve the understanding of time-lapse effects regarding CO_2 sequestration.

Acknowledgements

During the master's degree I have received excellent supervision from Prof. Tor Arne Johansen and Dr. Erling Hugo Jensen. All the feedback and sessions with discussions have really improved my understanding and knowledge within this field of work, and I would like to express my gratitude to both of you.
I would also like to thank Dr. Bent Ole Ruud for technical assistance related to various software -and VPN-connection issues.

I am also grateful for the social environment among fellow students at the Department of Earth Science, and I have really appreciated the cooperation and discussions with Sondre Kåstad throughout this thesis.

Finally, I greatly appreciate the support of my girlfriend, family and friends throughout my studies.

Table of Contents

1 Introduction

1.1 Motivation

According to the Intergovernmental Panel on Climate Change (2013), the atmospheric concentration of important greenhouse gases such as carbon dioxide and methane have increased extensively during the last decades, resulting in a global warming. IPCC (2014) states that the rise in greenhouse gas emissions is caused by anthropogenic activities connected to an increasing energy demand, driven by economic and population growth.

The International Energy Agency (2019) reports that 70% of the energy demand was met by the consumption of non-renewable fossil fuels, accounting for 33.1 Gt of CO_2 emissions to the atmosphere in 2018. In accordance with a constantly growing population striving for better livelihoods, the need for substantial amounts of energy will be essential and crucial in the future, thus the trend of the atmospheric CO_2 content is less likely to change without mitigating actions. The trend can be observed on the graph published by NASA (2020) (Figure 1.1).

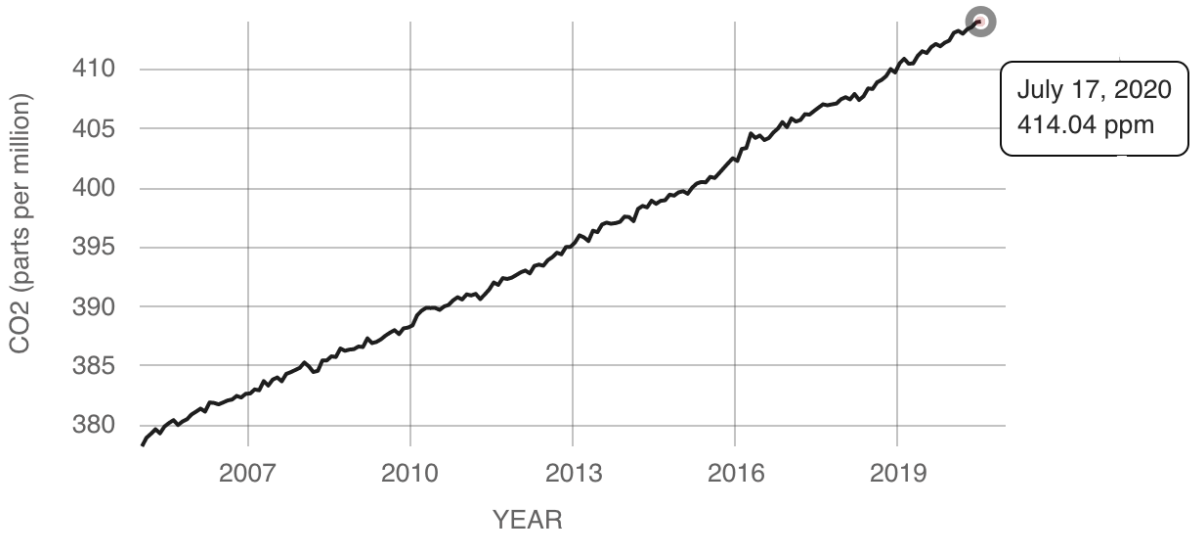

Figure 1.1: A graph illustrating atmospheric carbon dioxide concentration as a function of years at Mauna Loa (Hawaii). The concentration of carbon dioxide is given in parts per million (ppm), ranging from 378 ppm in Jan. 2005 to 414ppm in Jul. 2020 respectively. Source: NASA (2020).

Renewable energy is commonly understood to be the main solution to diminish anthropogenic greenhouse gas emissions. However, the business is immature in terms of compensating for the energy currently provided by the carbonized industry. Hence, there is a need for technological and innovative mitigating measures which decrease the anthropogenic carbon footprint without hindering the supply of energy.

Carbon Capture and Storage (CCS) is considered a solution to reduce the anthropogenic emissions without harming the supply chain of energy, and is defined as the process were carbon dioxide emitted because of the consumption of fossil fuels is captured and permanently stored in suitable subsurface reservoirs (Herzog and Golomb, 2004).

The storage capacity for carbon dioxide on the Norwegian Continental Shelf is estimated by Equinor (2020) to be equal to a millennium of Norway's emissions. This fact indicates the commercial potential for Norwegian CCS. Reservoir characterization and time-lapse seismic monitoring of the gas injections are therefore vitally important as they are needed for safe storage by detecting possible leakages and determining favorable injection points for new wells. Both of which are needed to optimize storage capacity and efficiency (Lumley, 2010; Schlumberger, 2019; Sandø et.al, 2009).

More specifically, the benefit of time-lapse seismic monitoring involves the ability to monitor variations in pore pressure, pore fluid saturations -and contacts within the reservoirs (Landrø, M., 2010). In addition, rock physics modelling can be used to predict the seismic response of a fluid substitution of a reservoir (e.g. CO_2 injected). It can also predict the seismic response of various hypothetical geological scenarios (Avseth et al., 2005). Hence, combining time-lapse seismic monitoring and rock physics modelling of gas injections are very useful to ensure safe and permanent storage of carbon dioxide.

Based on the fact that CCS could contribute to a more sustainable future, reducing a large share of greenhouse gas emissions from the industry and power sector through the energy transition from non-renewable to renewable energy, it is of interest to study the behaviour of carbon dioxide within a subsurface reservoir using seismic data. Accordingly, how gas injection influences rock properties under different temperature and pressure regimes and how it reflects on seismic images.

1.2 Main objectives

The main objectives of the master thesis scrutinize seismic monitoring of time-lapse data from Sleipner to demonstrate the influence of carbon dioxide on seismic reflections and amplitudes. More specifically, study how the injected gas affects physical rock properties and thus seismic attributes under different conditions, with a particular focus on CO_2 saturation, pressure and temperature.
Seismic modelling is used in this thesis to produce synthetic seismic data, as the synthetic results can be compared to real seismic data obtained from offshore surveys at Sleipner. The seismic attributes used in the thesis are calculated with respect to the calibrated rock physics model (RPM) for the Utsira reservoir.

The calibration of usable well log data and RPM is done with ENTER, a software created and developed by Rock Physics Technology. The seismic modelling is done using NORSAR, and some pre-processing of the synthetic results is done with GeoGiga.

1.3 Outline of thesis

The outline of this thesis is categorized into eight chapters, as listed below.
Chapter 1 provides the motivation for pursuing the thesis and includes the main objectives of the thesis.
Chapter 2 presents the possibilities and risks related to the sequestration of carbon dioxide, in particular CCS.
Chapter 3 provides background theory about elastic waves, rocks physics and the principle of rock physics modelling of CO_2 fluid substitution.
Chapter 4 introduces AVO analysis, direct hydrocarbon indicators and alternative seismic attributes.
Chapter 5 studies seismic signatures of CO_2 injections using numerical examples.
Chapter 6 focuses on the case study for the Sleipner Field – the injection of CO_2 in a porous sandstone reservoir and its influence on seismic data.
Chapter 7 discusses results with regards to the case study and numerical examples in the previous chapters.
Chapter 8 presents the final conclusions to the case study and thesis as a whole.

2 The process of CO2 sequestration – possibilities and risks

2.1 Outline

This chapter assesses the possibilities and risks linked with the sequestration of carbon dioxide involving climatic, social policy and economic aspects. Prior to a commercial industrial implementation of CO_2 sequestration, it is crucial that a thorough and elaborate risk assessment is done in order to delineate the possibilities and risks associated with the technology. This provides a wider perspective and understanding of the gains and challenges related to the CCS value chain.

2.2 Assessment of CO_2 sequestration – possibilities and risks

CO_2 sequestration, in particular CCS, is defined as a process were carbon dioxide that would otherwise be emitted into the atmosphere, is captured and permanently stored in porous subsurface formations (Herzog and Golomb, 2004). CCS consists of three procedures: the capture of CO_2 from flue and process gas at a facility, the transportation of CO_2 to a storage site via pipeline or ship, and finally the injection of CO_2 in a subsurface geological formation (Brown et al., 2020). The concept of carbon capture and storage is illustrated in Figure 2.1.

Carbon dioxide has been applicable to the industry for several decades regarding ammonia - and food production and enhanced oil recovery (EOR), implying that the technology of capturing carbon dioxide is widely known (Berge et al., 2016). Thus, the majority of challenges and risks related to the capture of carbon dioxide have probably been resolved. The possible capture technologies can be distinguished into three main categories, depending on which stage of the process the CO_2 is separated;

- Post-Combustion: Flue gas from a coal or gas powerplant is cooled from 80-90°C to 30-40°C with water. Further, the cooled gas is transported into an absorber tower, where the pressure decreases and the gas gets bounded to amines towards the top of the absorber tower. The resulting compound is collected at the bottom of the absorber tower and transported into a separation unit, where the carbon dioxide is separated from the amines through a heating process. This leaves pure carbon dioxide as an end product with typical capture rates of 85-90% (Berge et al., 2016).

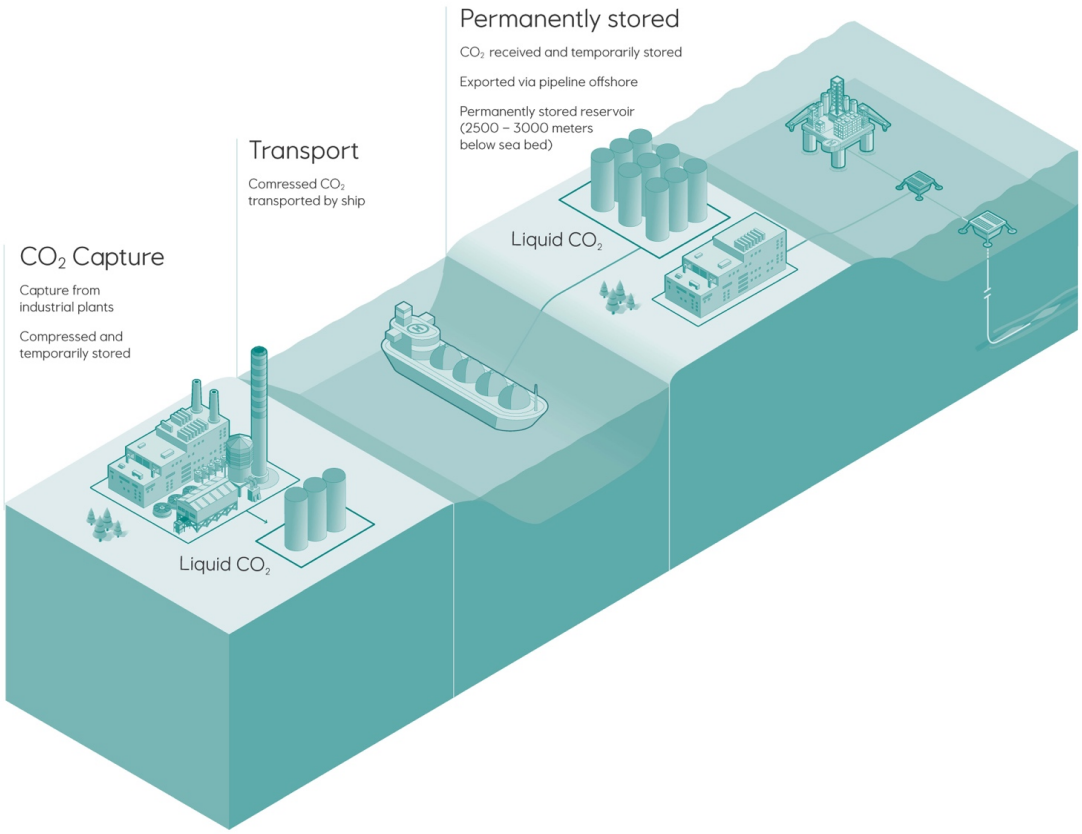

Figure 2.1: Illustration of the CCS process, from capture to subsurface storage. [1] CO_2 Capture: Capture from industrial plants, compressed and temporarily stored. [2] Transport: Compressed CO_2 transported by ship. [3] Permanently stored: CO_2 is received and exported via an offshore pipeline to the respective storage site, from where it is injected into a suitable reservoir. Source: Equinor (2019).

- Pre-Combustion: Fuel (e.g. natural gas) is mixed with water vapour and air in a reactor, chemically reforming the fuel to carbon monoxide and hydrogen under high temperature and pressure. The resulting gas is further converted to additional hydrogen as it is mixed with water after being cooled to 300°C. The carbon monoxide attaches to the oxygen in water, producing additional free hydrogen molecules. The CO_2 gets separated with amines, producing pure hydrogen and carbon dioxide as end products. The amines are reusable in both pre-combustion and post-combustion (Berge et al., 2016).
- Oxyfuel: The combustion of fuel is mixed with pure oxygen. The resulting exhaust gas consists of water vapour and carbon dioxide, which gets separated by cooling the flue gas. This condenses the water vapour into a liquid, chemically producing pure carbon dioxide as the final product (Berge et al., 2016).

Besides the possibilities of capturing carbon dioxide, a potential release or long term exposure of ammonia and amines impose the largest risk associated with the capturing process. Låg et al. (2009) state that amines linked to CCS may get degraded to different chemical compounds, posing serious hazard to human health if present in the environment. Thus, it is desirable to reduce the human exposure to these compounds. According to Solomon (2007), an exposure to pure CO_2 causes irritations to the human body and affects the human health negatively. To which extent this happens largely depends on the duration and concentration of CO_2 within a confined area. Nonetheless, it is possible to anticipate that with the extensive knowledge acquired from capturing carbon dioxide and handling hazardous chemical compounds, mitigations measures that minimize the overall risk can be implemented.

In accordance with several capture opportunities, carbon dioxide has a wide range of possibilities in terms of transportation. Road tankers, railways, pipelines or ships represent the most common ways of industrial transportation. Due to the large volumes involved in carbon sequestration, transportation via pipeline and ship is considered the best, both from a practical and economical point of view (Berge et al., 2016; Coleman et al., 2018).
According to Zero Emission Platform (2011), pipeline transportation is most beneficial for distances between 1000 – 1500 km, while a ship is preferred for larger distances, though it depends on conditions and volumes transported. Pipeline corrosion and leakage, and a potential collision, fire or stranding of a ship represent the major risks associated with the transportation of carbon dioxide. Nevertheless, these risks are considered minimal, due to the knowledge that has been acquired about the transportation of carbon dioxide via pipelines and natural gas by ships for many decades (Berge et al., 2016).

Moreover, there exists a risk related to the lack of extensive experience of transporting CO_2 through offshore pipelines over long distances. A factor that might challenge pipeline integrity, flow assurance, capital and operating cost, as well as safety and environmental factors (Onyebuchi et al., 2018). On the other hand, SINTEF has recently developed an advanced simulation model which is able to predict minor cracks or damages to pipelines that might lead to or develop into extensive fracturing. This prevents leakage and extensive damages to pipelines, providing both safe and cost-efficient transportation of CO_2 (Benjaminsen, C., 2019).
Additionally, there exists a risk regarding the lack of knowledge for large-scale transportation of CO_2 by ships. Luckily, the transport of liquefied petroleum -and natural gas (LPG & LNG)

is considered similar to large-scale CO_2 transportation, thus the risk of leakage or other hazards are significantly lowered (Berge et al, 2016). It is however important to acknowledge the fact that CO_2 behaves differently than natural gas under pressure, as a potential leakage releases ten times the amount of force compared to natural gas. This might be problematic and cause challenges in terms of safety (Benjaminsen, C., 2019). In contrast, the challenges related to the carbon dioxide transportation are not considered more comprehensive than those already encountered by hydrocarbon transportation, providing predictability and thus operational safety (Coleman et al., 2018).
Large point sources of CO_2 are also quite often clustered together within small geographical areas, making them suitable for sharing and utilizing the same pipeline infrastructure for transportation to nearby storage sites, strengthening the business' development opportunities by lowering infrastructure barrier costs (Berge et al, 2016). Similarly, the extra revenue from EOR projects could also contribute to deployment of necessary and costly infrastructure, through financing CO_2 pipelines, injection installations and power plants with CO_2 capture (Berge et al., 2016).

Besides the possibilities and risks of capturing and transporting CO_2, the largest climatic benefit of implementing CCS in the industry and power sector involves the ability to manage and artificially store substantial amounts of carbon dioxide in subsurface geological formations that would otherwise be emitted to the atmosphere and contribute to global warming (Herzog and Golomb, 2004; Berge et al., 2016). These geological formations consist of depleted oil and gas fields, saline aquifers and deep unmineable coal seams, and occur both in on -and offshore sedimentary basins (Berge et al., 2016).
The permanent storage of CO_2 makes CCS an artificial carbon sink, opening up the opportunity for energy intensive value chains to continue providing energy and delivering products to the global market without being restricted to slow down production because of climatic concerns. This is a factor which secures business growth and development throughout the energy transition from fossil fuels to renewable energy (Coninck et al., 2010; Moe et al., 2020).
Examples of energy intensive industries include refinery, coal fired power plants and the manufacturing of steel, iron and cement (Coninck et al., 2010; Berge et al., 2016).
Considering that pure CO_2 is inherent to several of the industrial processes, emissions from the manufacturing of steel and iron for instance are technically and economically hard to avoid. As these products represent the building blocks of societies, CCS becomes the only

large scale mitigation option for emission abatement from these sectors. Hence, strengthening the CCS' position commercially towards reaching the climate goals defined in the Paris Agreement (Levina et al., 2013; Coninck et al., 2010 ; Berge et al., 2016).
Nonetheless, energy intensive industries are not able to solely rely on CCS to reduce their share of emissions, but are additionally required to transform their use of energy through efficiency improvements and integration of other low carbon energy sources besides carbon sequestration (Levina et al., 2013).

Along with renewable energy sources, hydrogen is considered to be an alternative low carbon solution capable of slowly replacing fossil fuels as an energy source. Hydrogen is an environmentally friendly energy carrier, implying that it is capable of delivering and storing tremendous amounts of energy without venting carbonaceous gases upon combustion. Energy that can be converted into electricity, power and heat, which represent essential elements to every societies' development (Satyapal, 2017).
As most of the current hydrogen production involves natural gas through steam methane reforming, denoted blue hydrogen, the process vents large amounts of CO_2 to the atmosphere. Combining blue hydrogen production with CCS has the possibility to transform the hydrogen production into a renewable source of energy. Thus, boosting their competitiveness and commercial positioning, paving a way for further development. Berge et al. (2016) also state that the amount of time it would require for renewable energy sources to match the amount of energy currently provided by the fossil fuel sector equals a century. Considering the fact that the energy demand increases annually, an energy transition to renewables without CCS would make a replacement from fossil fuels to renewable energy even harder to achieve (Berge et al., 2016).

Despite all the benefits of underground CO_2 storage, a potential gas leakage from the subsurface reservoirs imposes the largest threat to the implementation of CCS. This would discourage its purpose as the carbon could migrate through the subsurface and end up in the atmosphere, elevating the atmospheric carbon content (Berge et al., 2016). A gas leakage could act as a barrier towards further industrial implementation, as it imposes a risk related to the business' reputation.

On the other hand, the risk of leakage in hydrocarbon reservoir can be considered quite small as these reservoirs have stored gas for millions of years using various trapping mechanisms (Berge et al., 2016). This involves structural and stratigraphic trapping, residual and capillary trapping, solubility trapping and mineral trapping. Structural and stratigraphic trapping refer to the trapping of gas beneath either a stratigraphical or structural seal so that mobile accumulations of hydrocarbons can occur. Residual and capillary trapping refer to the CO_2 that remains in a reservoir after significant amounts of gas have been injected into a reservoir, as the buoyancy pressure of the CO_2 plume does not overcome the capillary entry pressure of the surrounding pore throats, thereby hindering migration of CO_2 to neighbouring pores. Solubility and mineral trapping refer to CO_2 that has been dissolved in water or that has chemically reacted with newly formed rock minerals (Hermanrud et al., 2009). The solubility of CO_2 in water increases with pressure and decreases with temperature and salinity (Solomon, 2007). The relative importance of each trapping mechanism varies with time, as illustrated in Figure 2.2.

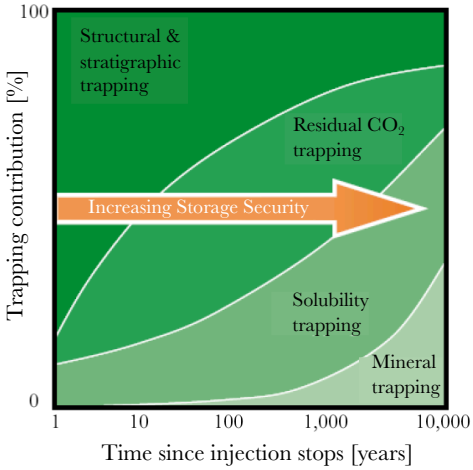

Figure 2.2: Various trapping mechanisms for CO_2. The contribution of each mechanism is plotted as a function of time since injection stops. The storage security increases with time as indicated by the orange arrow. Modified from Hermanrud et al. (2009).

Nonetheless, a prerequisite for permanent storage involves an area of structural simplicity. This includes an extensive cover of a low porous or permeable and ductile caprock overlaying a permeable and porous reservoir rock, blocking upwards migration of gas (Anderson et al, 2005). Valuable knowledge about safely storing carbon dioxide has also been acquired through EOR related gas injections (Berge et al., 2016). Since the geological formations of areas containing hydrocarbons have been extensively surveyed and mapped a leakage is

considered highly unlikely. Thus, with a properly selected, designed, monitored and operated storage site, the permanent storage of carbon dioxide is considered to be safe and permanent (Berge et al., 2016; Chadwick et al., 2008).

Equinor's project of injecting CO_2 into a saline aquifer at Sleipner is an ideal example of safe storage. Throughout the injection period the dissemination and behaviour of CO_2 in the reservoir have been carefully operated and monitored using time-lapse seismic (Berge et al., 2016). In combination with SINTEF's coordinated Pre-ACT project, these carbon storage projects provide scientists and operators with storage data essential to future CCS projects. The data can be used to estimate pore pressures in the reservoir, thus enabling operational decisions that maximize safety and storage capacity in a cost-efficient manner. The Pre-ACT project also utilizes an onshore field lab that demonstrates and monitors the carbon dioxide's behaviour in a sandy reservoir. Additionally, external participants can realistically test new methods and equipment at the facility, strengthening technological advancement and the CCS value chain's development (Benjaminsen, C., 2019). The CLIMIT-program, established by the Norwegian Ministry of Petroleum and Energy, could also improve the development as it solely aims to accelerate the commercialization of CCS through economic stimulation of research, development and demonstration (Halland et al., 2011).

From a different point of view, it is important to account for the risks of unforeseen leakages regarding well failure, the migration of gas through an abandoned well or a gradual leakage through undetected faults and fractures. As earthquakes could create unexpected faults and fractures, tectonically active areas are considered unstable with respect to permanent storage and are therefore avoided. The EU has however developed robust guidelines for effective and safe storage of CO_2 in saline aquifers, and provided several techniques that mitigate unforeseen hazards (Berge et al, 2016).

From another perspective, a strong commitment to carbon sequestration has the possibility to create new labour and grow low carbon value chains (e.g. blue hydrogen) (Størset et al., 2018). According to Størset et al. (2018), a commitment to CCS linked with large-scale hydrogen production, is considered necessary to secure economic growth and Norwegian jobs in the currently ongoing energy transition from fossil fuels to renewable energy. Especially when considering that a large portion of Norway's labour force and revenue is connected to the fossil fuel industry, and that CCS linked with hydrogen production has the opportunity to

strengthen and prolong the Norwegian natural gas market, thus sustaining the labour's competitiveness. Norway has many well mapped and natural storage sites in the North Sea together with a strong maritime and offshore based industry. This provides additional competitive advantages with regards to an industrial implementation of CCS (Størset et al., 2018; Berge et al, 2016).

Here, the development of industrial CCS is based on predictions. Therefore, the extent to which can actually become achievable and realistic remains hard to quantify. Primarily, the development of CCS depends on governmental cooperation and policymaking. A favourable policy framework would promote CCS as an alternative in climate change mitigation through regulations, providing commercial and sustainable business growth opportunities for CCS (Brown et al., 2020). Furthermore, it is possible to assume that with increased attention and public pressure towards reaching the climate goals by 2050, decarbonised energy and products are valued higher by their consumers, while the taxes of emitting carbon to the atmosphere will simultaneously increase (Pales et al., 2019; Stub et al., 2019). This will provide the producers with incentives to reduce their share of emissions or to invest in abatement measures, strengthening CCS' position in the global market (Brown et al., 2020).

Holmås et al. (2019) state that the EU's quota of emitting carbon dioxide to the atmosphere has been and is likely to remain lower than what IPCC suggest is necessary to meet the climate goals by 2050. This causes a risk in regards to the long term beneficial gain of the CCS value chain, as the price of emitting carbon to the atmosphere will remain lower than the cost of capturing and storing the gas. A factor implying that governmental support and measures aiming to promote markets for decarbonised products are required for CCS to act as an attractive opportunity in emission abatement (Holmås et al., 2019).
It is important that policies and regulations driving the decarbonisation of the industrial sector simultaneously establish effective measures that prevent other industries from losing market shares due to costly climate policies, a phenomenon known as "carbon leakage" (Brown et al., 2020). Measures involving business models and demands that carefully develop a market for carbon neutral solutions in a transition phase to decarbonised industrial production (Stub et al., 2019). The fact that CCS facilities are expensive to build and that the European quota for emitting carbonaceous gases increases more slowly than required, the initiation of the first CCS facilities requires governmental funding and support (Stub et al., 2019).

The Northern Lights project is the first full-scale CCS project and involves the sequestration of carbon dioxide from cement production, primarily funded by the Norwegian Government in cooperation with Equinor, Shell and Total (Northern Lights Project, 2020).
Based on the fact that the European climate policies are at a formative stage, the Norwegian Government's ambition is that the project can act as a flagship towards the international implementation of CCS, influencing policy making through an effective demonstration of the viability of the CCS value chain. An effective demonstration will most likely improve the acceptability and support for CCS as a safe, feasible and attractive abatement option, while simultaneously providing knowledge in terms of regulatory and commercial frameworks in support of CCS. A favourable policy making impacts the scale of future CCS projects, thus securing technological advancement and cost reductions (Brown et al., 2020).

2.3 Summary

With possibilities and risks in mind, CCS has the opportunity to play a key role in the transition from fossil fuels to renewable energy. IEA states that in order to meet climate goals, a cumulative of 107 Gt of CO_2 needs to be stored in the period to 2060 (Pales et al., 2019). In comparison, Norwegian Petroleum Directorate's Atlas estimates that the storage capacity in the North Sea is equal to 70 Gt (Halland et al., 2011). These facts prove the potential for Norwegian industry in terms of CCS, offering storage capacity to a compelling energy intensive market emitting large quantities of CO_2. Combining hydrogen production and CCS offer low carbon energy while simultaneously diminishing a large share of the fossil fuel sector's emissions, creating an interconnected system between the fossil fuelled industry and power sector, and the renewable and decarbonised energy sector (Figure 2.3).

This highlights the importance of time-lapse seismic monitoring as it provides essential and beneficial information about dynamic reservoir conditions, detecting potential leakages and optimizing storage capacity and efficiency. Seismic monitoring can therefore contribute to secure a safe and sustainable future for CO_2 storage, by strengthening the viability of the CCS value chain, thus the decarbonised energy sector in a futuristic energy driven society.

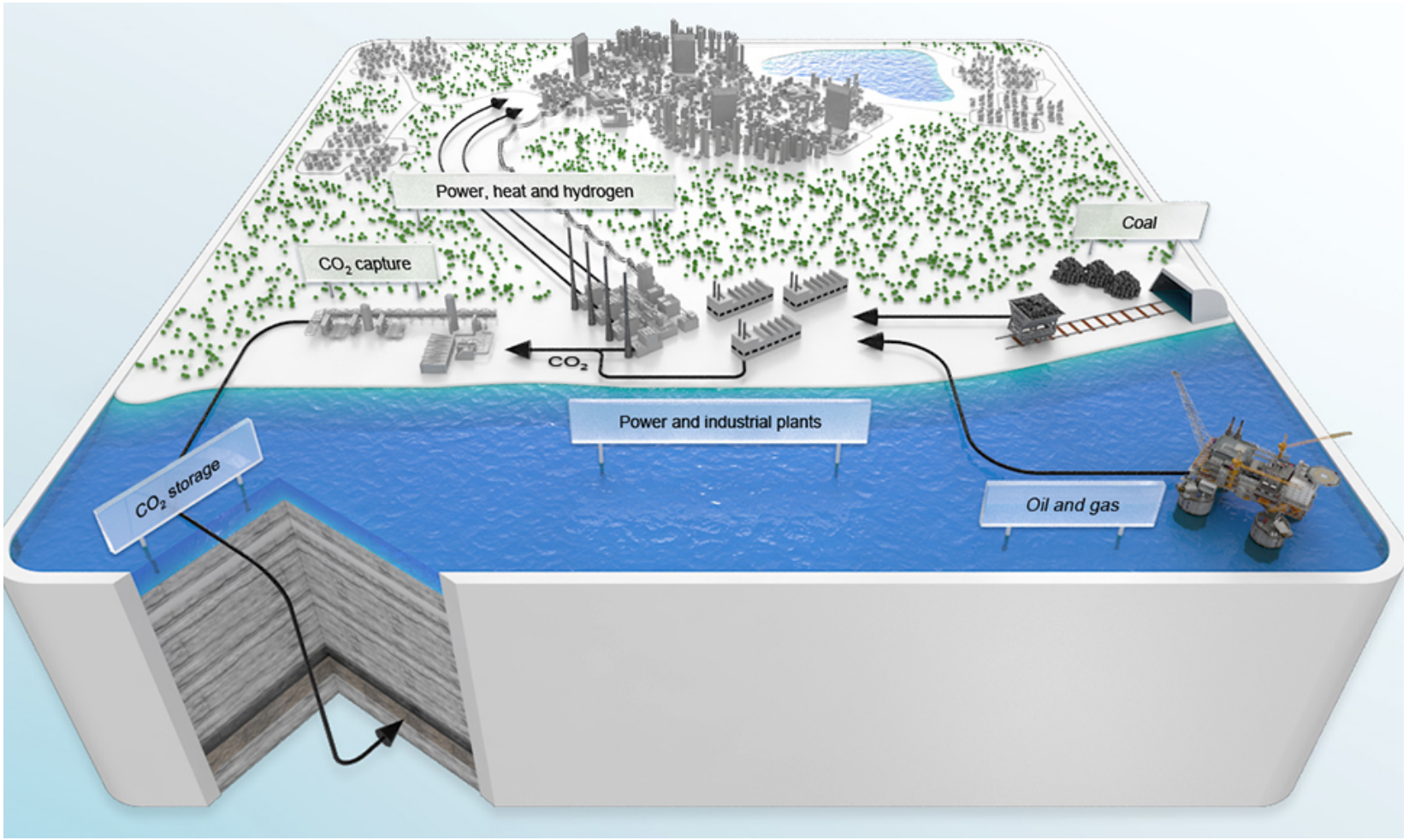

Figure 2.3: Illustration of CCS' role in an interconnected system, decarbonising the fossil fuel sector while simultaneously providing clean hydrogen energy. Source: Gassnova (2020).

3 Rock physics modelling of CO_2 fluid substitution

3.1 Outline

The purpose of this chapter is to provide background theory about elastic waves, rock physics and rock physics modelling. This will strengthen the understanding of how carbon dioxide injections influence reservoir properties and thus seismic responses under given temperature and pressure conditions. Knowledge about elastic wave theory and rock physics modelling is fundamental for being able to connect the use of seismic data to rock physics and reservoir characterization and monitoring. The information presented in this chapter is primarily based on Gelius and Johansen (2010) and Avseth (2010).

3.2 Elastic waves & rock physics

3.2.1 Elastic waves

Elastic waves represent pulses of energy propagating through the Earth. Reflections of these from discontinuities make it possible to create seismic images. These images contain valuable information about physical conditions in -and around storage sites for carbon sequestration. The elastic waves are generated by hydrophones in marine seismic, emitting energy pulses within a given frequency band. These waves deform the Earth elastically, which means that the energy pulses temporarily deform the subsurface rocks, such that the rock returns to its original shape and form after passage of the wave. Elastic wave propagation assumes a linear relationship between the stress imposed on a rock and the resulting deformation of the rock. This relationship is referred to as Hooke's law (Figure 3.2.1).

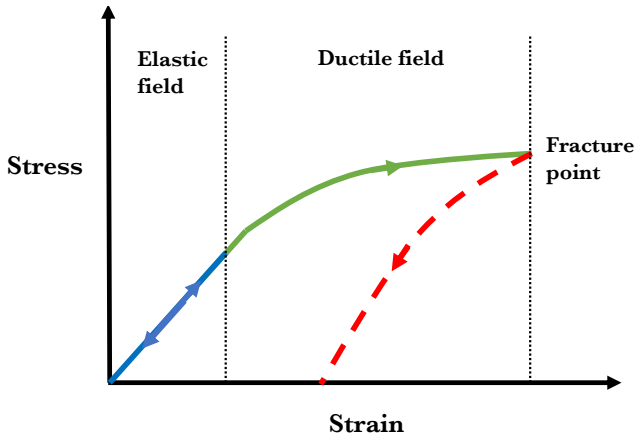

Figure 3.2.1: The relationship between stress and strain of a rock. If the stress does not exceed the elastic field, the rock returns to its original shape and form (blue). By applying more stress, the rock becomes permanently deformed (green). Ultimately, the rock fractures if the stress is further increased (red). Modified from Gelius and Johansen (2010).

Elastic waves compose of primary -and secondary waves, denoted P -and S-waves, each embossed with distinctive wave characteristics. Primary waves propagate through subsurface strata parallel to the particle motion, alternating compression and expansion of the medium. The P-wave travels through all types of materials including solids, liquids and gases, and usually propagates with velocities of 1-14 km/s. On the contrary, the S-wave propagates through medium perpendicular to the particle motion, vibrating the ground in a shearing motion. Shear waves only propagate through solid material, with velocities between 1-8 km/s. The exact velocities of the elastic waves through a rock formation depend on the rock type, hence the physical properties of the rock. The physical properties of a rock are described in the following subchapter.
Considering a homogenous and isotropic medium, the P -and S-wave velocities can be expressed as:

$$V_p = \sqrt{\frac{K + \frac{4}{3}\mu}{\rho}} \tag{3.1}$$

$$V_s = \sqrt{\frac{\mu}{\rho}} \tag{3.2}$$

Where V_p and V_s are the P -and S-wave velocities, K is the bulk modulus (MPa), μ is the shear modulus (MPa), and ρ is the density (kg/m^3) of the rock.

Equations (3.1) and (3.2) are derived by combining the elastodynamic wave equation with Hooke's law (Appendix A). The underlying assumptions when deriving these equations are based on a curl-free primary wave and a divergence-free secondary wave.

Due to the fact that the subsurface strata consist of layers with various physical properties, a proportion of the energy in the elastic waves will be reflected at boundaries between the layers. The amount of energy that is reflected depends on the contrast between the physical properties of the medium above and below the boundary. The remaining energy will be transmitted into the underlying formation (Figure 3.2.2). This process continues through the subsurface strata until all energy in the elastic waves has been transmitted or reflected. At

each boundary the incident ray generate both reflected and transmitted P -and S-waves (Kearey et al., 2002).

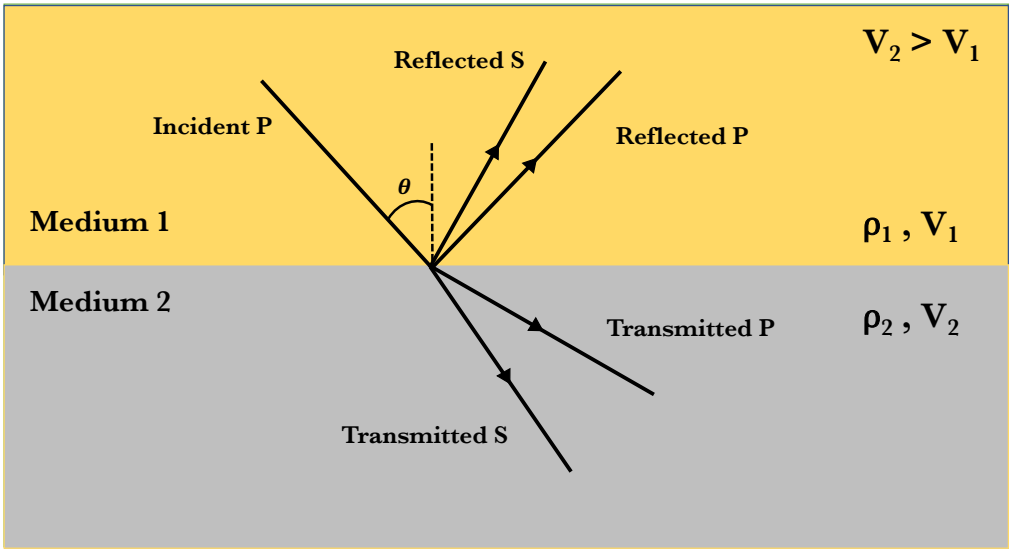

Figure 3.2.2: Illustration of an incident wave being reflected and transmitted at a boundary between two layers with different physical properties. Modified from Kearey et al. (2002).

How strong the reflections appear on a seismic profile depend on the reflection coefficient, which itself is a function of the acoustic impedance. In case of normal incidence the reflection and transmission coefficients and acoustic impedance are given below in equations (3.3) and (3.4). Since an incident ray is able to create both reflected P -and S-waves, four reflection coefficients can be defined: R_{pp}, R_{ps}, R_{sp} and R_{ss}. In case the incident ray hits the boundary at an angle, the reflection coefficient also depends on the angle of incident and is given by the Zoeppritz equations. A negative value for the reflection coefficient implies a phase shift of 180° of the reflected wave. This means a positive amplitude becomes negative during reflection.

$$R = \frac{I_2 - I_1}{I_2 + I_1}, \quad -1 \leq R \leq 1 \tag{3.3}$$

$$T = 1 - R = \frac{2I_1}{I_2 + I_1} \tag{3.4}$$

where R and T represent the transmission and reflection coefficients. I_1 and I_2 denote the acoustic impedances of layer 1 and 2 respectively, and given by:

$$I = \rho \cdot V \tag{3.5}$$

A bright reflection occurs if the contrast in acoustic impedance of two layers is significant as more energy is reflected rather than transmitted. In case the layer beneath the reflecting interface is stiffer the resulting reflection creates a peak, and vice versa if the layer is softer. Injecting CO_2 into a water saturated storage reservoir would strongly influence and lower the overall physical properties of the rock layer. This creates bright reflections on a seismic profile if the properties of the surrounding medium were stiffer originally.

On another note, it is important to be aware that to what extent the subsurface strata can be distinguished in details depends on the horizontal and vertical resolution of the seismic. The horizontal resolution is given by the Fresnel zone, which defines the portion of a reflector from which reflected energy can reach the detector within one-half the wavelength of the first reflected energy. The vertical resolution is considered to be equal to a quarter of the dominant wavelength of the elastic waves. The fact that the Earth also act as a natural frequency filter, attenuating the higher frequency waves with depth, the resolution reduces accordingly. As a consequence, minor faults and fractures might be concealed. This might compromise the sealing mechanism of the caprock above a potential storage site. Luckily, due the strong influence of injected carbon dioxide on physical rock properties, a leakage can be tracked with time-lapse seismic.

3.2.2 Rock physics

It is essential to understand how injected carbon dioxide influences reservoir conditions and seismic data. This implies use of rock physics which builds upon a description of subsurface media in terms of physical rock properties. Rock physics connects the gap between quantitative geophysical measurements and qualitative geological parameters. In other words, the relationship between observed seismic data and concealed reservoir properties. To understand the value of rock physics regarding seismic monitoring of CO_2 injections, it is important to define the underlying rock physical properties characterizing a subsurface layer, ensuring that temporal variation in fluid composition and pressure within injected reservoirs can be tracked.

Each layer of the subsurface strata consists of mechanical properties based on relations between the applied stress on a material and the resulting deformation (Figure 3.2.1). Furthermore, a porous rock consists of various constituents, i.e. grains, fluids and minerals. Varying compositions causes varying effective elastic properties of the subsurface layers. Hence, the effective elastic properties can be modelled from knowing the elastic properties of each constituent and the corresponding fraction. Additionally, the effective elastic parameters depend on the geometrical orientation and mechanical interaction of the constituents. In the case of isotropic media the mechanical properties of a rock can be described using the elasticity parameters: incompressibility and rigidity.

Incompressibility, also known as the bulk modulus, expresses a materials resistance to volume change (Figure 3.2.3). In contrast, the rigidity or shear modulus, expresses a materials resistance to shearing (Figure 3.2.3).

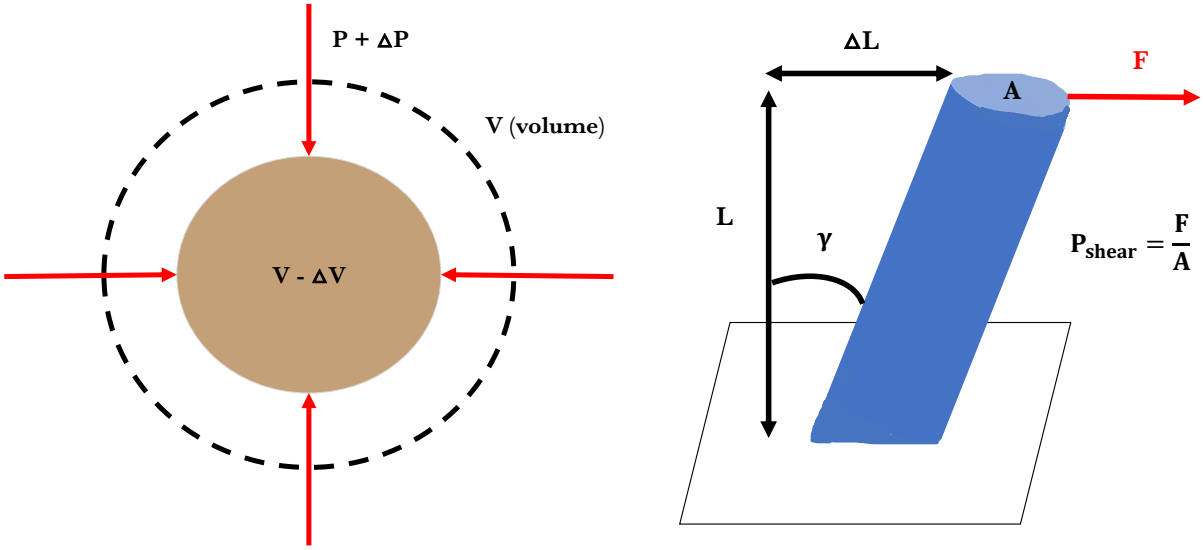

Figure 3.2.3: The incompressibility (left) and rigidity (right) of a material. Modified from Gelius and Johansen (2010).

The bulk and shear modulus can be described mathematically as:

$$K = \frac{\Delta P}{\Delta V / V} \tag{3.6}$$

$$\mu = \frac{P_{shear}}{\tan(\gamma)} \tag{3.7}$$

where K is the bulk modulus (MPa), μ is the shear modulus (MPa), P is the applied stress (N/m^2) and V is the volume (m^3).

Density is also an important physical property and is defined by a rock's mass divided by the resulting change in volume (Figure 3.2.4).

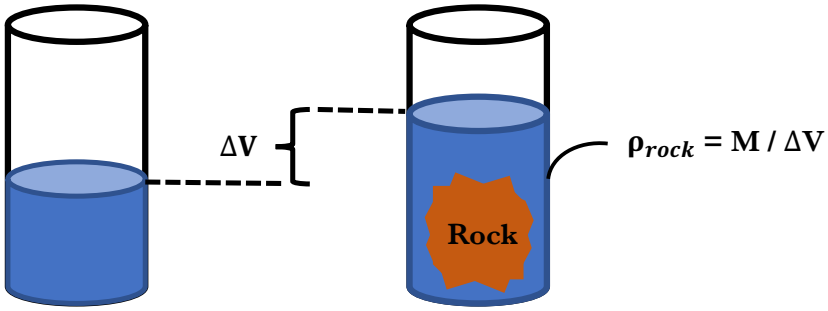

Figure 3.2.4: Illustrating the principle of deriving a rock's density which is its weight divided by volume.

By utilizing rock physics tools based on these elasticity parameters, e.g. AVO and bright spot analysis, it is possible to acquire information about the subsurface rocks and pore fluid saturations from reflection amplitudes. Based on the fact that seismic amplitudes primarily represent contrasts in elastic properties and/or densities between distinct layers, the amplitudes can reveal information about porosity, lithology, pore fluid type and saturation, and pore pressure in a subsurface formation. Information about these reservoir properties are important in prospect evaluation and reservoir characterization and monitoring. This composes the main reason rock physics has become an integrated part of quantitative seismic interpretation, enabling the link between seismic data and geological processes. Thus, minimizing the injection risk and ensuring safer and more efficient CO_2 storage.

In order to understand how reflection amplitudes reveals information about subsurface conditions, the next subchapters will present various physical properties of various rock aggregates including how they are mixed to form a basis for rock physics modelling.

3.3 Physical properties of water, gas and oil

Knowledge about the specific physical properties of pore fluids is fundamental to make sense of the contrasts between reflections in seismic images. In the previous subchapter it was shown that reflections depend on contrasts in acoustic impedances, defined by densities and velocities of the rock layers (3.3). The velocities of elastic waves propagating through a rock can be expressed by their effective density, bulk and shear modulus (3.1 - 3.2). The physical properties of the fluids occupying the pore space in a rock affect the effective rock properties, and thus the acoustic impedance and reflection amplitudes. However, the shear modulus is unaffected as fluids have no shear strength.

The most common pore fluids are water, oil and gas. Their physical properties vary with chemical composition, temperature and pressure (Batzle and Wang, 1992). Typical physical properties of various fluids at surface conditions are presented below in Table 3.3.1.

Table 3.3.1: Density, bulk modulus and P-wave velocity of water, oil and gas.

Fluid Type	**Density - ρ (kg/m^3)**	**Bulk Modulus - K (MPa)**	**Velocity – V_p (km/s)**
Water	$1.0 \cdot 10^3$	$2.24 \cdot 10^3$	1.49
Oil	$0.9 \cdot 10^3$	$1.90 \cdot 10^3$	1.45
Gas	1.44	0.13	0.3

Salinity is the dominant parameter when defining the seismic properties of water, and saline water is usually referred to as brine. The properties also depend on temperature and pressure as illustrated in Figure 3.3.1. The temperature and pressure dependency of the seismic properties of brine are less compared to oil and gas (Figures 3.3.2 and 3.3.3).

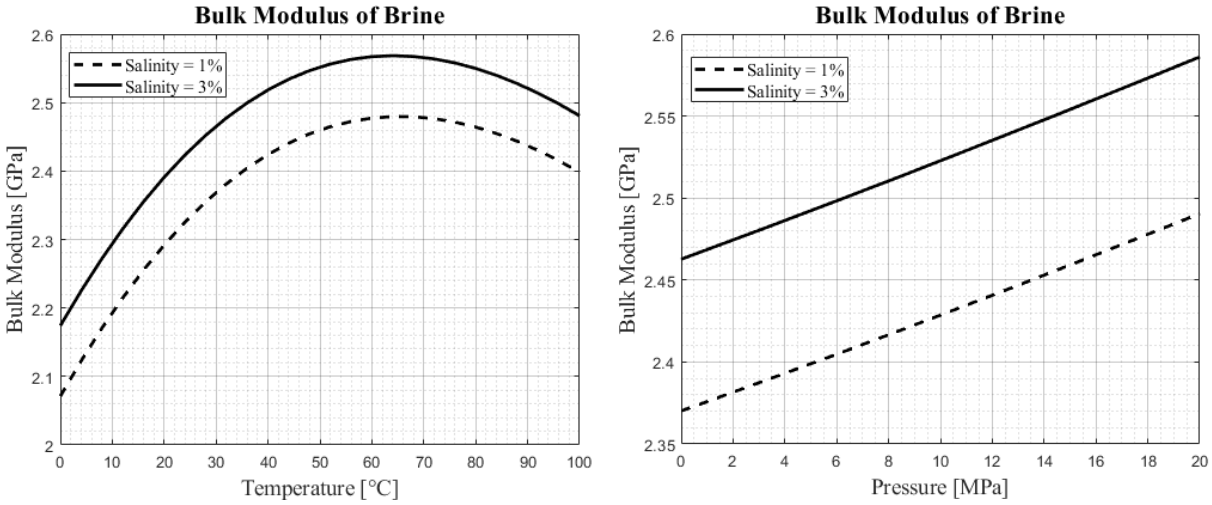

Figure 3.3.1: Bulk modulus of brine as a function of temperature (left) and pressure (right). The bulk modulus increases with increasing pressure and salinity, and decreases with increasing temperature.

The parameter used to define the seismic properties of oil is the reference density, denoted $\rho_{o_{ref}}$. The reference density is the density of oil measured at a pressure of 1 bar and a temperature of 15.6°C. The seismic properties of oil may be expressed by the API number as:

$$API = \frac{141.5}{\rho_{o_{ref}}} - 131.5 \tag{3.8}$$

As a rule of thumb; A high reference density which implies a low API number enhances the physical properties of the fluid and vice versa (Figure 3.3.2). It is equally important to see that an increase in pressure increases the physical properties, while the opposite applies to temperature.

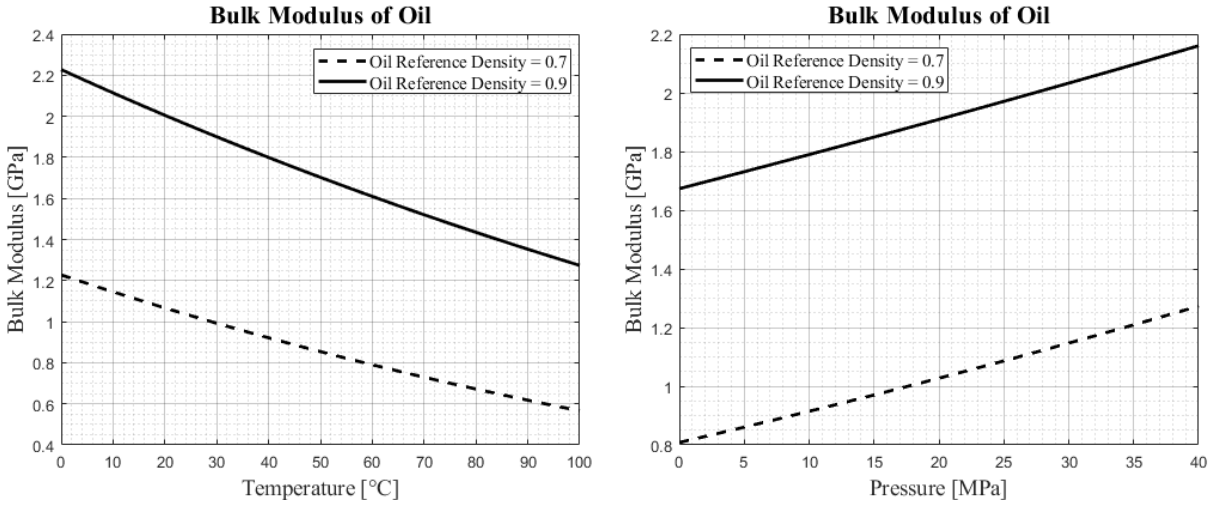

Figure 3.3.2: Bulk modulus of oil as a function of temperature (left) and pressure (right). The bulk modulus increases with increasing pressure and reference density, and decreases with increasing temperature.

The gas gravity is the parameter used to define the seismic properties of gas. It is defined as the ratio between the density of gas and the density of air at an atmospheric pressure of 1 bar and a temperature of 15.6°C. Higher gas gravity values imply heavier gases with elevated physical properties (Figure 3.3.3).

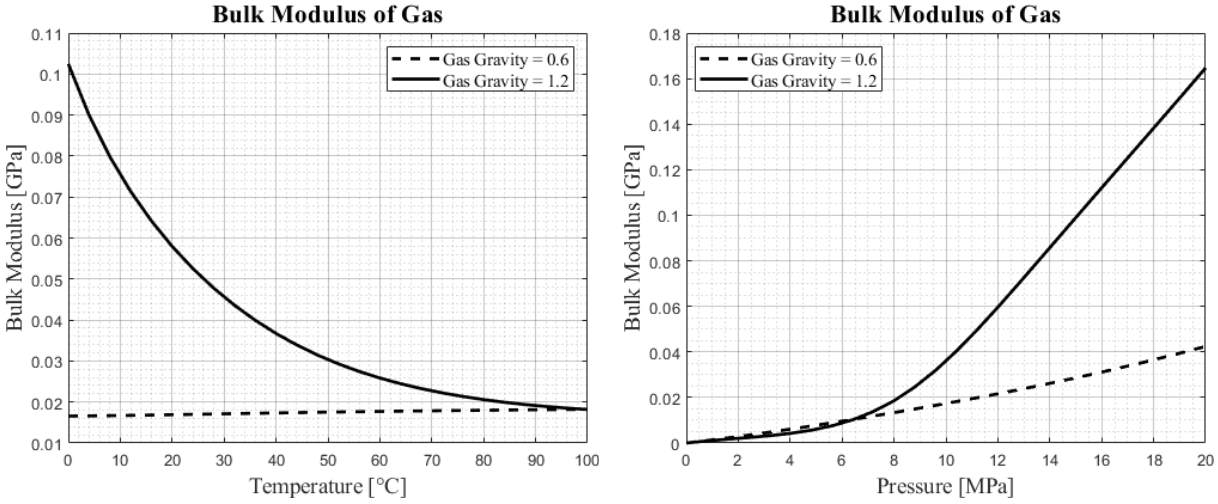

Figure 3.3.3: Bulk modulus of gas as a function of temperature (left) and pressure (right). The bulk modulus increases with increasing pressure and gas gravity, and decreases with increasing temperature.

3.4 Physical properties of CO_2

Considering that the physical properties of gas vary with composition, the specific physical properties of CO_2 have to be taken into account in order to comprehensively understand how carbon dioxide injections affect the seismic responses. Moreover, the various storage sites might be located at different depths with various geothermal gradients. In light of this, it becomes interesting to study the physical behavior of CO_2 under different temperature and pressure regimes and compare it with the physical properties of brine under the same conditions to highlight the effect of fluid substitution (Figures 3.4.1 and 3.4.2). The values are based on empirical relations in Batzle and Wang (1992) for reservoir fluids and Span and Wagner (1996) for CO_2.

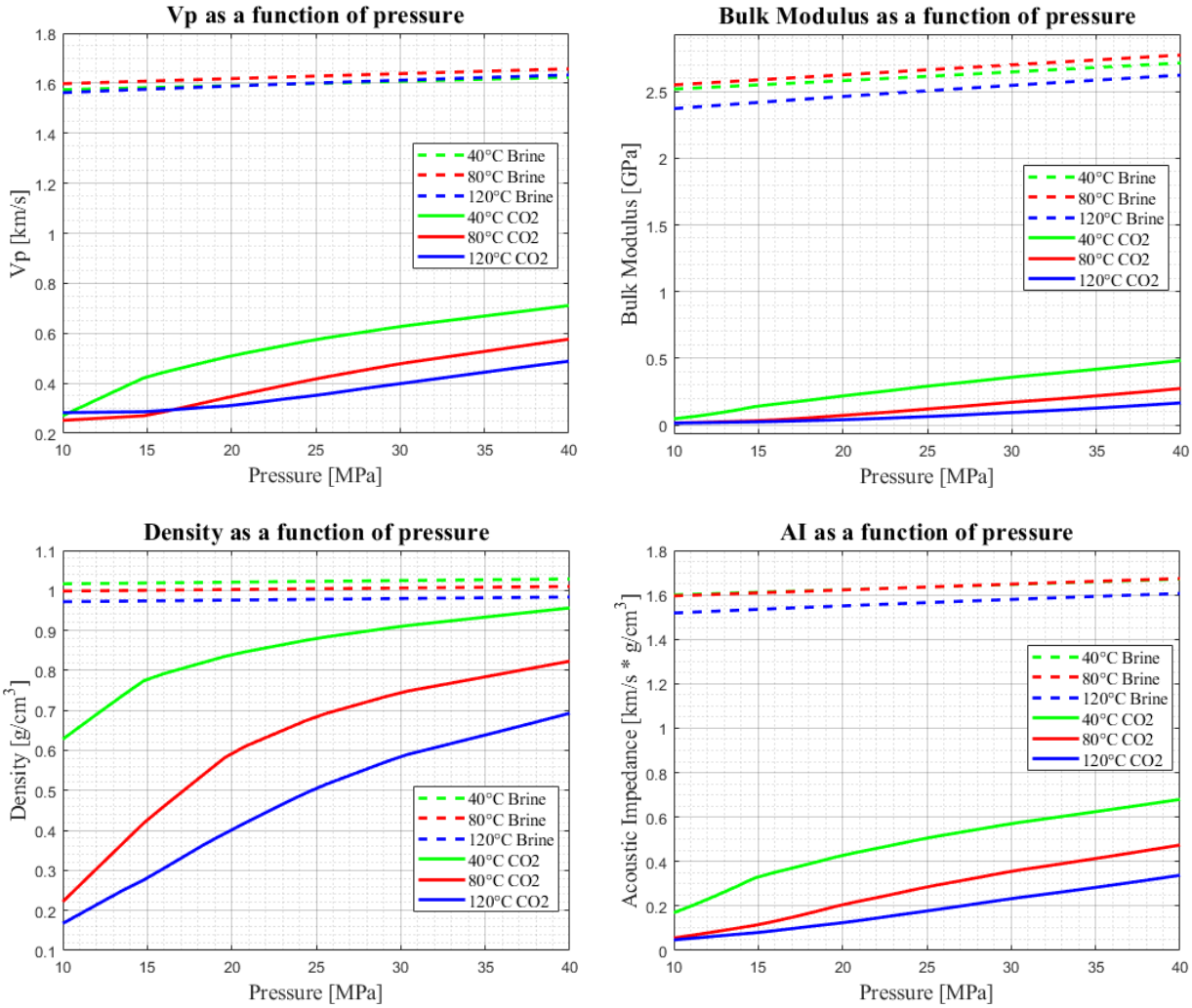

Figure 3.4.1: Plots illustrating the effect of substituting brine with carbon dioxide on the P-wave velocity (top left), bulk modulus (top right), density (down left) and acoustic impedance (down right). The physical properties are plotted for different temperatures as a function of pressure. The dotted lines represent brine, while the solid lines represent carbon dioxide.

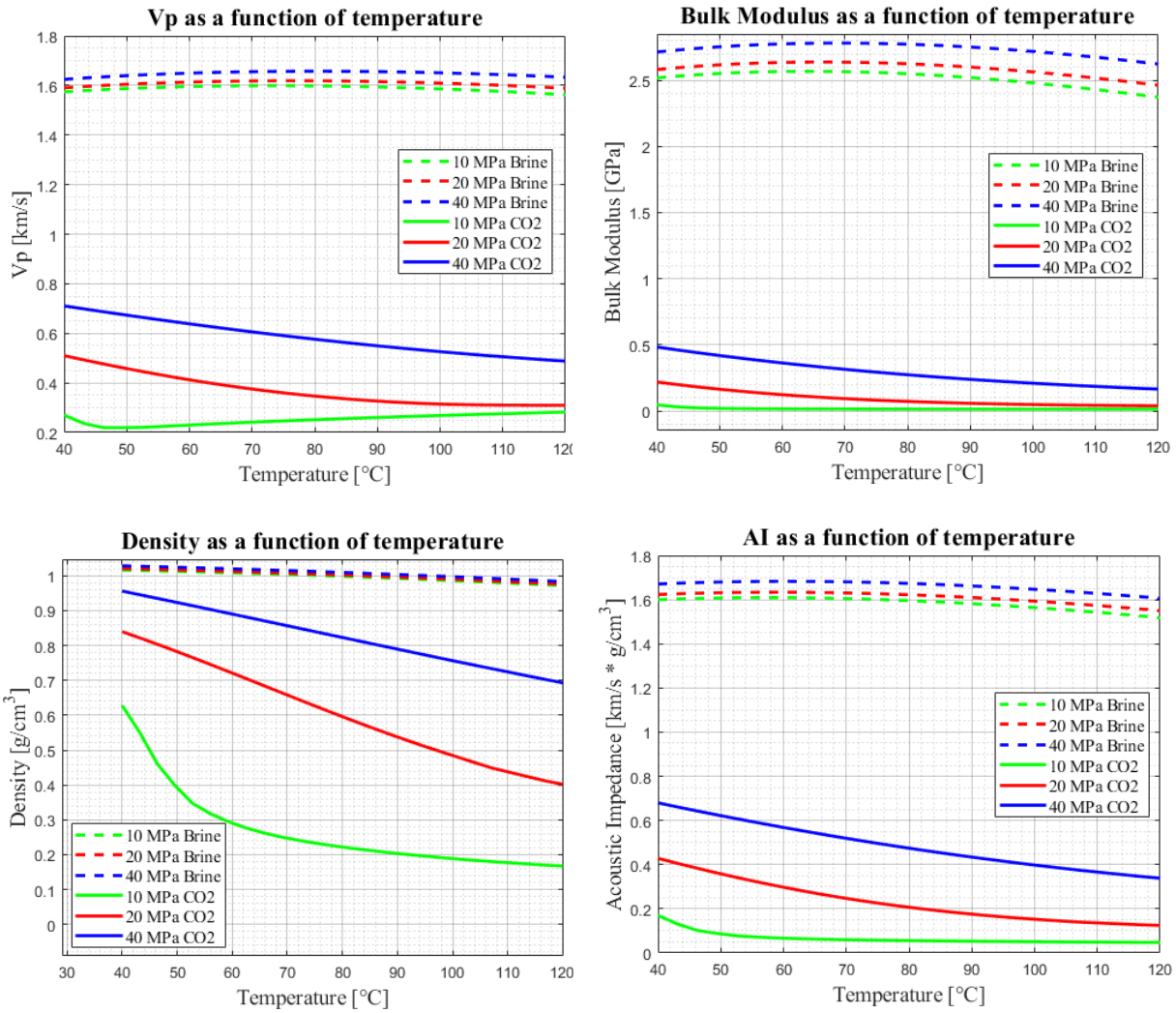

Figure 3.4.2: Plots illustrating the effect of substituting brine with carbon dioxide on the P-wave velocity (top left), bulk modulus (top right), density (down left) and acoustic impedance (down right). The physical properties are plotted for different pressures as a function of temperature. The dotted lines represent brine, while the solid lines represent carbon dioxide.

Figure 3.4.1 and Figure 3.4.2 show large contrasts between the physical properties of brine and carbon dioxide. The difference increases with increasing temperature and decreases with increasing pressure. Consequently, the contrast in acoustic impedance is significant and indicates that a substitution from brine to carbon dioxide will most likely alter strongly the reflection amplitude along a seismic profile, which might make it easier to monitor gas injections using time-lapse seismic.

In terms of storage, the phase state of carbon dioxide also affects the physical properties. A phase diagram representing the state of carbon dioxide can be created by correlating temperature with pressure (Figure 3.4.3). The phases include a solid, fluid and gas state.

However, carbon dioxide can also behave as a supercritical fluid, implying that the physical properties of carbon dioxide are between the fluid and gas phase. As a supercritical fluid the viscosity is similar to a gas while the density is similar to a fluid (Hellevang, 2015; Lumley, 2010).

Hence, it is beneficial to store carbon dioxide in a supercritical state as the gas occupies less volume and is more mobile due to its gas-like viscosity. Therefore, storing carbon dioxide in a supercritical state would increase the storage capacity while simultaneously contribute to diminishing a larger portion of the industrial emissions.

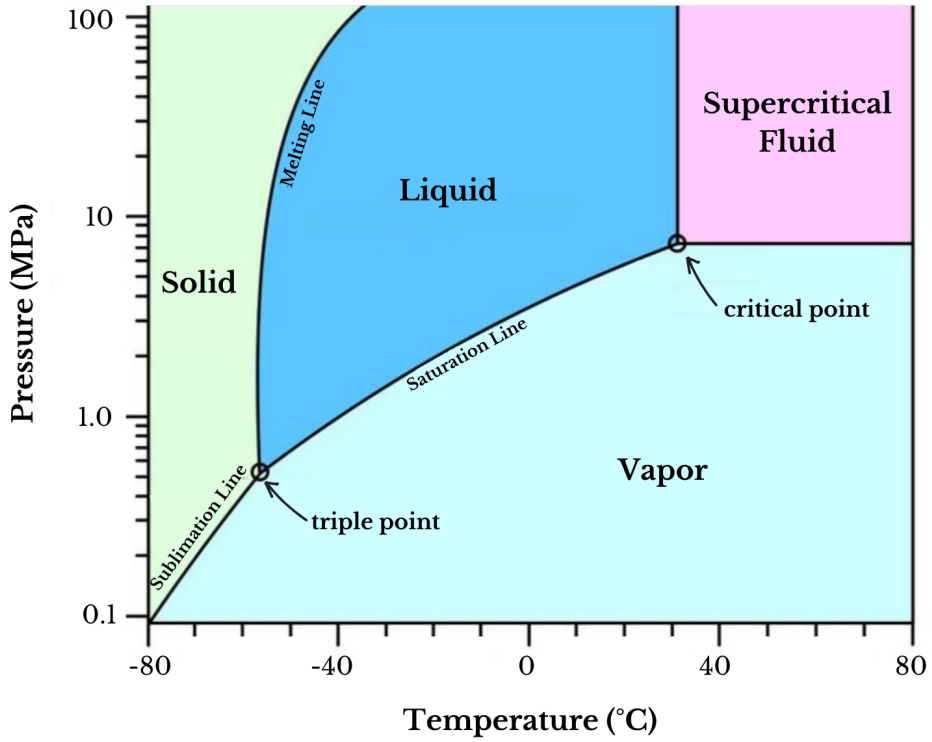

Figure 3.4.3: A phase diagram illustrating carbon dioxide's state dependency on pressure as a function of temperature. The pressure interval reaches from 0.1 – 100 MPa, while the temperature interval reaches from -80 – 80 °C. The critical point occurs at approximately 31°C and 7.39 MPa, while the triple point occurs at approximately -56.6°C and 0.158 MPa. Modified from Gierzynski (2016).

The physical properties of supercritical and liquid carbon dioxide are shown in Table 3.4.1, with values as given by Span and Wagner (1996). Notice the substantial decrease in velocity, density and bulk modulus in the transition from liquid to supercritical CO_2, implying that the seismic amplitudes and reflections will change when storing carbon dioxide in a supercritical state.

Table 3.4.1: The physical properties of CO_2 as a liquid and supercritical fluid.

Temp (°C) [K]	Pressure (MPa)	Density (kg/m^3)	Bulk Modulus (MPa)	Velocity (km/s)
27 [300]	10	801.6	137.58	0.414
77 [350]	10	228.8	14.14	0.249

3.5 Physical properties of grains, sandstones and shales

The previous subchapters have focused on elastic media. This subchapter makes a transition from elastic media to poroelastic media.

Sandstones and shales are the most common reservoir, source and caprocks found in subsurface prospects. These sedimentary rocks consist of siliciclastic sediments and grains, composed primarily of quartz, feldspar and clay minerals including kaolinite, smectite and illite (Bjørlykke, 2015).

The specific physical properties of sandstones and shales depend on the primary composition of the sediments, and also by the textural and mineralogical composition. The depositional environment and the diagenetic processes also affect the composition and textural effects. This indicates that the properties of sedimentary rocks change from the time of deposition to burial at great depths and during any subsequent uplift. Hence, a combination of mechanical compaction and chemical processes causing dissolution and precipitation of minerals takes place. Physical and chemical processes that are predominantly influenced by changes in temperature and pressure. (Bjørlykke, 2015)

The grains in siliciclastic rocks are characterized mainly based on their size and are distinguished by using the classification scheme shown in Figure 3.5.1.

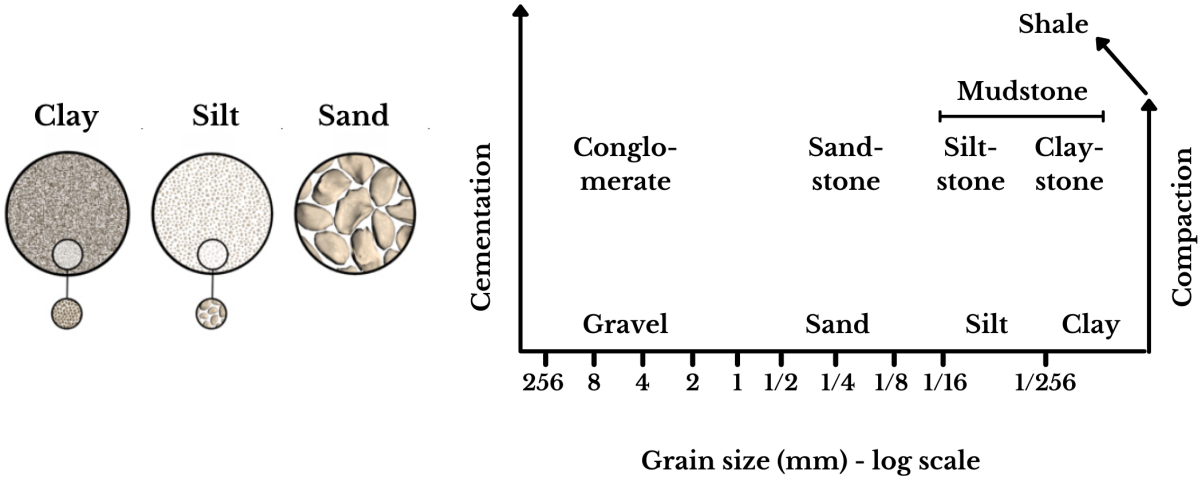

Figure 3.5.1: Sediment classification scheme based on grain size, with the relative grain sizes for sand, silt and clay illustrated to the left. Cementation and compaction are represented on the y-axis as a function of grain sizes, implying that an increase will lead to cementation and compaction of sediments to the respective sedimentary rocks above. Modified from Gelius and Johansen (2010) and The Comet Program (2010)

The typical physical properties of the most common grains in sedimentary rocks are listed below in Table 3.5.1 (Mavko et al., 2009). It is worth noticing the large difference in physical properties between clay minerals, thus influencing the effective physical properties of rocks. Poisson ratio represents the ratio between contraction and extension of the material when imposed to stress.

Table 3.5.1: Physical properties of common rock minerals.

Mineral	**K (MPa)**	**μ (MPa)**	**Density (g/cc)**	**Vp (km/s)**	**Vs (km/s)**	**Poisson Ratio**
Clays						
Kaolinite	1.5	1.4	1.58	1.44	0.93	0.14
“Gulf Clays”	25.0	9.0	2.55	3.81	1.88	0.34
Silicates						
Feldspar	37.5	15.0	2.62	4.68	2.39	0.32
Quartz	37.0	44.0	2.65	6.05	4.09	0.08

Sandstones and shales may vary greatly with respect to grain texture, mineral composition and respective mineral fractions. Porosity and pore geometry also vary within these rocks, and represent very important elements in terms of dry rock properties (Gelius and Johansen, 2010). Porosity is defined as the proportion of a rock which might contain a pore fluid, whereas the pore space geometry defines the shape of the pore spaces and their concentrations respectively. Thus, influencing the rock's permeability. Since clay and sand particles have different textures and mineral compositions, the porosity and pore space geometry of compacted sandstones and shales change when subjected to pressure and temperature alternations. This applies throughout their burial history, controlled by both mechanical and chemical compaction of grains with depth as illustrated by Figure 3.5.2.

Clay particles have a higher porosity at the time of deposition compared to sand particles, but decrease more rapidly with depth due to their textural difference. Chemical reactions deforming silicate minerals to clay minerals explain the sudden decrease in sandstone porosity and permeability as the shale particles clog pore throats, thereby reducing porosity and permeability (Figure 3.5.2). Even quartz grains can be partially deformed, enlarging contact areas between grains and reducing the porosity (Avseth et al., 2005).

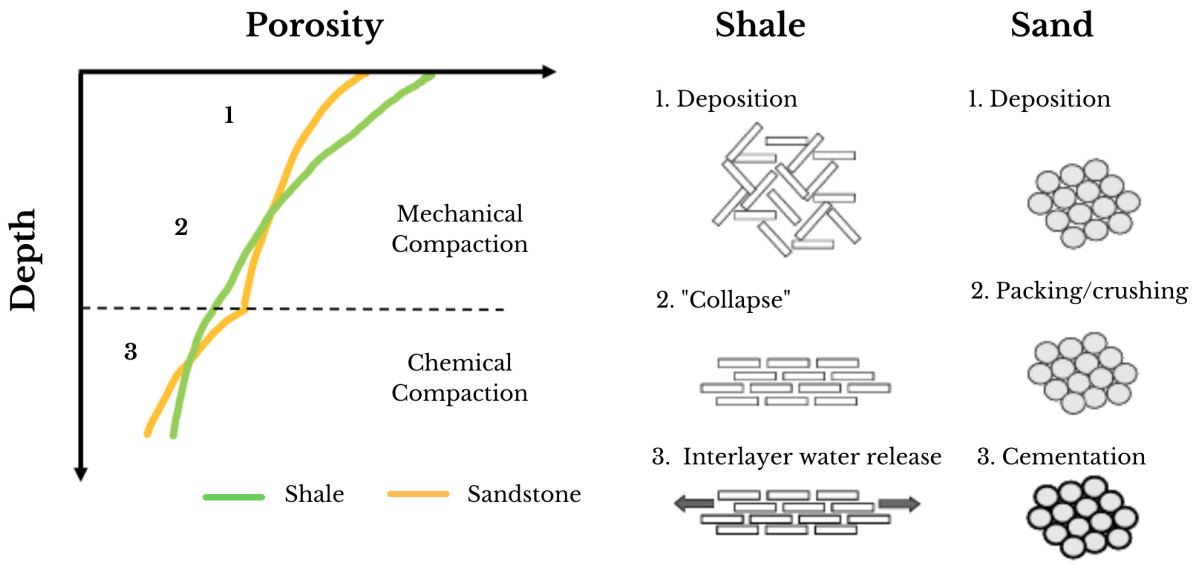

Figure 3.5.2: Illustration of the porosity-depth trend for sandstones and shales. Mechanical and chemical compaction are separated by the dotted line, with stages of compaction numbered from 1-3. The stages of compaction for shale and sand grains, from loose sediments to consolidated rocks, are illustrated to the right. Modified from Gelius and Johansen (2010) and Avseth et al. (2005).

The general trend in regards to physical properties involves a stiffening with depth as a result of porosity reduction due to mechanical and chemical compaction. Thereby, increasing the rocks' elastic properties. On the other hand, a subsequent uplift makes the rock prone to extensive fracturing due to a pressure decrease, weakening the framework of the rock and its elastic properties.

The physical properties of a rock depend on provenance, depositional environment and burial history. This shows the importance of understanding and incorporating sedimentary geology as a part of seismic interpretation and monitoring to avoid pitfalls involving fluid-lithology, sand-shale and porosity-saturation effects on time-lapse seismic (Avseth et al. 2005; Bjørlykke, 2015).

3.6 Mixing of grains

The effective elastic properties of a rock are also influenced by the way solid grains mixes within the rock aggregate. The mixing between solid grains is commonly characterized as a soft or stiff mix, referring to the geometrical distribution between stiff and soft material. The computation of the effective physical properties are denoted effective medium modelling, and provides either one or a set of effective medium parameters. The most popular modelling approaches for solid grains include VRH-bounds and Hashin-Shtrikman bounds.

3.6.1 Voigt – Reuss - Hill bounds

The Voigt (1928) and Reuss (1929) mixing models represent the absolute upper and lower bounds for interpolating the elastic properties of isotropic and anisotropic rocks. The Reuss mixing model corresponds to the softest composite mixture, while the Voigt mixing model corresponds to the stiffest composite mixture.

In order to describe these models mathematically, imagine a composite consisting of alternating layers of sandstone and shale. Let $V1$, $V2$ and $M1$, $M2$ denote the volume fractions and elastic moduli of the respective sedimentary rocks. The Reuss model considers the elastic moduli when the stress is applied normal to the horizontally aligned layers. Due to the fact that the properties of shale are softer than sand, the resulting strain is larger in shale layers even though the applied stress is constant. As a consequence, the effective elastic moduli get a lower limit:

$$\frac{1}{M_{Reuss}} = \frac{V_1}{M_1} + \frac{V_2}{M_2} \tag{3.9}$$

On the other hand, the Voigt mixing model considers the elastic moduli when the stress is applied parallel to the vertically aligned layers. This provides dominance to the stiffer sandstone layers. Hence, the effective elastic moduli get an upper limit:

$$M_{Voigt} = V_1 M_1 + V_2 M_2 \tag{3.10}$$

If the composite consists of more than two materials, the moduli can be estimated as an extended sum of the Voigt and Reuss equations (3.9 - 3.10). Furthermore, the Hill (1963) mixing model provides an arithmetic mean between the Reuss and Voigt models, and is usually applied if information about the geometrical distribution is not known. This can be expressed mathematically as:

$$M_{Hill} = \frac{M_{Voigt} + M_{Reuss}}{2} \tag{3.11}$$

Figure 3.6.1 illustrates the difference between the iso-strain and iso-stress mixing models with respect to the direction of the stress tensor σ.

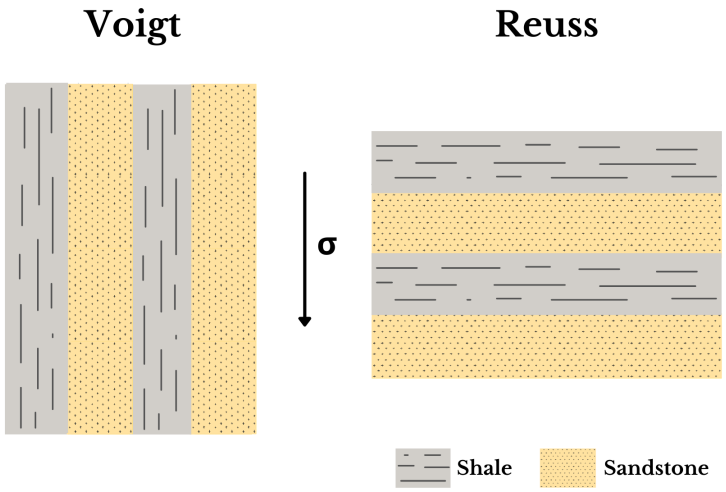

Figure 3.6.1: The iso-strain (left) and iso-stress (right) mixing models. The composites acquire maximum and minimum stiffnesses when the layers are aligned parallel or perpendicular to the applied stress tensor σ.

3.6.2 Hashin-Shtrikman bounds

The Hashin-Shtrikman bounds represent the most optimal bounds for an isotropic rock with the narrowest possible range of elastic moduli when the geometries of the constituents are unknown (Mavko et al., 2009). Hashin-Shtrikman bounds can be viewed as one constituent coating the other, forming an inner and outer spherical core of soft and stiff material (Figure 3.6.2). In case the stiffer material coats the softer material, the elastic moduli can be modelled using the Hashin-Shtrikman upper bound, denoted HS^+ and vice versa. A figure illustrating the differences between the Voigt and Reuss interpolations, and the Hashin-Shtrikman interpolations are shown below (Figure 3.6.3).

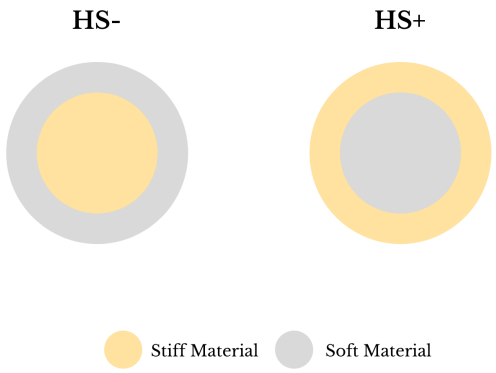

Figure 3.6.2: The differences between the lower and upper Hashin-Shtrikman bounds.

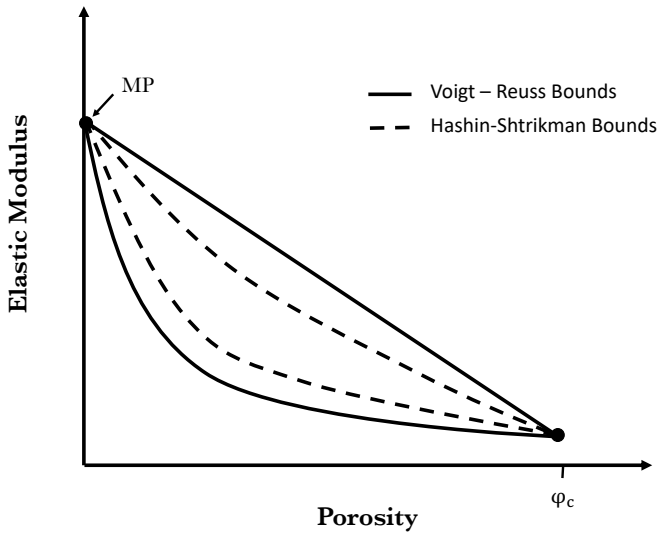

Figure 3.6.3: The relative differences between the Voigt-Reuss -and Hashin-Shtrikman bounds, interpolating elastic moduli from the critical porosity point to the mineral point.

Hashin-Shtrikman bounds can also be combined with Walpole's (1966a,b) theory to provide more generalized versions of the elastic moduli. The elastic moduli of Hashin-Shtrikman-Walpole (HSW) bounds can be expressed by equations (3.12) and (3.13).

$$K = K_1 + \frac{V_2}{(K_2 - K_1)^{-1} + V_1\left(K_1 + \frac{4}{3}\mu_{max}\right)^{-1}} \tag{3.12}$$

$$\mu = \mu_1 + \frac{V_2}{(\mu_2 - \mu_1)^{-1} + V_1(\mu_1 + \frac{\mu_{max}}{6}\left(\frac{9K_{max} + 8\mu_{max/}}{K_{max} + 2\mu_{max}}\right))^{-1}} \tag{3.13}$$

Where indices 1 and 2 refers to the stiff and soft material respectively, and K_{max} and μ_{max} represent maximum bulk and shear modulus respectively.

Regardless of the solid mixing model used, the density of a mixture (ρ_{mix}) between two or several solids, is given as the specific mineral densities (ρ) and their volume fractions (V) respectively:

$$\rho_{mix} = \rho_1 V_1 + \rho_2 V_2 \tag{3.14}$$

3.7 Mixing of fluids

The previous subchapter showed the importance of accounting for the geometrical distribution of grains, and not solely the composition and respective mineral fractions of the dry rock. Similarly, the effective elastic moduli of rocks are affected by fluid mixtures within pore spaces. Fluid mechanics indicate that a fluid seeks to avoid increasing fluid pressure by escaping to zones with lower pressure. This implies that a highly pressurized hydrocarbon fluid could gradually expel the original pore fluid in a reservoir. Meaning that the pore fluid of porous and permeable rocks may over time be replaced by other pore fluids, which is the case when highly pressurized carbon dioxide is injected into a storage reservoir. Being able to monitor the flow of pore fluids is therefore of significance to CO_2 injection, as fluid substitutions and mixtures influence the physical properties of the effective rock, thus the seismic character (Batzle and Wang, 1992).

3.7.1 The Gassmann model

The Gassmann model (1951) is used to predict the influence of a pore fluid on the effective elastic properties of a rock due to its simplicity and physical insight. Though it is important to also consider the attached assumptions when using Gassmann to derive effective properties. Assumptions involving uniform grain properties, open porosity and a homogeneous pore fluid that fully saturates the pore volume in a static condition. This implies that all pores are connected, and the fluid will make no resistance to shear deformation. Hence, the effective shear moduli of the saturated (μ_{sat}) and dry rock (μ_{dry}) are equivalent as shown in equation (3.15). The saturated bulk modulus is therefore only dependent on the porosity and the dry, fluid and solid bulk modulus as shown in equation (3.16).

$$\mu_{sat} = \mu_{dry} \tag{3.15}$$

$$K_{sat} = K_d + \frac{\left(1 - \frac{K_d}{K_s}\right)^2}{\frac{\phi}{K_f} + \frac{1-\phi}{K_s} - \frac{K_d}{K_s^2}} \tag{3.16}$$

where K_d is the dry rock bulk modulus, K_s is the solid rock bulk modulus, K_f is the fluid bulk modulus, and ϕ is the porosity.

3.7.2 Homogeneous versus patchy saturation

Fluids mix either as a homogeneous or patchy saturation. In case of a homogeneous mixture the original pore fluid in each pore is gradually substituted by another fluid. The bulk modulus can be expressed by Wood's (1955) equation, which is the equivalent to the Reuss model for grains:

$$\frac{1}{K_f^{(w)}} = \sum_{i=1}^{N} \frac{\mathrm{S_i}}{K_i} \tag{3.17}$$

Wood's equation indicates that if the properties of the individual fluids (K) and the respective volume fractions (S) are known, the properties of the mixture can be calculated (K_f).

Wood's equation shows that even small amounts of gas in a mixture with brine significantly lowers the bulk modulus and thus the seismic velocity in a reservoir.
Taking pressure and temperature into consideration, a pressure increase lowers the gas effect on seismic velocities, while the opposite applies for increasing temperatures as shown in Figure 3.7.1 and Figure 3.7.2. This indicates that in order for bright spots to occur at greater depths, the saturation of gas must be high (Batzle and Wang, 1992).

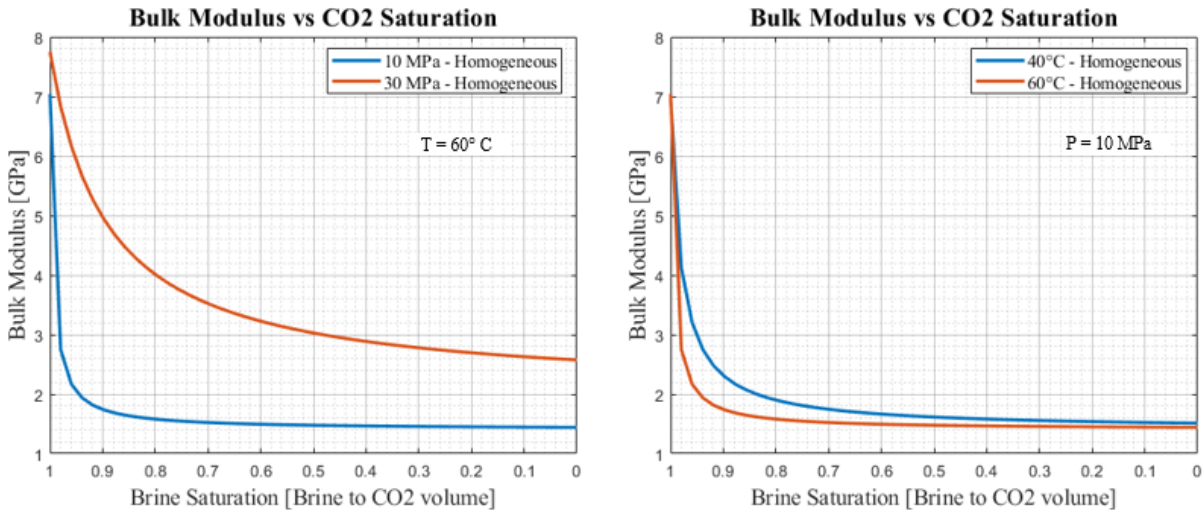

Figure 3.7.1: The bulk modulus of a homogenous mixture between brine and gas for different pressures (left) and temperatures (right). The x-axis is reversed, so that gas saturation increases to the right. A constant temperature of 60 °C is set for the different pressures, while a constant pressure of 10 MPa is set for the different temperatures.

Wood's equation is however only valid for immiscible fluids, as large quantities of gas are dissolvable in brine, reducing both the modulus and density of the fluid to a larger extent than the equation suggests. The same applies to light oils (Batzle and Wang, 1992). Another critical assumption to the homogenous mixing model is that different wave-induced pore pressures have time to flow and equilibrate among various fluid phases, therefore only being valid for fluid phases mixed at the finest scale (Mavko et al. 2009).

Conversely, if the fluids interfere in a patchy way the various pore volumes containing the original pore fluid are substituted locally at different times. The sizes of the various patches are small compared to the representative volume of pore space. As a consequence, the effective moduli of the rock get spatially varying bulk modulus and density while the shear modulus remain unaffected. To derive the effective bulk modulus of a patchy mixture

between two fluids, the Voigt model is used by replacing the moduli of grains with those of the fluids in equation (3.10) (Mavko et al., 2009).

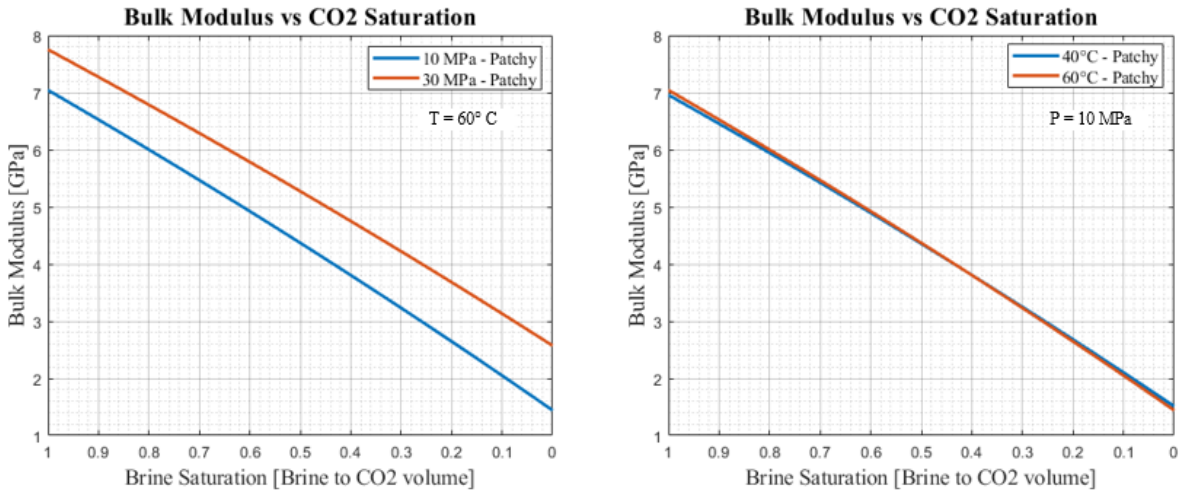

Figure 3.7.2: The bulk modulus of a patchy mixture between brine and gas for different pressures (left) and temperatures (right). The x-axis is reversed, so that gas saturation increases to the right. A constant temperature of 60 °C is set for the different pressures, while a constant pressure of 10 MPa is set for the different temperatures.

By comparing Figure 3.7.1 with Figure 3.7.2, it demonstrates that the choice of fluid modelling technique has a significant impact on the elastic properties of a rock. Especially considering small volume fractions of gas, whereas the elastic properties decrease substantially for a homogenous mixture while the trend is more or less linearly declining for a patchy mixture.

Moreover, the density of a fluid mixture is given as the sum of the separate fluid densities and their respective volume fractions, similarly to the grains of the dry rock in equation (3.14).

3.8 Rock physics modelling of reservoir rocks

The basis of rock physical modelling (RPM) has been described in detail previously. RPM is used to estimate reservoir properties from seismic data or to model seismic properties based on reservoir parameters. RPM is basically a forward modelling scheme used to better understand the expected elastic response to various hypothetical geological scenarios (Avseth, 2010).

Rock physics models try to describe the elastic moduli of complex subsurface formations mathematically. The models are specified by the volume fractions of the various constituents of heterogenous rocks, the elastic moduli of the various phases and the geometrical details of how constituents interact relative to each other. Because of the complexity of the subsurface structures and conditions, there exists a wide range of models that can be utilized in rock physical analysis. The choice of model depends on available data and the geological scenario under consideration. It is important to acknowledge the fact that all RPMs have certain advantages and limitations, or as stated by Box (1976): "All models are wrong, but some are useful". This implies that every model should be applied with caution to avoid erroneous results and interpretations. It is therefore necessary to analyze and classify previous studies of reservoir rocks, in order to ensure that the hybrid construction of RPMs provides the most representative results for a specific geological setting (Avseth et al., 2005; Nguyen and Nam, 2011).

This thesis uses the friable sandstone and patchy constant cement model as the rock physics modelling approach. Input data is calibrated from well log measurements at Sleipner and extracted from scientific papers characterizing the area of interest (Zweigel et al., 2000; Arts et al., 2008; Chadwick et al., 2004). The advantages and disadvantages of using the respective RPMs are discussed in chapter 7.

3.8.1 Friable sandstone model

The friable sandstone model describes the velocity-porosity behaviour of unconsolidated sandstones due to deteriorating sorting at a specific effective pressure. The model is based on Walton's (1987) contact theory (CT) for clean and well sorted sands, combined with a lower HSW bound to interpolate the elastic properties between the mineral point and the high porosity end member (Dvorkin and Nur, 1996; Avseth et al., 2005). The Hill model is used to model the effective solid, and a patchy mixing model is used to model the effective fluid. The effective saturated rock properties are calculated using Gassmann. The mineral point is assumed to have zero porosity with elastic properties equal to the effective elastic moduli of the rock forming minerals. Conversely, the high porosity end member modelled with Walton's contact theory is assumed to be located at the critical porosity point with elastic properties corresponding to spherical grains subjected to a confining pressure (Avseth et al.,

2005). As pressure is included in the Walton model, stress sensitivity caused by pressure variation is accounted for and minimizes the uncertainty of the interpolations (Appendix A).

3.8.2 Patchy constant cement model

The patchy constant cement model describes the porosity-velocity behaviour versus sorting at a specific cement volume, linked to specific depths where cementation occur. The model considers a cemented rock with a binary mixture of uncemented and cemented grain contacts, as described by Walton's contact theory and Dvorkin and Nur's (1996) contact cement theory (CCT) (Appendix A). The high porosity end member is modelled using a mixing model between contact -and contact cement theory, to account for both the stiffening effect induced by small fractions of cement and stress sensitivity related to loose grain contacts. The elastic properties between this well sorted end member and the zero porosity point are modelled with HSW bounds (Avseth and Skjei, 2011).

A lower HSW bound is used for minor cement volumes, while an upper HSW bound is used for higher cement volumes as all grain contacts are assumed to be cemented, hence the stress sensitivity vanishes. As a result, HSW bounds are able to link the soft and stiff components together to determine which part of the components is loadbearing. In other words, differentiate between cement occurring as part of the loadbearing structure or the intrinsic pore space. According to Avseth and Skjei (2011), the lower bound gives a good representation of sorting, while the upper bound gives a good description of contact cement.

Similar to the friable sandstone model, the Hill model is used to model the effective solid, while a patchy mixing model is used to model an effective fluid. Gassmann's model is further used to calculate effective saturated rock properties. For simplicity, the cement in the modelling consists of the same material as the effective mineral. Furthermore, the CCT model tend to overpredict the shear modulus, so a friction factor varying from 0 to 1 is included in the model. Thus, representing the boundary condition between no-friction and no-slip (Avseth and Skjei, 2011).
The properties of brine and CO_2 for both RPMs are based on Batzle and Wang (1992) and Span and Wagner (1996) respectively, while the mineral properties are based on Mavko et al. (2009). The modelling procedure of the RPMs is shown in Figures 3.8.1 and 3.8.2.

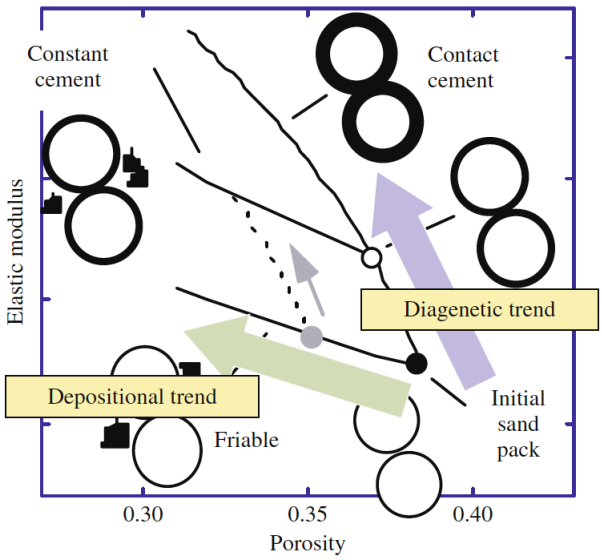

Figure 3.8.1: A theoretical illustration of the difference between the friable sandstone and patchy constant cement modelling approaches. Source: Avseth (2010).

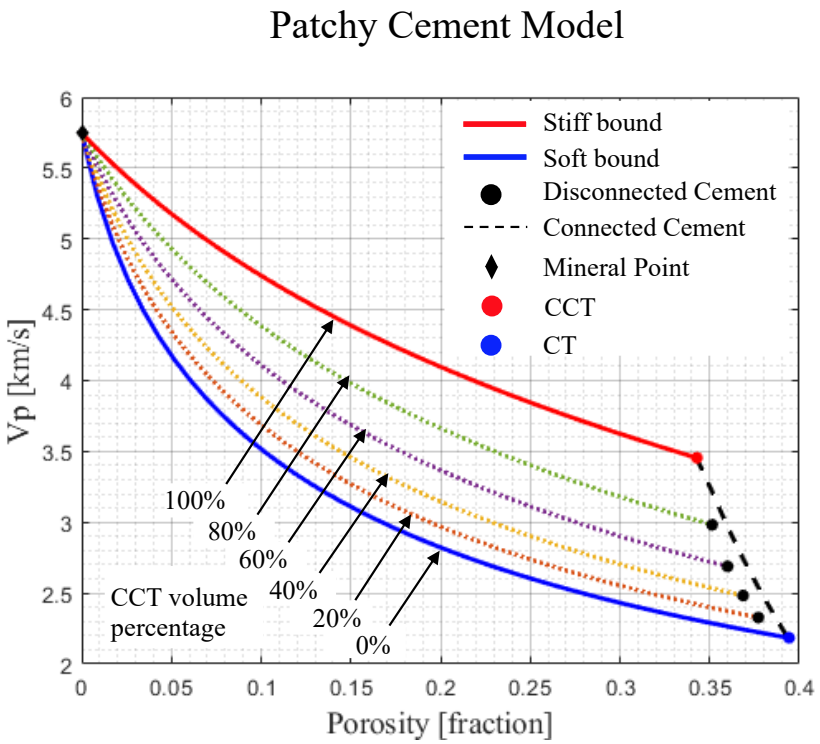

Figure 3.8.2: The patchy constant cement model for the Utsira reservoir. Elastic properties are interpolated as a function of porosity and CCT volume percentage. Vp is plotted as a function of porosity to illustrate an example, the modelling procedure is however the same for all elastic modulus.

3.9 Summary

Seismic reflections and amplitudes mirror contrasts between physical properties of rocks. The physical properties of rocks are affected by various factors including temperature and pressure, fluid -and mineral composition and texture, and the way constituents interact within the rock aggregate. Knowledge about how variations in these factors are linked with physical properties of rocks and its effect on seismic parameters, are therefore of severe importance for fully utilizing seismic data in reservoir monitoring of carbon sequestration. This provides insight on how changes in reservoir properties depict in geophysical data, enabling a link between seismic data and reservoir properties (Figure 3.9.1).

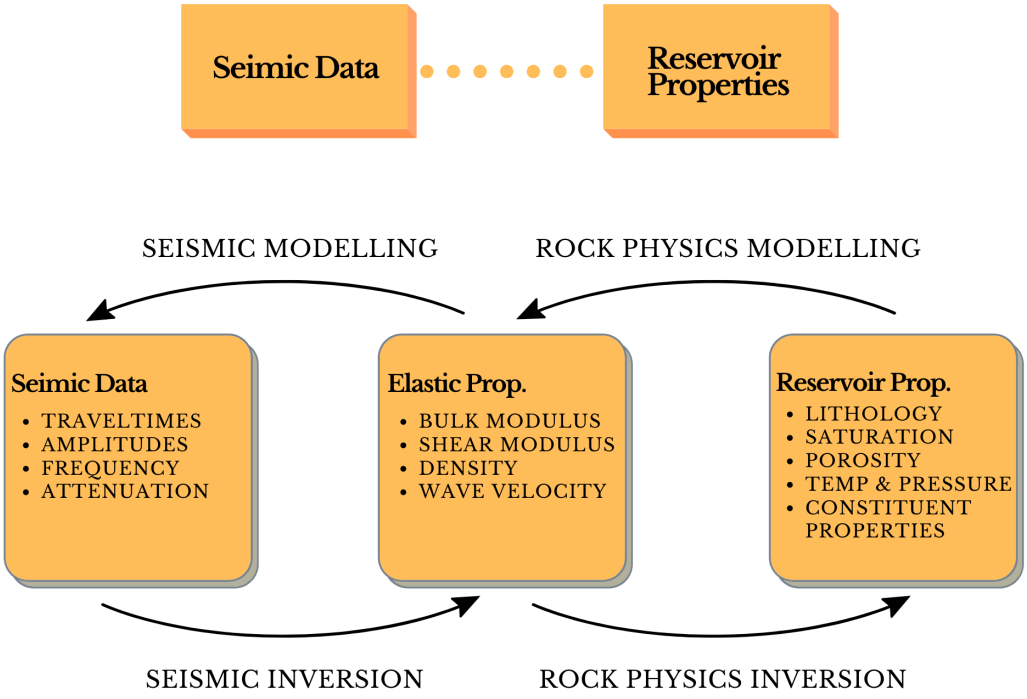

Figure 3.9.1: The connection between seismic data, elastic -and reservoir properties, linked together by rock physics -and seismic modelling and inversion. Modified from Bredesen (2012).

The chapter has highlighted the importance of understanding elastic wave theory, and incorporating rock physics and sedimentary geology as part of rock physical modelling to avoid erroneous interpretation of seismic data. Furthermore, how the choice of modelling techniques affect the physical properties of rocks.

4 Seismic attributes

4.1 Outline

Seismic attributes represent geophysical tools that can aid and strengthen quantitative seismic interpretation by utilizing physical principles to provide useful information about lithology, porosity and fluid saturation (Gelius and Johansen, 2010). This chapter presents AVO analysis, direct hydrocarbon indicators and alternative attributes. The majority of information presented in this chapter is based on Gelius and Johansen (2010).

4.2 AVO analysis and DHIs

Amplitude versus offset (AVO) is a technique that studies amplitude variations along a reflector as a function of offset. AVO analysis seeks to extract information about elastic velocities through simplified expressions of reflectivity, given as the reflection coefficient R_{pp}:

$$R_{pp} = \left[\left(b\frac{cos\theta_1}{V_{p1}} - c\frac{cos\theta_2}{V_{p2}}\right)F - \left(a + d\frac{cos\theta_1}{V_{p1}}\frac{cos\phi_2}{V_{s2}}\right)Hp^2\right]/D \tag{4.1}$$

where a, b, c, d, F, H, D represent various coefficients for the physical properties of rocks and incidence and reflection angles at interfaces. p is the ray parameter. The coefficients and ray parameter are defined in Appendix A.

Figure 3.2.2 showed that an incident ray generates both reflected P -and S-waves at an interface between two layers. This indicates that R_{pp} contains information about shear waves indirectly through conversion, even though the shear waves are not recorded at the surface in marine seismic. This can be explained by the fact that for a zero-offset trace, the reflectivity is equal to the P-wave reflectivity, and as the incidence angle increases along with offset, the influence of shear wave velocity increases accordingly due to the $\sin^2\theta$ term in equation (4.6) (Shadlow, 2014). AVO analysis can therefore provide separate shear and pressure information, acting as an indicator for V_p/V_s variations. This information is beneficial in terms of gas injections as the P -and S-wave reflectivities are poorly correlated due to a substantial decrease in V_p and a slight increase in V_s when substituting brine with CO_2. This makes the AVO technique a direct hydrocarbon indicator (DHI).

The AVO technique involves picking amplitude values in a NMO-corrected CMP-gather and plot these amplitudes as a function of offset to derive estimates of P and S-wave reflectivities. However, the Zoeppritz equations used to fit the experimental values to reflectivities are complicated and provide no physical insight of how amplitudes are related to seismic parameters. Therefore, simplified expressions of the R_{pp} providing physical insight are the key to success. An approach which provides physical insight involves combining a linearization of zero-offset P-wave reflection coefficient with Aki-Richards'(1980) and Wiggins' (1984) approximations. Hence, the zero-offset reflection coefficients for P -and S-waves are mathematically described as:

$$R_p = \frac{1}{2}\left[\frac{\Delta V_p}{V_p} + \frac{\Delta \rho}{\rho}\right] \tag{4.2}$$

$$R_s = \frac{1}{2}\left[\frac{\Delta V_s}{V_s} + \frac{\Delta \rho}{\rho}\right] \tag{4.3}$$

Based on equations (4.2) and (4.3), Aki-Richards' approximation gives:

$$R_{pp(\theta)} = \frac{1}{2}\left[\frac{\Delta V_p}{V_p} + \frac{\Delta \rho}{\rho}\right] - 2\left(\frac{V_s}{V_p}\right)^2 2\left[\frac{\Delta V_s}{V_s} + \frac{\Delta \rho}{\rho}\right]\sin^2\theta + \frac{1}{2}\frac{\Delta V_p}{V_p}\tan^2\theta \tag{4.4}$$

Assuming small angles ($\tan\theta = \sin\theta$) and $V_p/V_s = 2$, Wiggins' approximation gives:

$$G = R_p - 2R_s \tag{4.5}$$

$$R_{pp}(\theta) = R_p + G\sin^2\theta \tag{4.6}$$

The final equations (4.5) and (4.6) provide physical insight, as the P-P reflection coefficient is only dependent on the P-wave reflection coefficient (R_p), gradient (G) and angle of incidence (θ). Furthermore, if the gradient and reflection coefficients are known, the amplitude anomalies can be categorized into four different classes of gas sands by AVO cross plotting

the data. The cross plots are created with respect to the mudrock line, relating V_p to V_s for water saturated sandstone-shale systems, and Rutherford and William's (1989) classification scheme. An illustration of the AVO concept is shown below in Figure 4.2.1.

The first class of gas sands is usually associated with areas onshore and is characterized as high impedance sand. The second class is associated with both onshore and offshore settings and has an impedance contrast close to zero between shale and sand. The third and fourth classes of gas sands are associated with marine environments, and are defined as low impedance sands. How the amplitudes changes with offset for each class of gas sand can be observed in Figure 4.2.2.

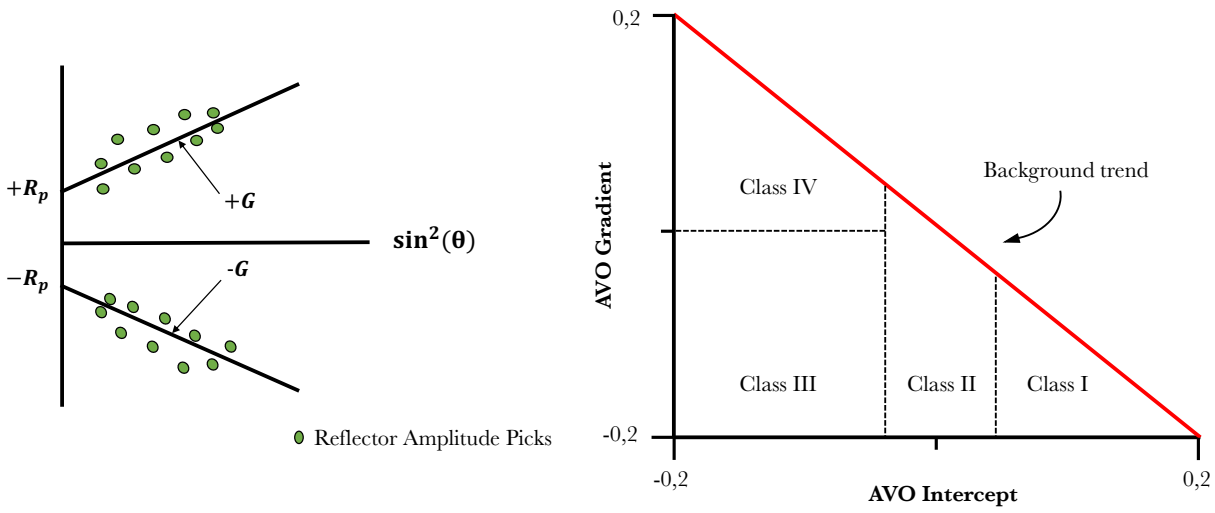

Figure 4.2.1: The concept of AVO-analysis: picking amplitude values along a reflector of interest and fit these values to theoretical P-P reflection coefficients, and thereby plotting the data as a function of incidence angle (left). Furthermore, determine which class of gas sand the anomalies represent by plotting gradient as a function of intercept (right). The background trend (red) are made from combining the AVO gradient, equation (4.2), Gardner's equation (1974), and the slope of the mudrock line (Gelius and Johansen, 2010).

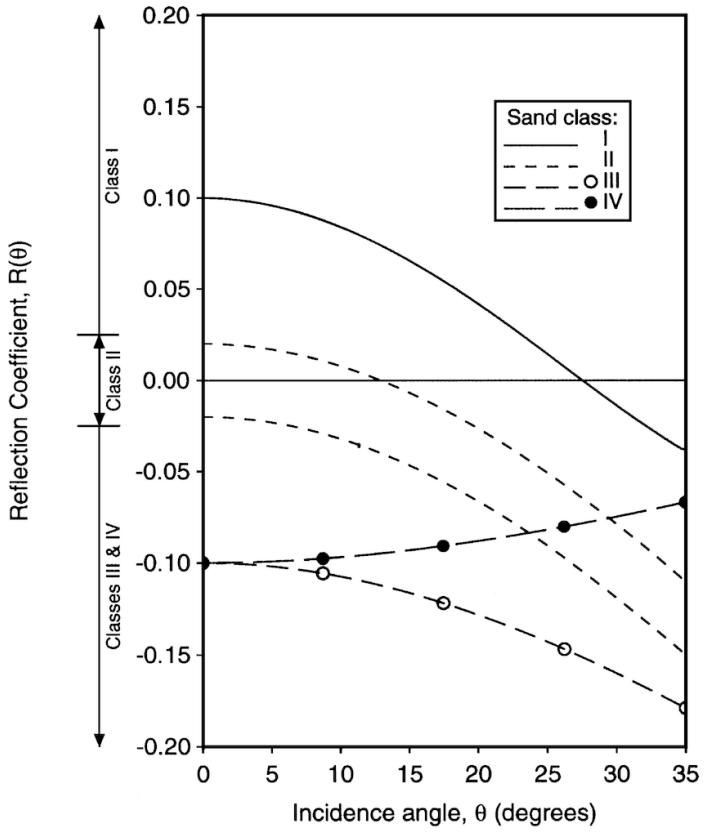

Figure 4.2.2: Reflection coefficients at the top of each class of gas sand as a function of incidence angle. Class 2 has both a negative and positive intercept, though the trend remain the same. Source: Castagna et al. (1998).

Since DHIs represent full stack amplitude anomalies, DHIs can be formed from AVO effects. Hence, the relationship between DHIs and AVO classes can be summarized beneath in Table 4.1 (Shadlow, 2014). The various DHIs can be observed in Figure 4.2.3.

Table 4.1: A classification scheme for direct hydrocarbon indicators.

DHI classification	AVO class
Dim spot (dimming peak with offset)	Class I, II
Phase change (peak to trough with offset)	Class II, III
Bright spot (increasing trough with offset)	Class III, IV

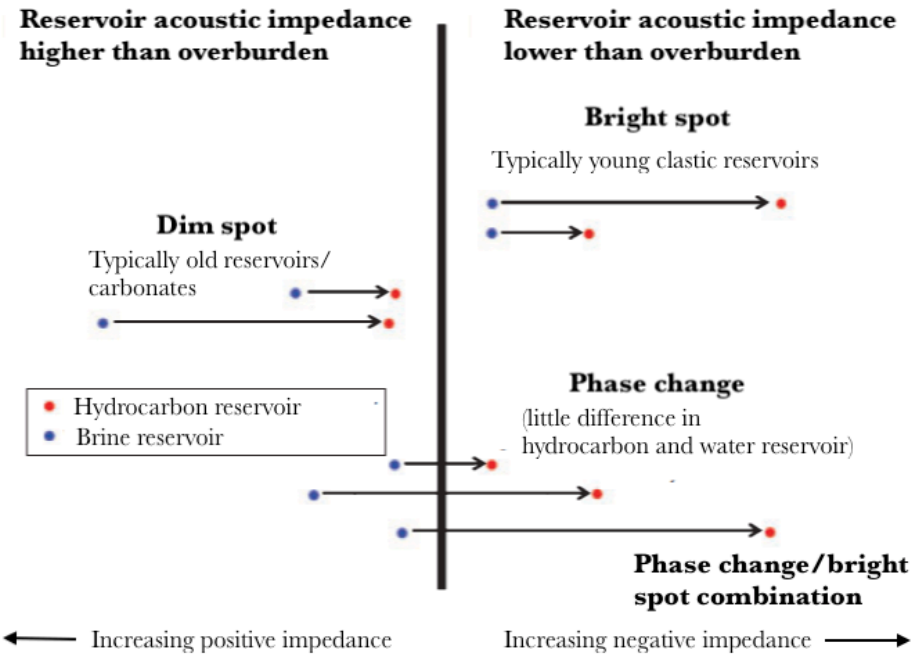

Figure 4.2.3: The acoustic impedance change for different DHIs. All DHIs are due to a decrease in acoustic impedance. The blue dots represent brine saturated reservoirs, and the red dots represent hydrocarbon saturated reservoirs. The movement from left to right demonstrates the change in reservoir properties as a result of fluid substitution from brine to hydrocarbons. Modified from Shadlow (2014).

4.3 Alternative attributes

Besides the fact that AVO-analysis is the main focus in this thesis, there exists a wide range of seismic attributes that can assist the analysis of AVO effects, thus strengthen the seismic interpretation. A very brief introduction to some alternative and frequently used attributes is presented below. This includes rock physics templates (RPT) and the lambda-mu-rho (LMR) method.

RPTs were introduced by Ødegaard and Avseth (2004) for effective reservoir characterization. The RPTs represent rock physics models constrained by local geological factors, and are created by doing forward rock physics modelling. This creates theoretical trendlines that are representative for an area of interest which are able to distinguish between various lithologies, fluids and porosities. By scatter plotting the observational data acquired

from well logs, predictions of lithology, fluid saturation and porosity can be made (Avseth et al, 2005; Ganguli, 2017).

However, the reliability of the RPT strongly depends on the quality of input data and model assumptions (Ødegaard and Avseth, 2004). V_p/V_s ratio plotted as a function of acoustic impedance is the most commonly used RPT. An RPT including the theoretical trendlines for idealized siliciclastic lithologies, fluid saturations and porosities is shown in Figure 4.3.1.

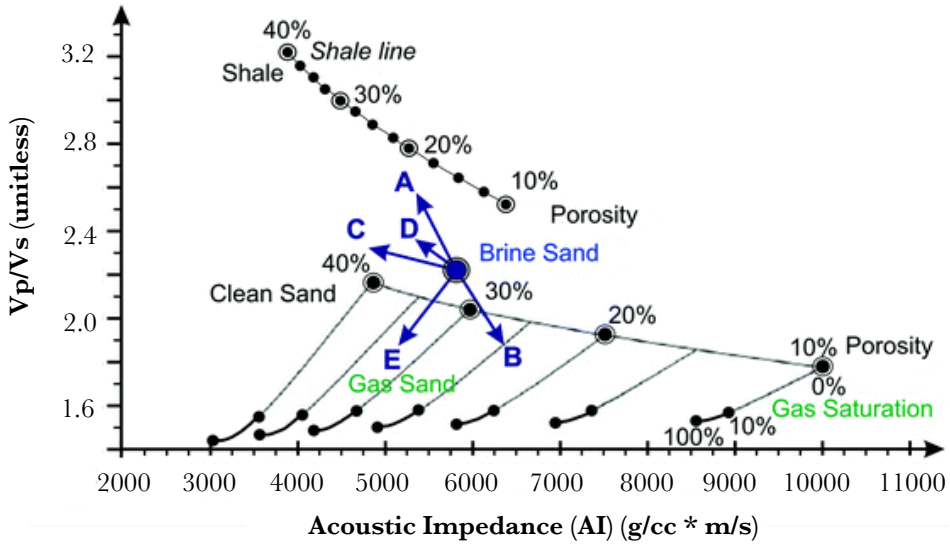

Figure 4.3.1: An idealized rock physics template with V_p/V_s plotted as a function of acoustic impedance. The blue arrows in the rock physics template indicate various trends: A=increasing shaliness, B= increasing cement, C= increasing porosity, D= increasing pore pressure, E= increasing gas saturation. Modified from Ganguli (2017).

On the other hand, the LMR method isolates and relates the incompressibility of an effective rock to its rigidity by using Lamé parameters. The method is therefore able to differentiate between lithological and fluid variations, as the separate lithologies and fluids have characteristic incompressibilities and rigidities. Rigidity separates lithologies while incompressibility separates fluids, as shown in Figure 4.3.2.

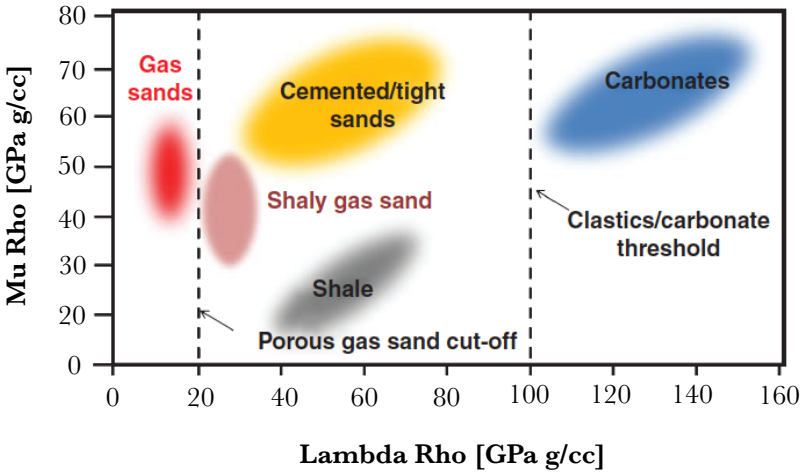

Figure 4.3.2: A typical LMR plot with Mu Rho plotted as a function of Lambda Rho. The general positioning of datapoints representing different lithologies saturated with various fluids is highlighted by separate coloured clouds. Modified from Shadlow (2014).

4.4 Summary

Seismic attributes represent useful techniques to connect seismic signatures to geological trends. AVO analysis studies amplitudes as a function of offset, revealing beneficial information about velocity ratio and acting as a DHI. Furthermore, the intercept versus gradient crossplot is used to link the various amplitudes to classes of AVO anomalies. Additionally, RPTs and LMR-method may be used to distinguish various lithologies, fluid saturations and porosities.

This shows the value of using seismic attributes to strengthen seismic interpretation and avoid ambiguities related to fluid fill, lithology, porosity and other geological factors influencing the seismic response.

5 Seismic signatures of CO_2 – injection: Numerical examples

5.1 Outline

This chapter will give a demonstration of well log calibration when calibrating a RPM. The chapter will also use numerical examples to illustrate seismic signatures of carbon dioxide injections linked to various hypothetical geological scenarios. The various scenarios mimic the geological setting at Utsira, characterized as a highly porous sandstone reservoir overlain by a low permeable caprock of shale. AVO-analysis, the effect of lithology and reservoir properties, in addition to the effects of pressure, fluid saturation and distribution on seismic responses are presented. Knowledge about how seismic signatures are linked to various factors strengthen the understanding of how CO_2 injections influence seismic data. This makes it easier to recognize similar events on time-lapse seismic.

5.2 Well log calibration

This subchapter was written in cooperation with fellow master student Sondre Kåstad.
Calibrating an RPM in practice requires input data that are usually based on acquired well log data. Data including information about lithology, porosity, density and velocities. The well log measurements used to calibrate an RPM in this thesis are extracted from well 15/9-13, acquired from the Sleipner East Field in the North Sea (NPD, 2021a).
As the measurements from well 15/9-13 were inconsistent, and unreliable in certain intervals, several assumptions had to be made in order to obtain more useable well log data. The data was considered unreliable in certain intervals due to the fact that the caliper log values exceeded the upper limit of 23 inches on the log in combination with unrealistically high P-wave velocity values. By reviewing the geological history of the area, the sedimentary formation of interest consists of friable sand, indicating that the unreliability is likely related to overbreak which causes disturbances to the measurements (Jullum and Kolbjørnsen, 2016; Zweigel et al., 2004; Bøe et al., 2002). This affects not only the caliper log values, but also densities, porosities and velocities. Additionally, neither a resistivity or S-wave velocity log were recorded in the original well log.

The well log calibration process was extensive and involved several steps, summarized and numbered below:

(1) A lithology log was made based on the assumption that a gamma ray log value of 40 represented clean sand, while a value of 90 represented clean shale. The resulting well log was

ranged from 1 to 0, from clean shale to clean sand respectively. In well log analysis it is commonly understood that a gamma ray log value of 60 differentiates between sand and shale, so this was used as a basis for determining the upper and lower limits.

(2) A porosity log was made based on the well log -and fluid density in addition to a matrix density. The matrix density was derived from the mineral densities and fractions extracted from Mavko et al. (2009) and Chadwick et al. (2004), linked with the lithology log from the previous step. Given that the reservoir represents a saline aquifer, it was also assumed that the reservoir was fully water saturated prior to CO_2 injection, hence the fluid density was equivalent with saline water (ρ=1.03 g/cm^3). The porosity log was also connected to the caliper log, defined with an upper limit of 20 inches, to obtain a more representative log. All values above the upper limit were then neutralized to a porosity value between 1% and 40% depending on the volume fraction of shale, while values below were considered to be reliable. The porosity limit of 40% was based on data presented in Chadwick et al. (2004), while the lower limit of 1% was determined based on cross plot data.

(3) As certain intervals still yielded unrealistic porosities of 70-90%, the porosity log was modified to have an absolute upper limit of 40%, similar to the porosity limit defined in Chadwick et al. (2004) for the Utsira Fm.

(4) An updated density log was created based on the porosity log, fluid -and matrix density from the previous steps.

(5) As the interval of interest contained unreliable data, a new P-wave velocity log had to be calibrated. The calibration was based on Walton's contact theory, providing good velocity predictions for shallow unconsolidated rocks (Andersen and Johansen, 2010).
The S-wave log was first modelled with Walton and polyfitted to the calibrated P-wave velocity log. Further, the original P-wave velocity log was then used to derive the new S-wave velocity log. As a result, the calibrated Vs log is not only influenced by the rock physics model, but also by the V_p log.

(6) Finally, new bulk and shear modulus were calculated based on the calibrated velocities and density logs.

The calibrated logs were used as a basis for calibrating the RPM used in this thesis. Plots illustrating the differences between the original and calibrated well logs, and the RPM's ability to predict density, bulk and shear modulus for the caprock, reservoir and below, are shown in Appendix B. The calibrated input in the RPMs for the caprock, reservoir and below are summarized in Table 5.2.1. Some calibrated well log data is presented in Figure 5.2.1.

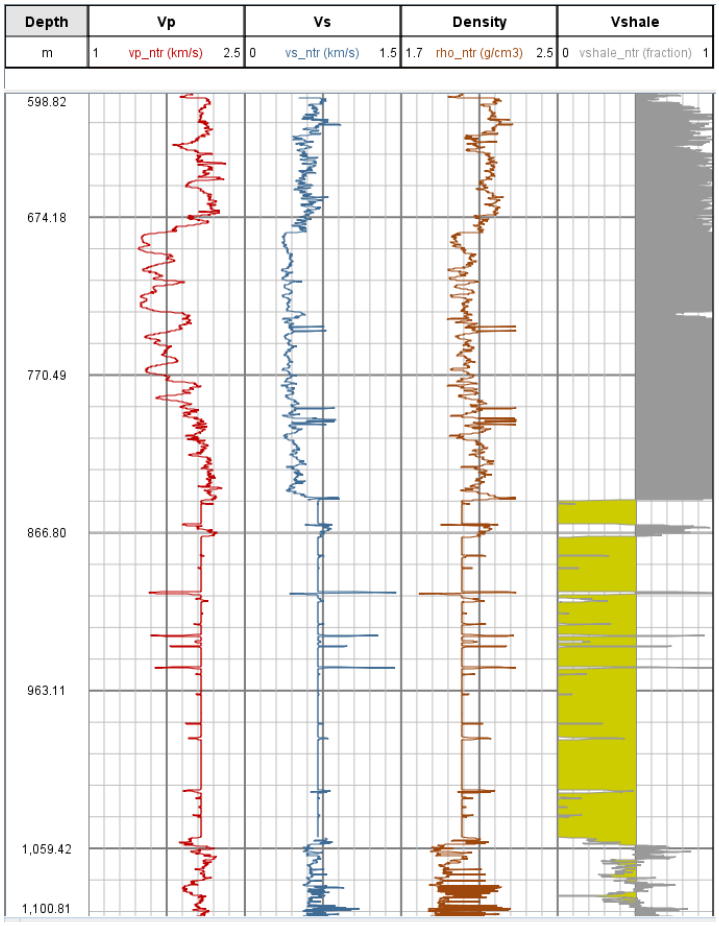

Figure 5.2.1: Calibrated elastic velocities, density and Vshale logs for Well 15/9-13. The Utsira reservoir stretches from 850 – 1050 m, marked by the thick sequence of sandstone (yellow).

Table 5.2.1: The calibrated RPM input for the caprock, reservoir and below.

Properties	**Caprock**	**Utsira Reservoir**	**Below**
Sand Bulk Modulus	30.28	38.99	20.00
Sand Shear Modulus	45.75	36.66	41.49
Sand Density	2.66	2.66	2.66
Shale Bulk Modulus	10.25	12.00	17.70
Shale Shear Modulus	2.00	8.00	6.55
Shale Density	2.3	2.3	2.3
Vol. Frac. Shale	1	0	0.5
Eff. Porosity	0.2	0.4	0.3
Friction Factor	0.0086	0.1	0.25

The calibrated rock physics model for the Utsira reservoir is in correspondence with information presented in other scientific papers and can therefore be considered reliable (Chadwick et al.,2004; Zweigel et al., 2000; Arts et al., 2008). Furthermore, the P-wave velocity and density logs used to calibrate model input show similarities to the logs presented by Rabben and Ursin (2011). The same applies to the physical properties of the sand grains. The physical properties of the shale grains are however more uncertain, though Chadwick et al. (2004) provide the mineral composition of the caprock. Based on the fact that the caprock contains significant amounts of kaolinite indicate that the properties of shale are soft nevertheless. Chadwick and Eiken (2013) also stated that the porosity of the caprock is roughly 30%, though the calibrated porosity log indicate a porosity value of 20%. The sequence below the reservoir is less studied, so a comparison of physical properties are difficult. Nonetheless, it is calibrated from the same well log data which provides reliability.

5.3 Scenario specifications

The scenarios illustrated below are all based on the geological setting at the Utsira storage site, represented as the basis scenario (or scenario 1). Scenario 2 highlights how changing the lithology and reservoir properties affect the seismic reflections. Scenario 3 demonstrates the effect of increasing the gas saturation and pore pressure. Scenario 4 contains a buoyant and gradually increasing CO2 plume, migrating from the lowermost sand package and into the top Utsira layer by penetrating the intra-layering shales in the reservoir zone. A more detailed description of the specific layers is provided in the case study in chapter 6. The friable sandstone model was used for all scenarios except scenario 2b involving cementation. The patchy constant cement model was used for the cementation scenario. An introduction to each scenario, together with simple illustrations, is provided below.

The basis scenario consists of a highly porous, permeable and clean sandstone reservoir underlain and overlain by a sandy-shale and clean shale unit respectively (Figure 5.3.1). All layers are assumed to be saturated with brine, similar to Utsira before CO_2 was injected. The temperature is set to 41°C with an effective pressure of 10 MPa, similar to information in Arts et al. (2008).

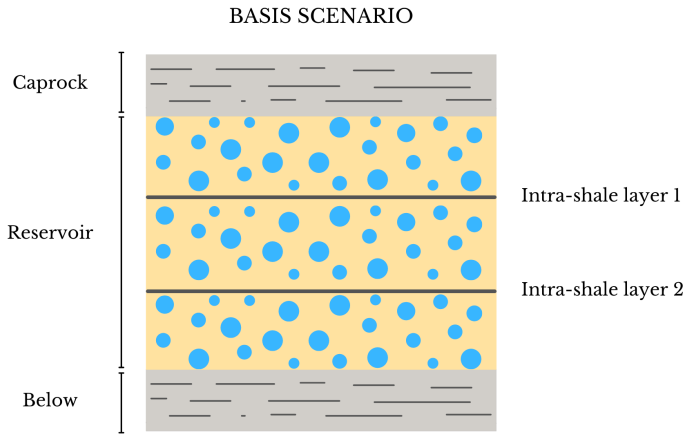

Figure 5.3.1: An illustration of the geological setting at Utsira during the pre-injection phase. The blue dots indicate pore spaces filled with brine.

Scenario 2a describes a setting where the shale content in the reservoir is increased compared to the basis scenario (Figure 5.3.2). The explanation for studying the effect of shaliness could be lateral lithological variations, slightly deviating from well log and core cutting observations.

Furthermore, by moving the setting down to 2 km depth, it is assumed that cementation occurs as the temperature and pressure increase to approximately 70 °C and 20 MPa. As a consequence, all layers are modelled to contain small fractions of cement (Figure 5.3.2). Both mechanical compaction and cement fraction will reduce the porosity accordingly. A motivation for studying the effect of cement is to study the seismic signature of injections in a deeper, more consolidated target. This correspond to scenario 2b.

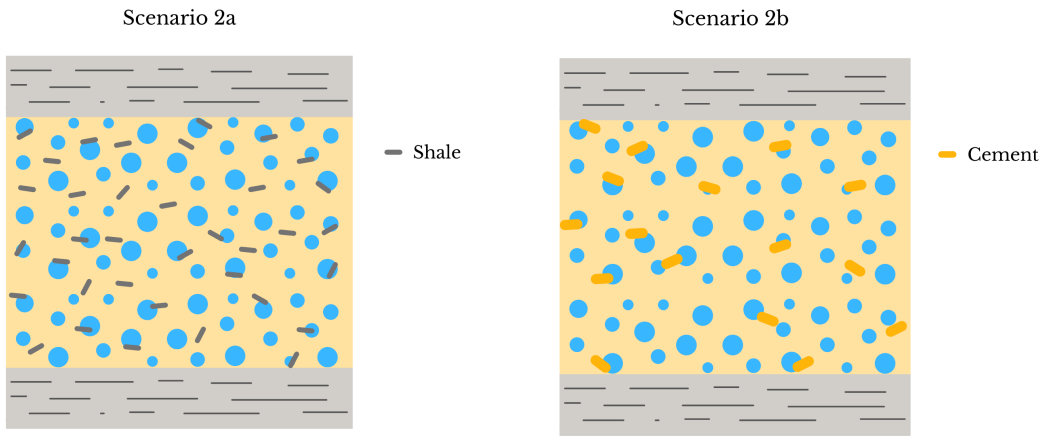

Figure 5.3.2: Simple illustrations of the Utsira reservoir containing shale (left) and cement (right). Shale particles are marked with black, while cement is marked in dark yellow.

Scenario 3 increases the gas saturation of CO_2 in the reservoir and simultaneously account for the increasing pore pressure (Figure 5.3.3). For this scenario, it is assumed that the pore pressure increase is equal throughout the reservoir unit, even though this is presumably most representative near the injection point, from which it will gradually decline both laterally and vertically due to the large pore volumes in the Utsira Fm. (Chadwick and Eiken, 2013). No leakage into the caprock is assumed. The explanation behind studying this scenario is that during the life cycle of a CO_2 sequestration project the majority of pore spaces will eventually be saturated with CO_2, and the pore pressures increase as the gas continues to be injected into the reservoir unit.

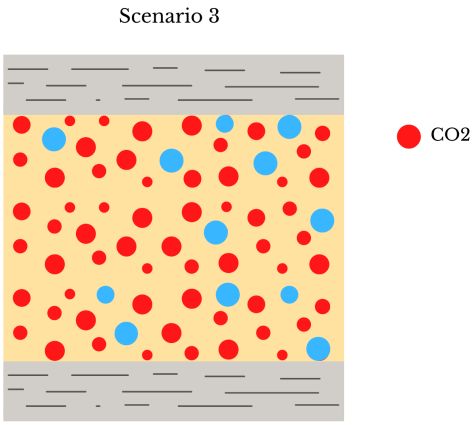

Figure 5.3.3: An illustration of the reservoir injected with CO_2 (red) in a patchy mix with brine (blue).

Scenario 4 studies fluid distribution patterns. The scenario imagines an increasing CO_2 plume gradually migrating through the intra-layering shales to the top of the reservoir (Figure 5.3.4). It is assumed that only the lowermost sand package is saturated with CO_2 during the first event. In the second event, it is assumed that the gas has migrated through the first intra-layering shale and into the sand package above. Furthermore, it is imagined that the carbon dioxide has migrated through both the intra-layering shales and into the uppermost sand package in the final event. It is assumed that the intra-layering shales act as barriers against the upwards migration of CO_2, as stated by Arts et al. (2008).
The reason for studying the effect of fluid distribution patterns is that this resembles a real life scenario of a growing CO_2 plume from an early injection phase to a mature injection phase, providing insight to how amplitudes change over time.

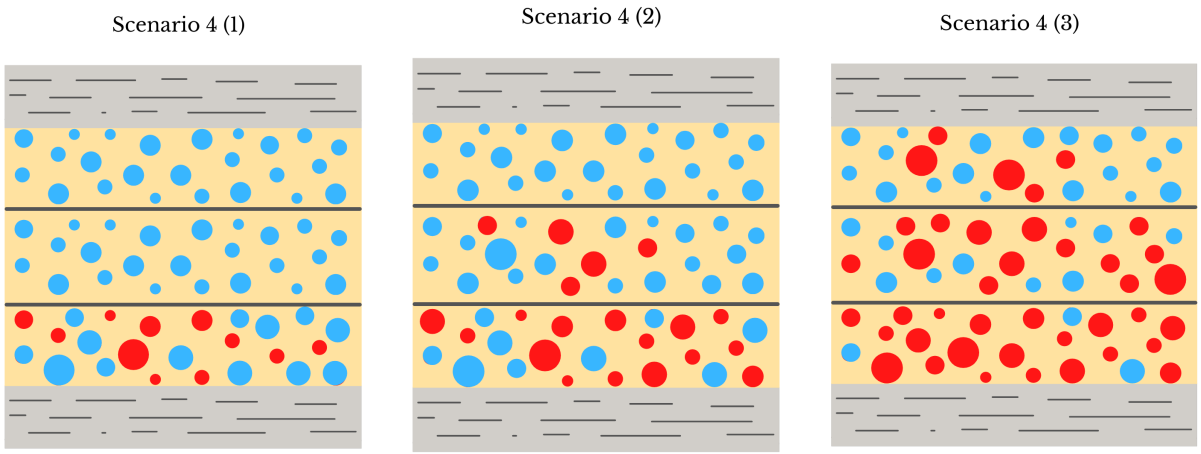

Figure 5.3.4: Simple illustrations of a growing CO_2 plume, from an early injection phase (left) to a mature injection phase (right). The CO_2 migrates through the semi-permeable barriers of shale with time.

5.4 Reflectivity and Amplitude Versus Offset (AVO)

As mentioned in the previous chapter, AVO analysis act as a useful tool to geoscientists doing seismic interpretation as it can reveal useful information about reservoir conditions. By studying the AVO intercept versus gradient, a trend plot linking amplitudes to changes in reservoir pressure, porosity, lithology and gas saturation can be created (Figure 5.4.1).

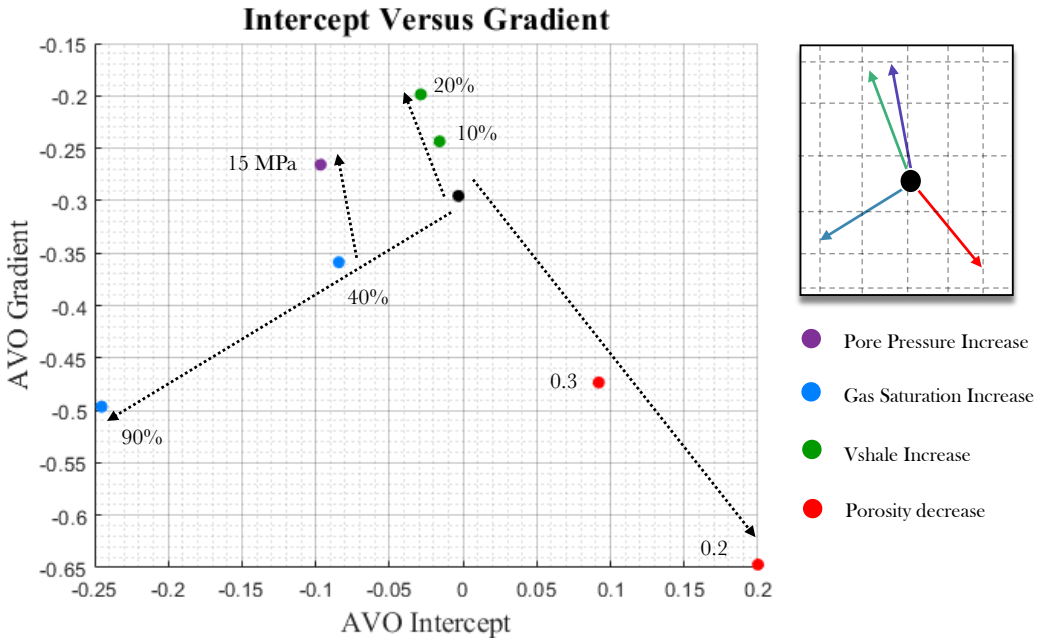

Figure 5.4.1 : An AVO crossplot showing the various trends for changes in saturation (blue), porosity (red), shaliness (green) and pore pressure (purple) compared to the basis scenario (black). The trends are highlighted in the minor box to the right, with the different arrows corresponding to the different trends. The pore pressure (purple) was increased when the reservoir was saturated with CO_2.

The trend of increasing the cement fraction within the reservoir is shown in Figure 5.4.2.

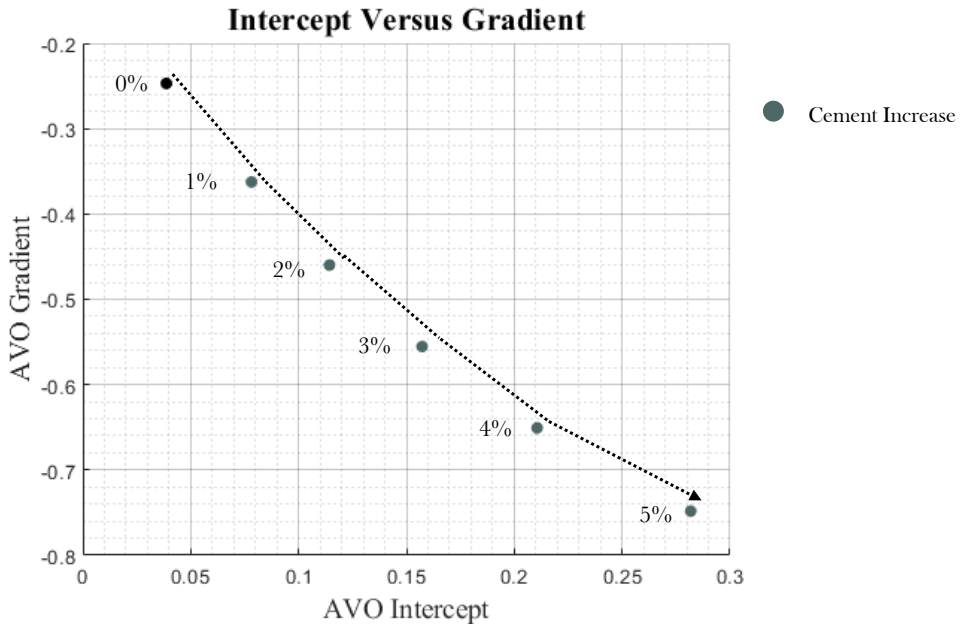

Figure 5.4.2: An AVO crossplot showing the trend of increasing the cement fraction in the reservoir model. AVO gradient is plotted as a function of intercept. The black dot represent the reservoir at 2 km depth with 0% cement, while the green dots represent cement fractions from 1-5%, increasing in the direction of the black arrow.

The trends observed in Figures 5.4.1 and 5.4.2 can be summarized as follows:

- Increasing the pore pressure in a reservoir significantly increases the gradient, and slightly decreases the intercept.
- Decreasing the porosity in a reservoir significantly decreases the gradient and increases the intercept significantly.
- Increasing the gas saturation of CO_2 in a reservoir decreases both the gradient and intercept significantly.
- Increasing the shaliness in a sandstone reservoir largely increases the gradient and slightly decreases the intercept.
- Increasing the cement fraction in a sandstone reservoir decreases the gradient and increases the intercept. However, with increasing cement fraction the AVO intercept increases more than the gradient decreases.

5.5 Effects of lithology and reservoir properties

In order to observe the effect of adjusting model input, the seismogram for the basis scenario needs to be introduced. All seismograms are generated with a zero-phase Ricker wavelet of 30 Hz which peaks at the arrival time. Furthermore, geometrical spreading and anelastic attenuation are excluded, though its effect on amplitudes will be discussed in chapter 7. All amplitudes are downscaled by 25 dB to fit within the frame of the seismograms. In Table 5.5.1 the survey geometry is given, in addition to the geological model used in Figure 5.5.1. Only P-P reflections from the top to base Utsira are accounted for, the remaining uppermost layers are only included to preserve the two-way traveltime observed on seismic sections from Sleipner. Due to practicalities and a desire to minimize the complexity of the geological setting, the interfaces between the layers are horizontal. The reason for doing so is to isolate and highlight the effect of each adjustment on seismic amplitudes, and avoid dipping reflectors and interference.

Table 5.5.1: The synthetic seismic survey setup

Nr. Of Shots	1
Min Offset	0 km
Max Offset	1.5 km
Receiver Increment	0.05 km
Nr. receivers per shot	30
Incidence angle range – top Utsira	0 – 14 (Near) 14 - 28 (Mid) 28 - 41 (Far)
Incidence angle range – base Utsira	0 – 12 (Near) 12 - 24 (Mid) 24 - 35 (Far)

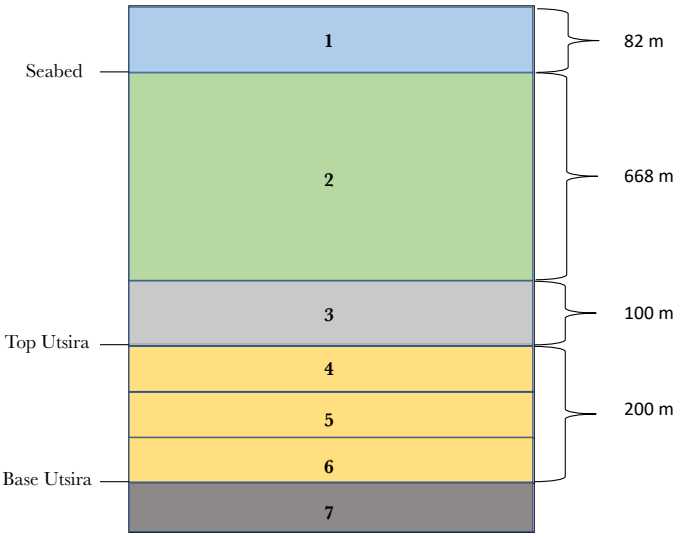

Figure 5.5.1: The geological model used to produce seismograms, with layer thicknesses presented to the right. The two uppermost layers represent the seawater column and the transport layer respectively. The remaining layers consists of the lowermost caprock at the top, followed by three equally thick sandstone packages representing the reservoir, and a shaly unit beneath the Base Utsira.

The seismogram for the basis scenario is shown in Figure 5.5.2. The polarity of the seismic signals is presented to the right.

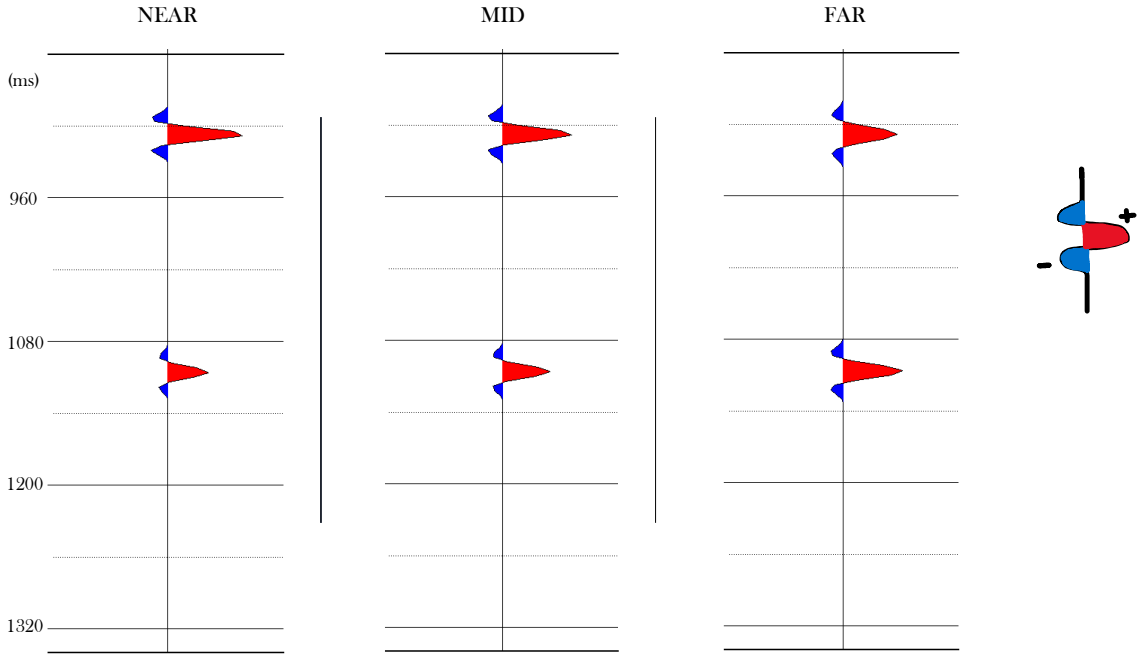

	Vp (km/s)	ρ(g/cm^3)
Caprock	1.86	2.05
Reservoir	2.03	2.01
Below	2.06	2.05

Figure 5.5.2: An NMO-corrected CSP-gather for the basis scenario, attached with P-wave velocities and densities for the respective layers.

The reflections for the basis scenario are strong, and can be explained by the soft properties of shale in the reservoir model. Furthermore, the acoustic impedance increases downwards, resulting in strong positive reflections for each interface. The amplitudes for the top reflector slightly decrease with increasing offset, while the opposite apply to the bottom reflector.

By increasing the shale content in the reservoir from 0% to 20%, a porosity reduction from 40% to 35% is obtained. Other input parameters are held constant. The effect of shaliness corresponds to scenario 2a, and the resulting seismogram is shown in Figure 5.5.3.

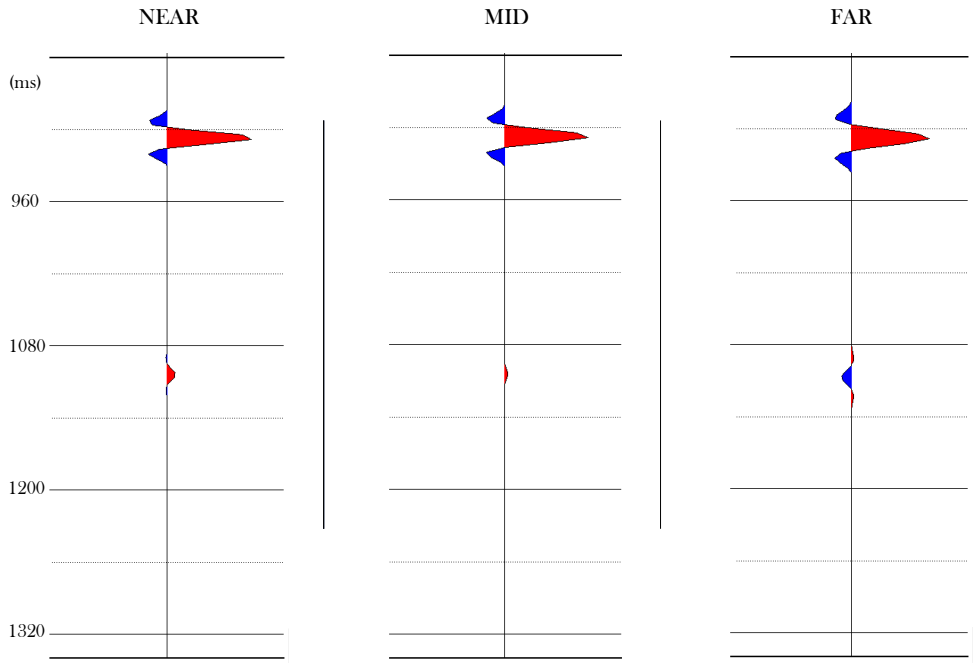

	Vp (km/s)	ρ(g/cm^3)
Caprock	1.86	2.05
Reservoir	**2.05**	**2.04**
Below	2.06	2.05

Figure 5.5.3: An NMO-corrected CSP-gather for the scenario with increased shaliness in the reservoir, attached with P-wave velocities and densities for the respective layers. The changed reservoir properties are highlighted in black.

By comparing the reflections with the basis scenario, the bottom reflector is weakened by the increasing shale content, while the upper reflection is slightly stronger. The trend of a decreasing amplitude with offset is however the same for both reflections. Additionally, the polarity changes for the bottom reflection in the far stack, implying that the polarity is reversed for large offsets. This is in accordance with Avseth et al. (2005), which state that

increasing the shale content within a sandstone reservoir increases its physical properties and thereby weakens the amplitudes in seismic reflections. This assumes that the surroundings are stiffer originally.

Moreover, by moving the geological setting down to 2 km depth, a cementation process initiates. Here, it is assumed that each layer contains 2% cement, and that the porosity decreases for all layers both due to mechanical and chemical compaction. However, it is assumed that mechanical compaction influences the porosity in shale more than sand, and vice versa for chemical compaction (Figure 3.5.2). The porosity in the caprock is reduced from 20% to 15%, while the porosity in the reservoir is reduced from 40% to 35%. The porosity in the unit below is reduced from 30% to 24%. The effect of cement corresponds to scenario 2b, and the resulting seismogram is shown in Figure 5.5.4.

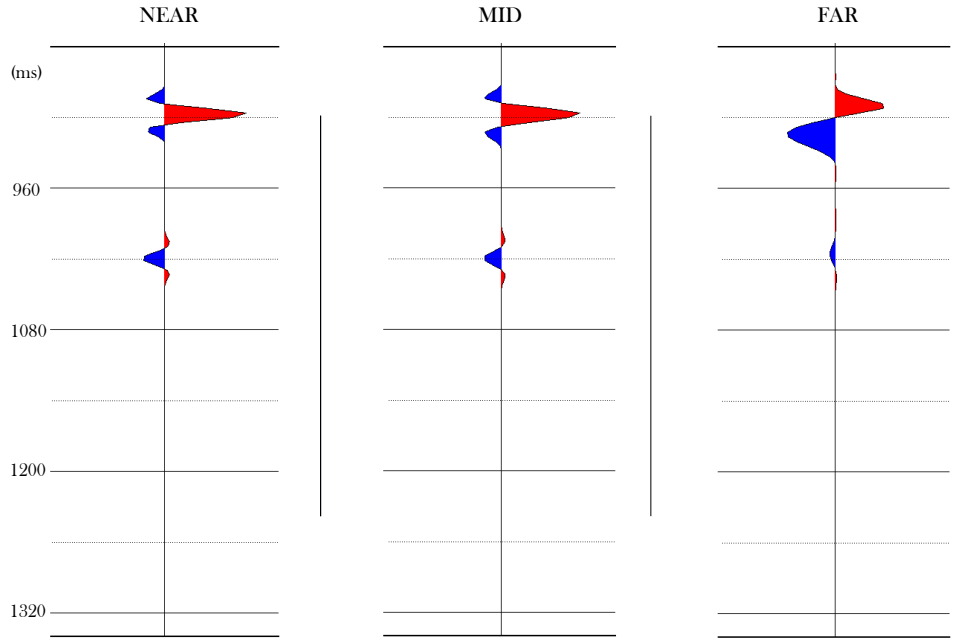

	Vp (km/s)	ρ(g/cm^3)
Caprock	2.04	2.11
Reservoir	**3.30**	**2.09**
Below	2.82	2.13

Figure 5.5.4: An NMO-corrected CSP-gather for the scenario with cement in all layers, attached with P-wave velocities and densities for the respective layers. The changed reservoir properties are highlighted in black.

The cement clearly stiffens the physical properties of each layer in the model. By doing so, the cement both reverses the polarity and attenuates the amplitudes for the bottom reflector compared to the basis scenario. Due to the soft properties of the caprock, the top reflector still remains strong without any noticeable changes compared to the basis scenario. However, the far stack for the top reflector deviates from the basis scenario as a sudden amplitude increase occurs. This indicates that all the energy within the seismic waves have been reflected as the critical angle is reached. Similar to both the previous examples, and excluding the far stack response for the top reflector, the amplitudes decreases with offset. A time-shift of approximately 90 ms also occurs for the bottom reflector, due to the enhanced seismic properties of the layers in the model reducing the two-way traveltime remarkably.

5.6 Effects of saturation and pressure

Injecting CO_2 into a saline aquifer will most likely reduce the effective pressure and increase the pore pressure in a reservoir. As observed in Figure 3.7.2, the amount of gas within pore spaces would also have a very strong influence on the seismic properties in the reservoir, thereby reducing the acoustic impedance for the reservoir significantly. By assuming a gas saturation of 90% and a uniform pore pressure of 15MPa, a seismogram accounting for saturation and pressure effects is created. The effect of saturation and pressure corresponds to scenario 3, and the resulting seismogram is shown in Figure 5.6.1.

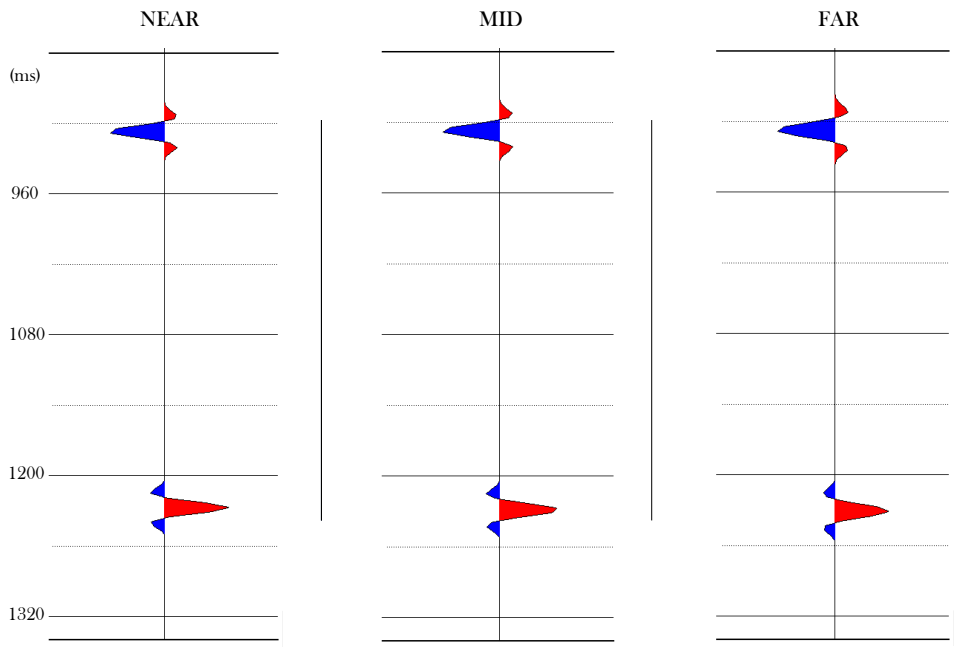

	Vp (km/s)	ρ(g/cm^3)
Caprock	1.86	2.05
Reservoir	**1.26**	**1.92**
Below	2.06	2.05

Figure 5.6.1: An NMO-corrected CSP-gather for the third scenario with high gas saturation and increased pore pressure, attached with P-wave velocities and densities for the respective layers. The changed reservoir properties are highlighted in black.

The reflections and amplitudes are very strong for all offsets within the domain, most likely due to the significant decrease in Vp and density for the reservoir. Compared to the basis scenario, the top reflector in scenario 3 has changed polarity to an even stronger negative reflection, while the polarity for the bottom reflector remains the same. The amplitudes for the bottom reflector slightly decreases with offset, while the opposite applies to the top reflector.

5.7 Effects of fluid distribution patterns

By gradually injecting CO_2 into the three layers of sand in the reservoir, the time-lapse effect and fluid distribution patterns are presented. It is assumed that for each event, as the gas saturation increases within the reservoir layers and migrates upwards, the pore pressure also increases. To what extent the pore pressure increases depends on the gas saturation within each layer. The effect of fluid distribution patterns corresponds to scenario 4, and the resulting seismograms are shown in Figures 5.7.1 - 5.7.3, from the first to final event respectively. No leakage into the caprock is assumed.

The first event assumes that only the lowermost layer of sand is saturated with CO_2. The exact gas saturation is set to 40% with an assumed uniform pore pressure of 13MPa. The remaining two sand packages above are assumed to be equal to the basis scenario. The seismogram for the first event can be observed in Figure 5.7.1.

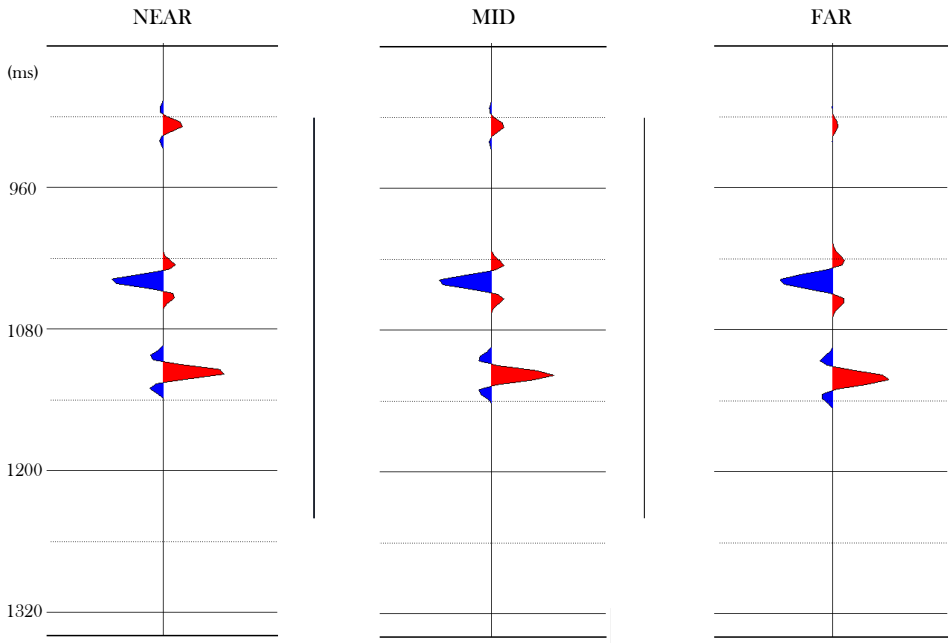

	Vp (km/s)	ρ(g/cm^3)
Caprock	1.86	2.05
Res Top	2.03	2.01
Res Mid	2.03	2.01
Res Base	**1.75**	**1.96**
Below	2.06	2.05

Figure 5.7.1: An NMO-corrected CSP-gather for the first event of the fourth scenario, attached with P-wave velocities and densities for the respective layers. The changed properties within the reservoir are highlighted in black.

As with the previous scenario, increasing the gas saturation and pore pressure in the lowermost sand package yields strong reflections with large amplitudes for all offsets. The bottom reflector slightly decreases with offset, while the reflection above slightly increases. The top reflector is weakened compared to the basis scenario. This is mainly due to the very strong reflections below. However, the amplitude for the top reflector decreases from near to far stack similar to the top reflector in the basis scenario. A minor time-shift also occurs for the bottom reflection compared to the basis scenario (Figure 5.5.2).

The second event assumes that both the mid and lowermost sand packages are saturated with gas, as the CO_2 has migrated through the first semi-permeable layer of shale within the reservoir. The gas saturation in the lowermost layer has increased to 60% with a corresponding pore pressure of 14 MPa while the mid layer has increased to 20% with a corresponding pore pressure of 11 MPa. The uppermost layer is still assumed to be brine saturated and unaffected by the CO_2 injection below. The resulting seismogram can be observed in Figure 5.7.2.

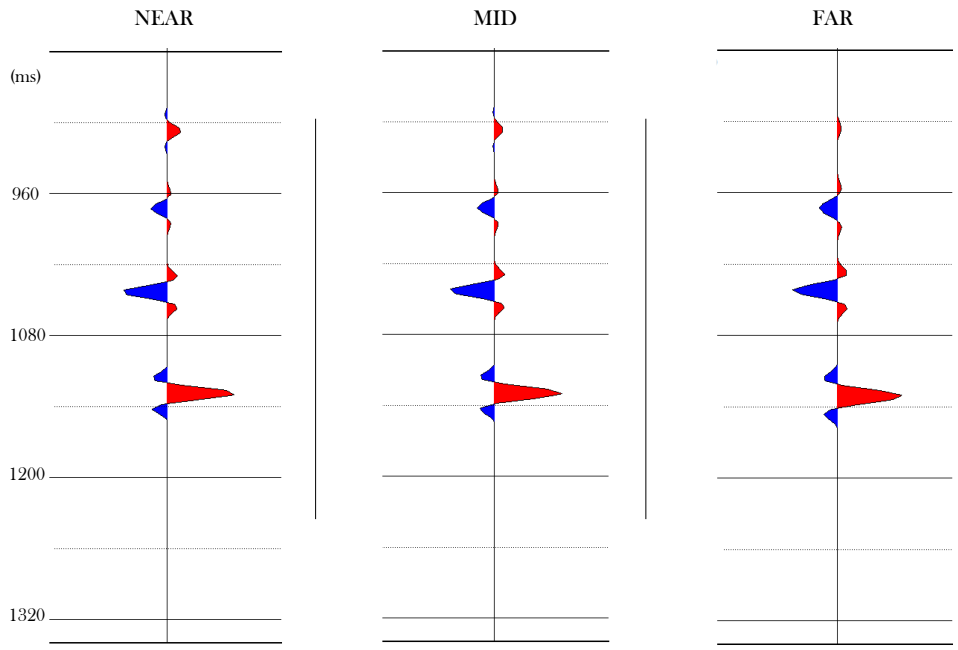

	Vp (km/s)	ρ(g/cm^3)
Caprock	1.86	2.05
Res Top	2.03	2.01
Res Mid	**1.91**	**1.98**
Res Base	**1.58**	**1.94**
Below	2.06	2.05

Figure 5.7.2: An NMO-corrected CSP-gather for the second event of the fourth scenario, attached with P-wave velocities and densities for the respective layers. The changed properties within the reservoir are highlighted in black.

As all layers in the reservoir model have different physical properties, the resulting seismogram contains four reflections. The top reflector is slightly weakened compared to the previous event, though it still has the same trend of a decreasing amplitude with offset. A strong negative reflector occurs beneath the top reflector and is caused by the influence of CO_2 in the second sand package in the reservoir. This reflector contains amplitudes that

slightly increase with offset. However, in comparison to the reflector below, the amplitudes are weaker. This suggests that increasing the gas saturation and pore pressure enhances the seismic response. The lowermost reflection still remains positively strong for all offsets, due to the large contrast between the gas saturated sandstone layer and the brine saturated sandy shale layer beneath.

The final event imagines a setting where all layers in the reservoir are saturated with CO_2, and that each layer has increased pore pressures. The gas saturation in the lowermost layer is set to 90% with a corresponding pore pressure of 15 MPa. The middle layer has a gas saturation of 60% with a corresponding pore pressure of 12 MPa, and the uppermost layer has a gas saturation of 20% with a corresponding pore pressure of 11 MPa. The resulting seismogram can be observed in Figure 5.7.3.

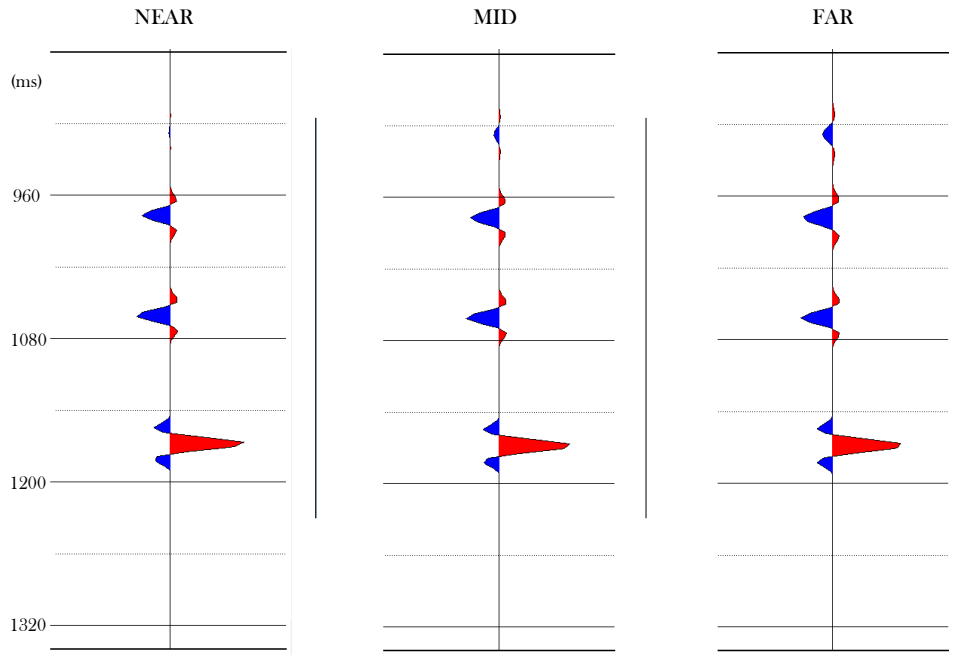

	Vp (km/s)	ρ(g/cm^3)
Caprock	1.86	2.05
Res Top	**1.91**	**1.98**
Res Mid	**1.61**	**1.92**
Res Base	**1.26**	**1.92**
Below	2.06	2.05

Figure 5.7.3: An NMO-corrected CSP-gather for the third event of the fourth scenario, attached with P-wave velocities and densities for the respective layers. The changed properties within the reservoir are highlighted in black.

The top reflector changes polarity as the uppermost layer in the reservoir is saturated with carbon dioxide. The amplitude increases with offset. As for the previous events, higher gas saturations and pore pressures yield stronger reflections and amplitudes. However, the reflection below the top reflector is slightly increased while the reflector above the lowermost reflection is slightly reduced compared to the previous event. This is due to the relative differences in acoustic impedance between the separate layers, and is based on the fact that a minor gas saturation change has a greater effect on amplitudes than a higher gas saturation change. The lowermost reflection still remains positively strong for all offsets and decreases slightly from near- to far stack, though a time-shift of approximately 60ms has occurred compared to the previous event. The lowermost reflection is also stronger than the same reflector for the basis scenario.

5.8 Summary

The AVO-crossplot (Figure 5.4.1) and numerical examples (Figures 5.5.2 – 5.7.3) have demonstrated that the seismic reflections and amplitudes are directly linked to lithological variations, pressure -and saturation changes, and fluid distribution patterns. This proves the importance of preserving pre-stack data when acquiring and processing seismic.

By increasing the shale content in a sandy reservoir, the shale particles clog pore throats and reduce porosity, thereby stiffening the reservoir rock. The same applies to a cementation process, as small fractions of cement slightly reduces the porosity but rapidly stiffen the rock frame. This lowers the overall contrast between layers in the geological model and attenuate seismic reflections and amplitudes compared to a scenario without shale or cement. In case the surroundings are softer originally, the cement and shaliness have the opposite effect and slightly increases the reflection as observed for the top reflector in scenario 2. Additionally, it is important to keep in mind that increasing the shale content only stiffens the rock to a certain point, as a shale fraction exceeding the sand fraction in a reservoir would have the opposite effect (Avseth et al., 2005).
Moreover, by increasing the pore pressure and gas saturation within a reservoir as a result of carbon dioxide injections, the reflections become brighter and the amplitudes increase as the properties of the reservoir are weakened. For the reflectors above the CO_2 saturated layers, the polarity is also reversed, and increases with offset similarly to the trends in the AVO crossplot.

6 Case study: The Sleipner Field

6.1 Background and CO_2 history

The Sleipner Field is located in the northern part of the North Sea and consists of two separate producing fields: Sleipner West and East. Sleipner West and East were discovered in 1974 and 1981, and started production of gas and gas condensate in 1996 and 1993 respectively. NPD's division map for the Norwegian Continental Shelf shows that the field is situated within block 15/9 and 15/6 as shown on Figure 6.1.1 (NPD, 2021b).

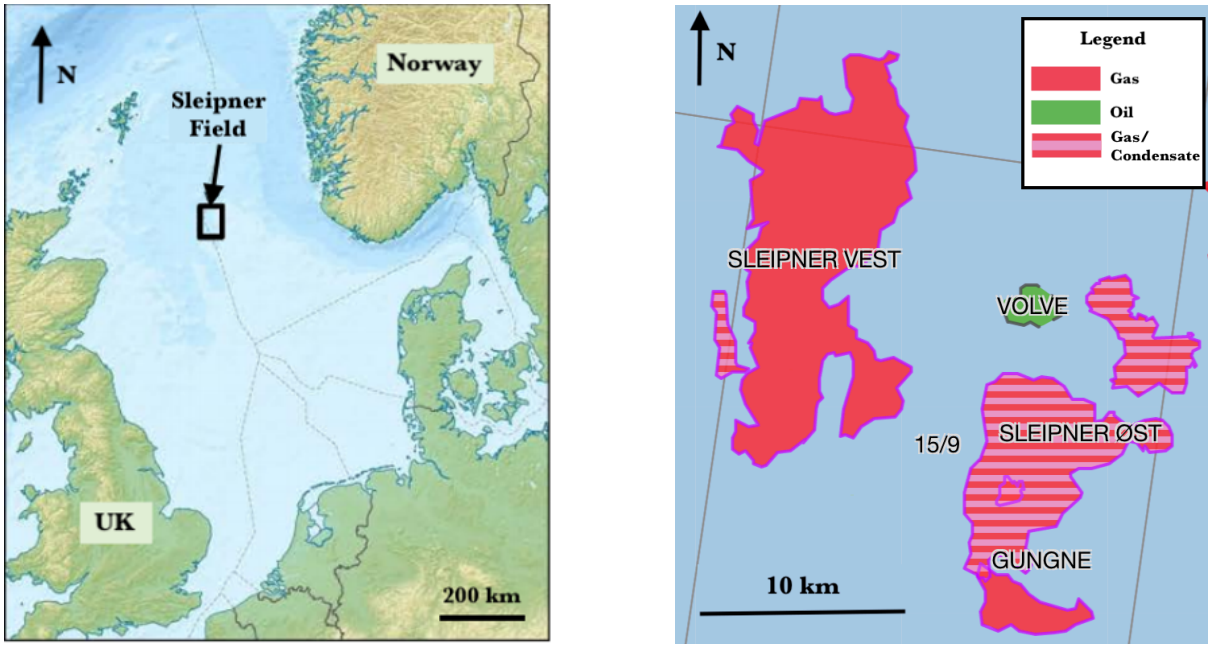

Figure 6.1.1: Location of the Sleipner Field in the North Sea. Modified from Furre et al. (2016) and NPD (2021b).

Due to the high concentration of carbon dioxide in the produced gas from Sleipner, the composition did not meet sales requirements and had to be processed via amine scrubbers that removed the excessive CO_2. While the operators simultaneously tried to avoid supplemental pollution to the atmosphere and reduce the Norwegian tax for carbon emissions, it was determined that the excessive carbon dioxide would be captured and stored in the subsurface (Furre et al., 2016; Chadwick and Eiken, 2013).

The sequestration process has been ongoing since 1996, with an annual injection rate of 1Mt CO_2. By injecting carbon dioxide into the subsurface, the Sleipner CO_2 injection project has become the world's first industrial offshore CCS project. It therefore acts as a pilot for similar carbon sequestration projects globally (Furre et al., 2016; Chadwick and Eiken, 2013).
The injection activities at Sleipner are also accompanied by multinational research projects, CO2STORE and SACS, which aim to monitor the behaviour of CO_2 in subsurface formations in long term perspectives. This is done by testing and refining monitoring tools and improving the understanding of CO_2 migration and trapping mechanisms within storage reservoirs.
As a result, the research projects contribute to the promotion and development of CCS technology from a small research and demonstration scale to large-scale industrial implementation, by providing robust guidelines for effective and safe storage of CO_2 for a range of geological settings, both onshore and offshore (Chadwick et al., 2008; Zweigel et al., 2004).
The key monitoring techniques that have ensured storage integrity and tracked storage performance at Sleipner, have primarily been based on time-lapse seismic, gravimetry and controlled source electromagnetics (Chadwick and Eiken, 2013). This thesis only covers the aspect of time-lapse seismic.

6.2 Geological setting

6.2.1 Utsira reservoir

The Utsira formation is the reservoir unit for the carbon sequestration at Sleipner (Figure 6.2.1). Utsira is characterized as a very permeable, porous and thick saline aquifer, and consists of clean, fine-grained and friable sand (Arts et al 2008; Chadwick et al., 2005). The sand consists primarily of quartz with some feldspar and shell fragments. The exact mineral composition is provided in Chadwick et al. (2004). Biostratigraphical analysis has determined that the Utsira originates from late middle Miocene (c. 11Ma) to earliest late Pliocene (c. 3Ma) (Zweigel et al., 2004).

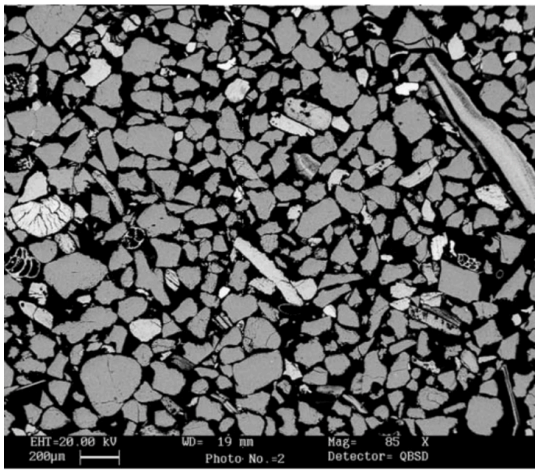

Figure 6.2.1: SEM image of the friable Utsira Sand under a transmitted light. Source: Chadwick et al. (2004).

The reservoir is situated within the late Cenozoic post-rift succession of the northern North Sea Basin, forming a basin-restricted lowstand deposit of considerable extent. It stretches 400 km from north to south and between 50 and 100 km east to west (Figure 6.2.2). The Utsira formation is constrained by stratigraphical onlap to the east and west, finer grained sediment to the southwest, and a narrow, deepening channel to the north (Chadwick and Eiken, 2013; Chadwick et al., 2004).

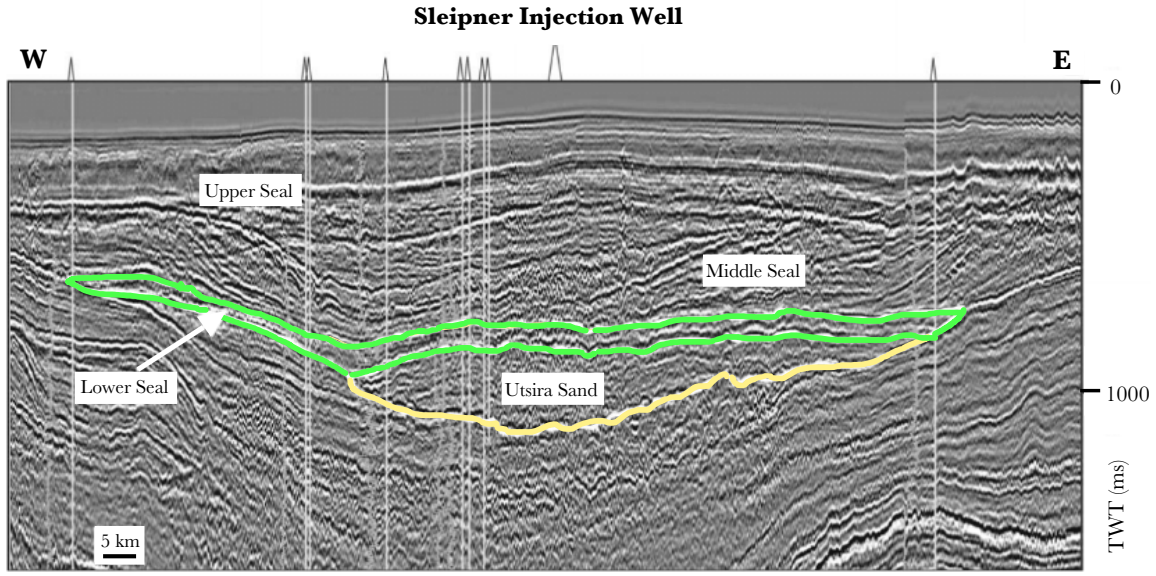

Figure 6.2.2: A seismic cross section of the Utsira Sand (yellow) overlain by the Nordland caprock (green). The cross section is oriented from west to east, with the two-way traveltime presented to the right. Modified from Hermanrud et al. (2009).

Internally the Utsira Sand is composed of stacked overlapping mounds of very low relief, interpreted as individual fan lobes. According to Gregersen et al. (1997), the Utsira Sand was deposited as turbidites in a moderately deep marine environment.
The fan lobes are commonly 30 m thick and are separated by very thin intra-layering shale beds that can be observed on the calibrated Vshale log in Figure 5.2.1. The intra-reservoir shale layers are usually 1 m thick and act as important permeability barriers towards the upward migration of CO_2 in the reservoir. The intra-layering shales have had a significant effect on CO_2 migration through, and entrapment within, the reservoir (Arts et al., 2008; Chadwick and Eiken, 2013; Chadwick et al., 2005).
According to Zweigel et al. (2000) the intra-layering shales contain fractures and are therefore slightly permeable due to differential subsidence and erosion during the deposition of the individual sand lobes. This suggests that accumulations of CO_2 would eventually migrate through the intra-layering shales. Furthermore, a laterally persistent and much thicker shale layer separates an eastward thickening sand wedge from the main reservoir below, and is detectable on both the calibrated well log (Figure 5.2.1) and 3D seismic in the vicinity of Sleipner (Zweigel et al. 2000; Chadwick and Eiken, 2013).

Isopach maps of the reservoir reveal two distinctive depocenters. The first depocenter is situated in the southern part of the Utsira Sand near Sleipner, while the second is situated further north, approximately 200 km apart with thicknesses exceeding 300 m and approaching 200 m respectively (Chadwick and Eiken, 2013; Kirby et al., 2001).
The depth to the top Utsira generally varies smoothly from 500 – 1500 m, and is around 800-900 m near Sleipner (Kirby et al., 2001). The top Utsira surface is characterized by irregular topography and several linked domal and anticlinal structures caused by subsidence anomalies. These anomalies are predominantly influenced by mud mobilisation edifices at the base of the Utsira Sand. The top Utsira also has a weak regional dip towards the south. (Zweigel et al., 2000). Isopach and depth to the top Utsira maps are shown in Figure 6.2.3.

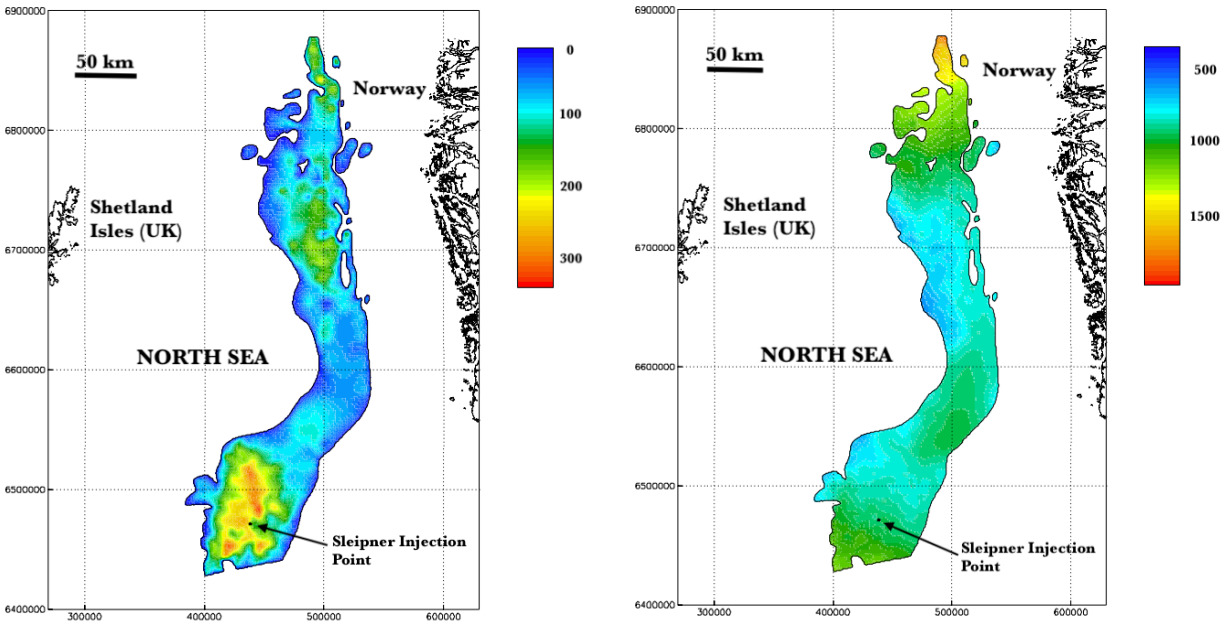

Figure 6.2.3: Isopach (left) and depth to top Utsira (right) maps for the Utsira Sand. The colour bars to the right indicate thicknesses and depths in metres. Modified from Kirby et al. (2001).

The base of the Utsira Sand is structurally more complex, and is characterised by mud diapirism. The base consists of numerous mounds of mud diapirs. The diapirs are usually 100 m high and are mapped either as isolated and circular domes, or irregular and elongated bodies with varying orientations. Additionally, they are typically 1 - 2 km in diameter and up to 10 km in length. The diapirism is associated with soft sediment mobilisation and local reverse faulting in the shaly Hordaland formation below, cutting the base of the Utsira Sand. However, it does not appear to affect the upper parts of the reservoir or its caprock, thus the storage integrity (Chadwick et al., 2004).

6.2.2 Nordland caprock

The caprock succession overlying the Utsira reservoir is several hundred metres thick and can be categorized into three main units: The Lower, Middle, and Upper Seal. The Lower Seal, acting as the immediate reservoir caprock, consists of clay-rich sediments of the Nordland Group and is commonly referred to as the ‘Shale Drape’ (Chadwick et al., 2004).
The Middle Seal consists of distal parts of sediment wedges that prograded from the western and eastern basin margins during the Pliocene. It is dominantly muddy in the basin centre and coarsens into sandier facies both upwards and towards the basin margins. The Upper Seal is

of Quaternary age, composed primarily of glacio-marine clays and glacial tills (Chadwick et al., 2004).

Chadwick et al. (2004) state that the lowermost caprock is basin-restricted with a thickness ranging from 50 - 100 m. Core and cuttings samples have revealed that the Lower Seal is composed of grey clay silts or silty clays, identified as non-organic mudshales and mudstones. These are uncemented and plastic with a very low permeability. The specific mineral composition is provided in Chadwick et al. (2004).
Even though the porosity is unusually high for the Nordland caprock, up to 35% , the low permeability and pore throat diameter of 14 - 40 nm ensures a capillary entry pressure of between 2 and 5.5 MPa, capable of trapping a supercritical CO_2 column several hundred metres high. As a result, the caprock acts as an effective seal as the buoyancy pressure is significantly lower than the sealing capacity. Additionally, the maximum confined column heights of CO_2 are generally below 10 metres in the Utsira reservoir. This implies that a capillary leakage of CO_2 is very unlikely to occur (Arts et al., 2008; Chadwick et al., 2004). Additionally, it was estimated that the caprock extends more than 50 km west and 40 km east of the area occupied by the injected CO_2 in 2001, and that this is well beyond the predicted final migration footprint of the CO_2 plume at Sleipner (Zweigel et al., 2000; Chadwick and Eiken, 2013).

6.2.3 Injection profile

Carbon dioxide is being injected into the lowermost sand lobe in the Utsira reservoir via a deviated well at 1012 m depth, about 2.3 km from the Sleipner platform (Figure 6.2.4). Simulation models have predicted that the carbon dioxide will migrate primarily to the north-west if the top Utsira acts as a long term barrier, and to the north-east if gas invades the sand wedge above the main reservoir (Zweigel et al., 2000; Zweigel et al., 2004). Exact migration paths depend largely on net to gross, porosity and topography of the overlaying shale layers. (Chadwick and Eiken, 2013; Zweigel et al., 2000)

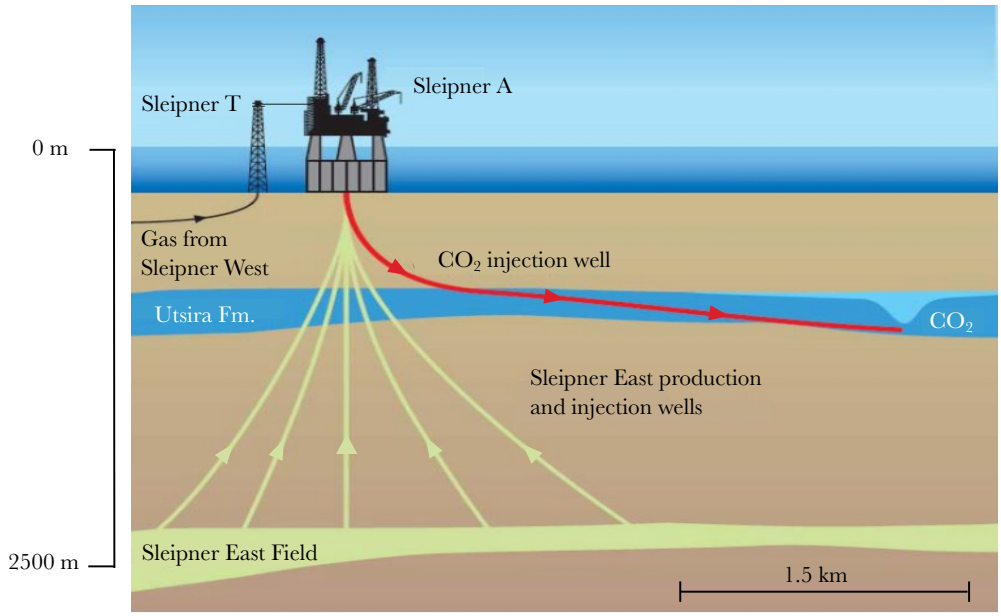

Figure 6.2.4 : The Sleipner East Field with both injection (red) and production (green) wells presented. The separation of CO_2 takes place at Sleipner T. Modified from Kalam et al. (2020).

The geological setting at Utsira is therefore ideal for carbon sequestration, considering the fact that thick and highly porous sand lobes are overlain by both intra-layering shales in the reservoir zone acting as semi-permeable barriers toward the upward migration of CO_2, and a thick succession of an impermeable and ductile caprock. Thus, creating several individual layers of gas sand within the reservoir. The injection profile is illustrated in Figure 6.2.5, with specific permeabilities and porosities listed below in Table 6.2.1, as presented in Chadwick and Eiken (2013). Since the horizontal permeability is lower than the vertical permeability, the CO_2 plume will presumably stretch out laterally more easily than vertically.

Table 6.2.1: Porosity and permeability of the caprock and reservoir.

Layer	**Porosity (%)**	**Permeability (Darcy)**
Caprock	32 - 38	$4 \cdot 10^{-7}$ $(vertical)$ $1 \cdot 10^{-6}$ $(horizontal)$
Reservoir	30 – 42	1 – 3

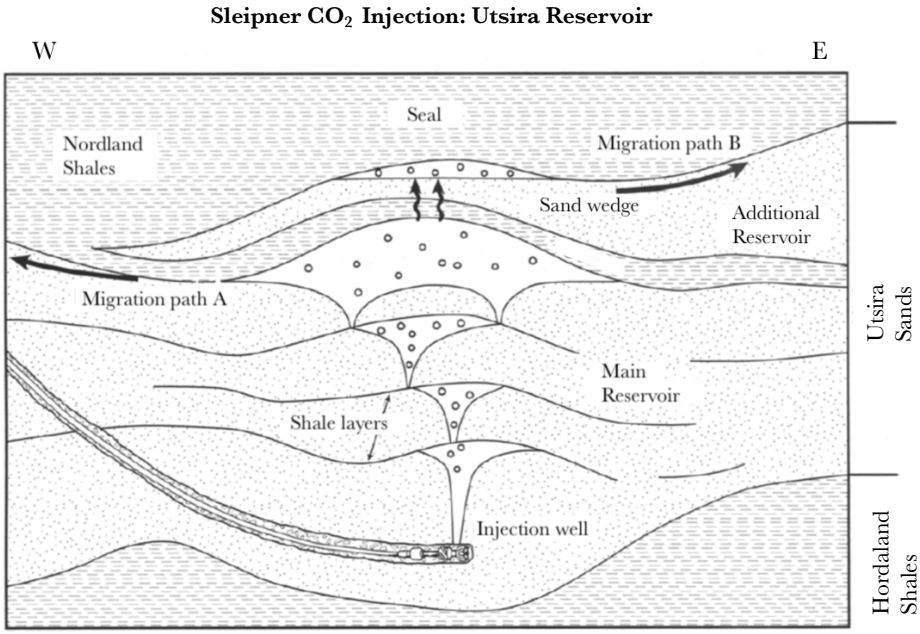

Figure 6.2.5: An illustration of the injection profile at Sleipner from west to east. Modified from Zweigel et al. (2004).

6.3 Data and modelling

6.3.1 Time-lapse seismic monitoring

Several 3D seismic surveys have been carried out since the start of the CO_2 injection project at Sleipner. The seismic surveys acquired in 1994 and 2006 are presented in this thesis, as these represent time-lapse seismic from a pre-injection phase to a mature injection phase respectively. A full stacked seismic section from 2001 is also included in Figure 6.3.3, in addition to the ’94 and ’06 sections, primarily to monitor the development of an increasing CO_2 plume using time-lapse seismic. According to Chadwick and Eiken (2013), a total of 8.5 Mt of CO_2 was stored in the Utsira Sand in 2006. The polarity for the seismic from Sleipner is however reversed compared to the numerical examples (Figure 6.3.1). According to Shadlow (2014), the polarity of the seismic represents a major pitfall regarding the correct interpretation of a DHI, as hard events could be interpreted as gas sands, and vice versa.

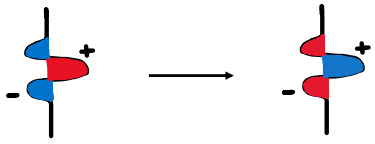

Figure 6.3.1: The observed polarity reversal for the seismic responses between the numerical examples (left) and the acquired seismic from Sleipner (right).

The positioning of the extracted seismic cross section can be viewed in Figure 6.3.2.

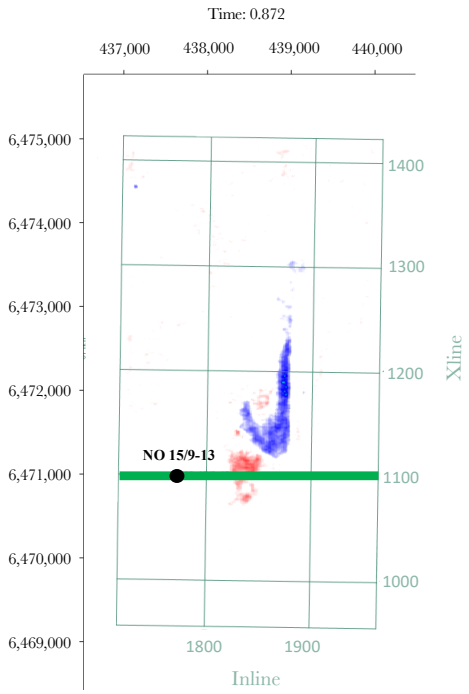

Figure 6.3.2: A time-slice of the full stack difference between the ’94 and ’06 surveys for the top reflector at Utsira. The geographical positioning are presented on the y- and x-axis. The green rectangle represent the 3D seismic cube with corresponding inlines and xlines. The selected seismic cross section (Xline = 1099) is highlighted in green and cuts through well 15/9-13 (black dot).

The seismic sections in Figure 6.3.3 show the time-lapse effect of injecting CO_2 into the Utsira reservoir. Several of the reflectors in the ’01 and ’06 sections have been strengthened and appear much brighter compared to the same reflections in the baseline survey from 1994. Assuming that the geological setting have remained the same throughout the time period and that the survey geometry is more or less equal, the observed differences are directly linked to the CO_2 injections. By studying the lateral extent of the bright amplitude anomalies, the gas has also disseminated more widely in the ’06 section than the ’01 section. The amplitudes also appear slightly stronger on the ’06 section as a result of larger CO_2 accumulations within each layer, which is in correspondence with the statement of Arts et al. (2004) that amplitude strength increases proportionally with CO_2 layer thicknesses up to 8 m (= tuning thickness) in the Utsira reservoir. Figure 6.3.4 shows the influence of CO_2 on physical rock properties, thus the acoustic impedance contrast and seismic response. The properties in Figure 6.3.4 are calculated based on the calibrated RPM for the Utsira reservoir, with a temperature of 41°C and a pressure of 10MPa (Table 5.2.1).

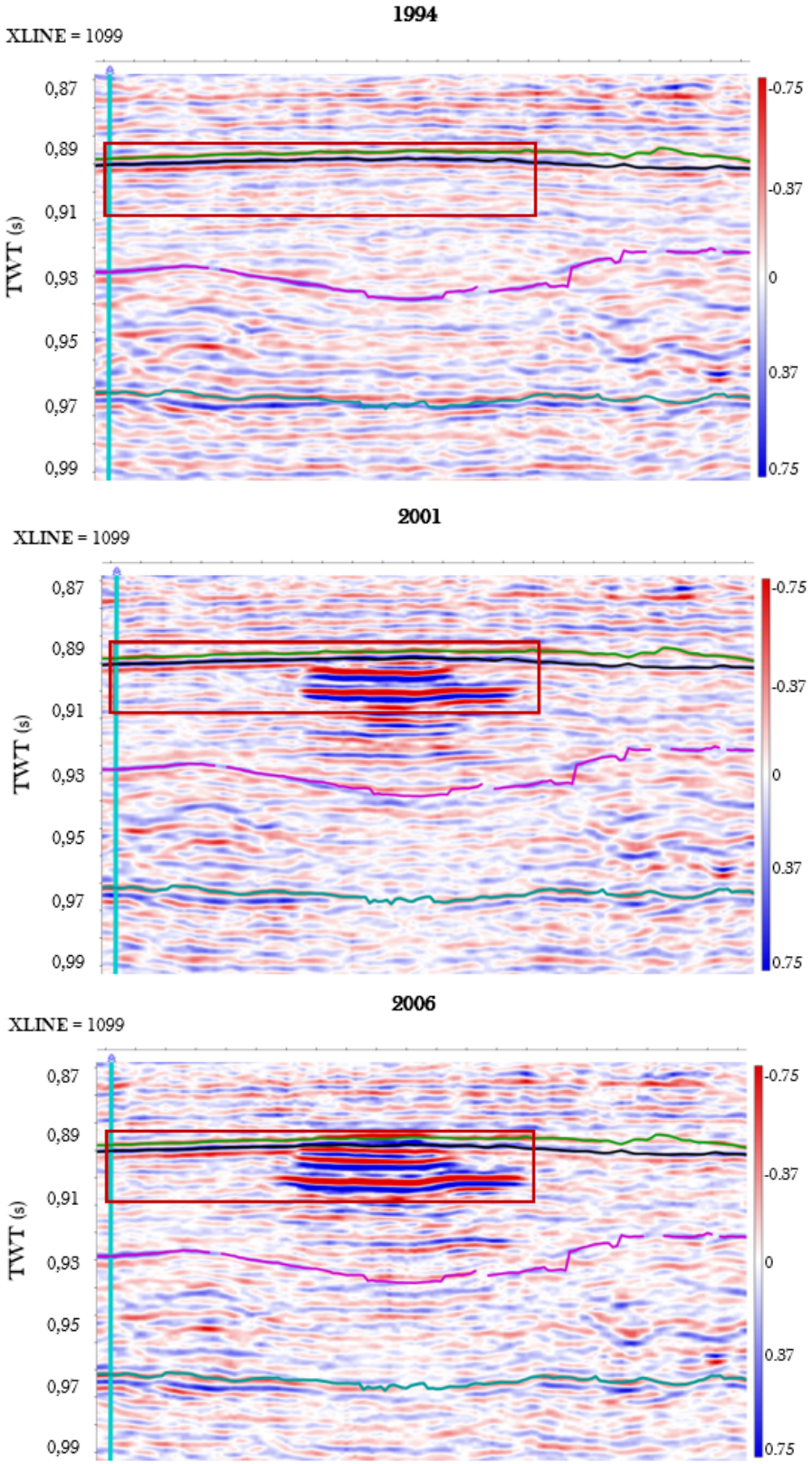

Figure 6.3.3: Full stack seismic sections of the ’94, ’01, and ’06 surveys. The amplitudes are scaled from -0.75 to 0.75. Well 15/9-13 is plotted to the left (light blue). The horizons include the Utsira Sand wedge (green), top Utsira (yellow), base Utsira (pink), and the time-shift marker (light green). The red rectangle represent the area of interest for AVO analysis. Two-way traveltime is presented on the y-axis.

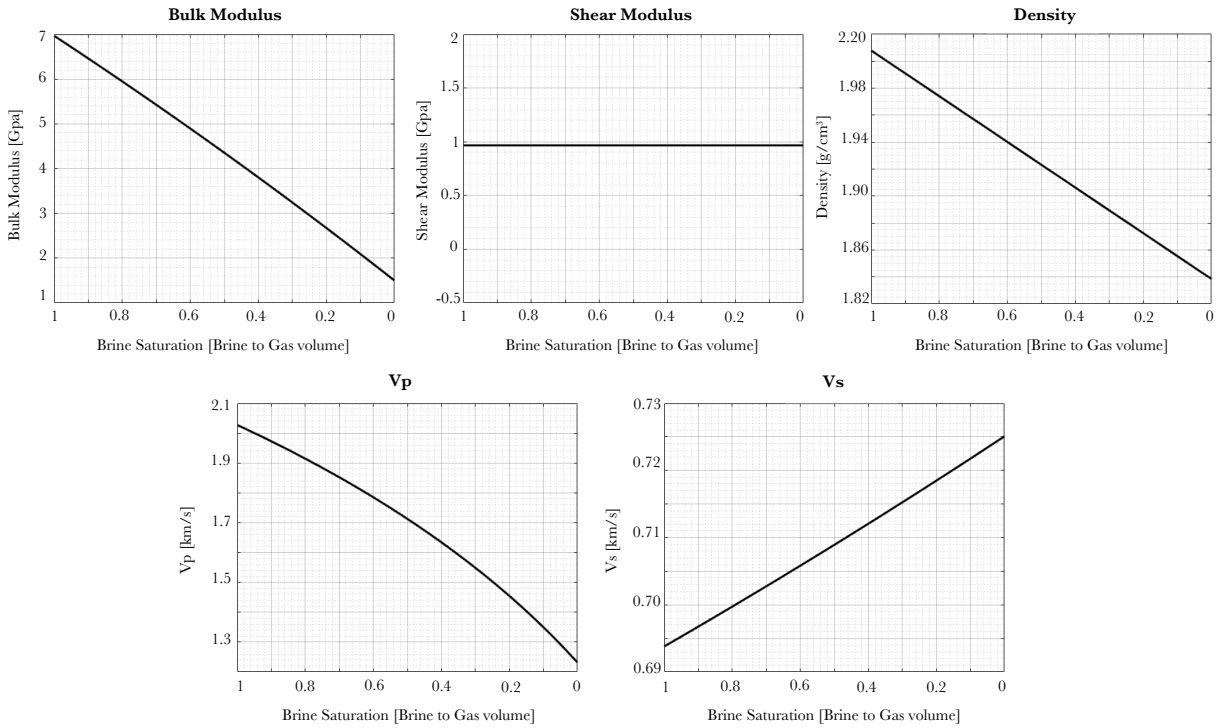

Figure 6.3.4: The effect of CO_2 on bulk modulus (top left), shear modulus (top middle), density (top right), P-wave velocity (down left) and S-wave velocity (down right). The physical properties and acoustic velocities are plotted as a function of brine saturation in a mixture with CO_2. The x-axis is reversed, so that the gas saturation increases to the right.

Figure 6.3.4 shows that increasing the gas saturation will lower the bulk modulus and density considerably, while the shear modulus remains unaffected. As a consequence, the V_p is reduced significantly while the V_s is slightly increased due to the density decrease. Hence, the elastic impedance contrast between the sands and shales is enhanced. A larger acoustic impedance contrast generates brighter reflections, and explains the full stack amplitude anomalies occurring between the seismic profiles in Figure 6.3.3. The observations are in correspondence with information presented in Arts et al. (2004), stating that two dominant effects determine the seismic response at Utsira: an enhanced negative elastic impedance contrast due to the presence of CO_2 in the sand layers, and the interference from sequences of water saturated sand, shale, CO_2 – saturated sand, and water saturated sand again. Since the impedance contrasts between shale and underlaying sand increase significantly from ’94 to ’06 due to the presence of CO_2, the anomalies can be identified as seismic bright spots (Figure 4.2.3). The next subchapter will study the AVO effects of injecting CO_2 on near and far stacks from Sleipner, and correlate the observed amplitude changes to the synthetics and AVO trends from the previous chapter.

6.3.2 AVO effects

In order to study AVO effects, the full stack seismic sections from ’94 and ‘06 are split into near- and far stack seismic sections. According to Chadwick et al. (2010), the near stack represents incidence angles between 6° and 16°, while the far stack composes of incidence angles between 28° and 38°. The sections represent AVO data within the red rectangle in Figure 6.3.1. This area is further divided into three units that will be studied individually. The separate units are presented as A, B and C. The near and far stacks for the seismic sections are shown in Figure 6.3.5.

The presence of hydrocarbons in a reservoir influences the ratio of compressional and shear wave velocity (Figure 6.3.4), translating to changes in reflectivity with offset on seismic gathers. Hence, as CO_2 is injected into the Utsira reservoir, the acoustic impedance contrast between the layers above and below the reservoir unit is expected to be enhanced with a reflectivity that changes with offset due to V_p/V_s variations. Since Utsira represents a shallow, unconsolidated and saline aquifer, the amplitude anomalies on time-lapse seismic are anticipated to correspond to class III or 4 of the AVO anomalies in Figure 4.2.2 (Shadlow, J., 2014).

By studying unit A for the ’94 section, the amplitudes weaken with offset. Minor variations in amplitude strength occurs for the near stack, especially at top Utsira, and can be interpreted as local porosity variations and/or lithological impurities similar to scenario 2a in the previous chapter. The enhanced amplitudes indicate that the porosity or fraction of sand are slightly increased compared to the surroundings. Nonetheless, the amplitude strength alternates between slightly positive and negative reflections within each stack, indicating that the individual layers of sand and intra-layering shales have more or less the same physical properties. Furthermore, the Utsira Sand wedge horizon indicates that the sand layers are represented as troughs, thus implying that the shale beds are stiffer than the sand beds. Similar observations can be made by comparing unit A for both the 94’ and ’06 sections. Hence, no amplitude anomalies have occurred within unit A between the ’94 an ’06 sections. This indicates that this zone has not yet been influenced by the CO_2 injections, and is still brine saturated.

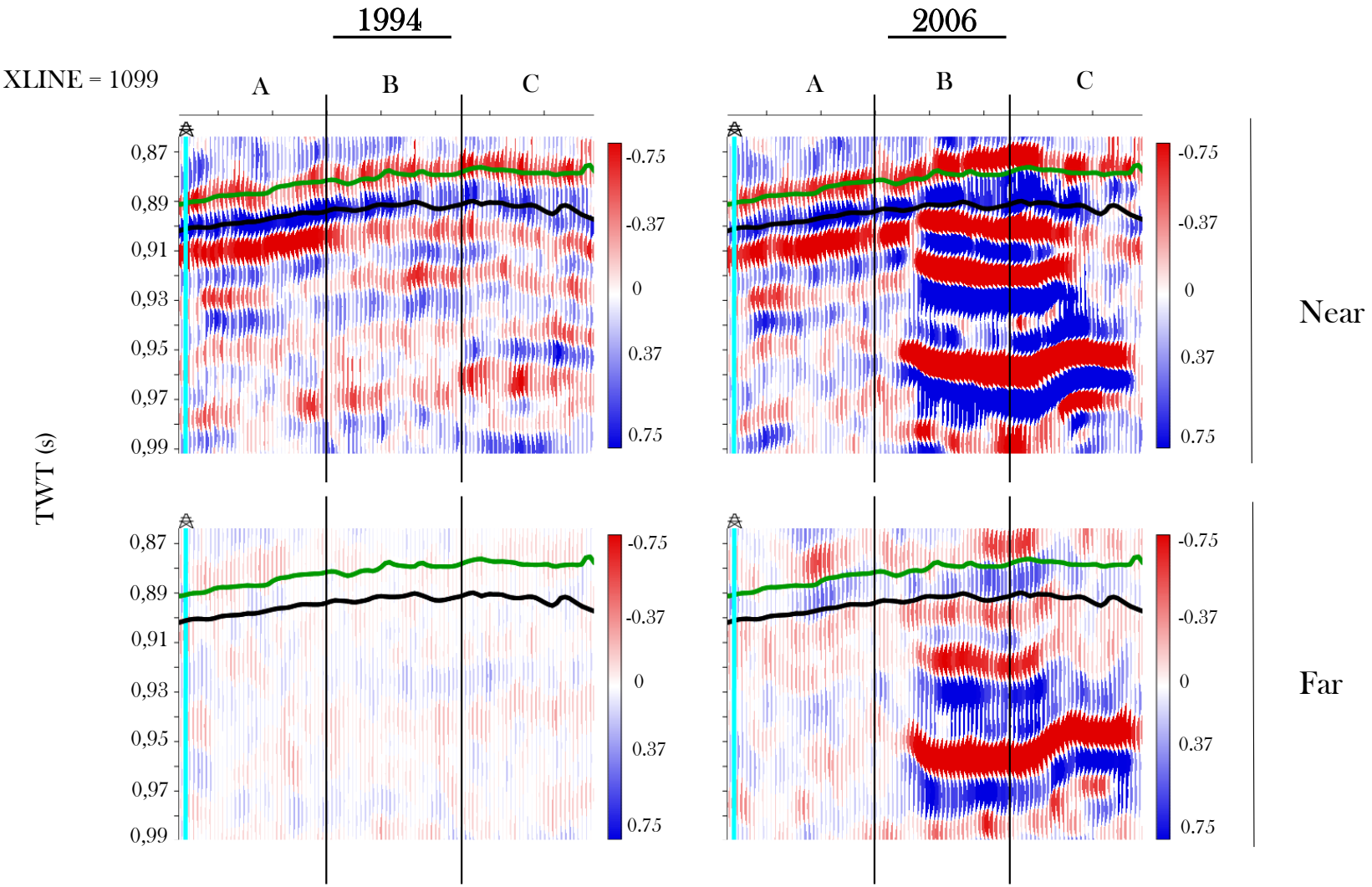

Figure 6.3.5: Near- and far stacks of the ’94 and ’06 seismic surveys. The sections are split into three subunits: A, B, C. The two-way traveltime is represented to the left, with seismic amplitude strength to the right.. The horizons for the top Utsira (black) and Utsira Sand wedge (green) are included, in addition to well 15/9-13 (light blue).

Unit B for the ’94 section has the same trend as unit A and appears more or less the same. However, the top Utsira reflector is slightly weakened in the near stack, possibly due to a local porosity decrease or shale fraction increase, weakening the elastic impedance contrast. Large amplitude anomalies occur when comparing unit B for the ’94 section with the same unit for the ’06 section. The amplitudes are enhanced and the reflections appear much brighter in the ’06 section. A total of four strong events are identified within unit B on the near stack for the ’06 section, however the two uppermost anomalies are weakened in the far stack due to the amplitude decrease with offset. These four events can be interpreted as four individual layers of gas sand separated by overlaying shales. Furthermore, the amplitude anomalies appear stronger for each event downwards, resembling the trend of the numerical examples for fluid distribution patterns (Figure 5.7.3). Therefore, it is possible to assume that both the pore pressure and gas saturation increase within each layer of gas sand downwards. Since CO_2 is injected at the bottom of the Utsira reservoir, and since the interlayering shales act as permeability barriers toward the upward migration of CO_2, higher pore pressures and gas saturations for the lowermost sand lobes seem logical.

The amplitudes in unit C for the ’94 section show similarity to both unit A and B. In terms of the ’06 section, the amplitude anomalies observed in unit B continue into unit C. However, the lateral extent of the amplitude anomalies within unit C varies and increases downwards. This gives an indication that the carbon dioxide has disseminated more widely for the lowermost sand lobe compared to the layers above. Because the horizontal permeability is larger than the vertical permeability and the lowermost sand package contains higher accumulations of carbon dioxide, the lateral extent of the amplitude anomalies within each layer is reasonable. This observation is also in compliance with Arts et al. (2004), which state that the marked decrease of seismic amplitudes at the edges of the anomalies indicate very thin layers of CO_2 pinching out to zero thicknesses.

To provide more certainty to the interpretations of AVO effects, an AVO RPT can be created. This rock physics template was introduced by Jensen et al. (2016b), and relates near stack to far stack responses for seismic amplitudes. Furthermore, trend lines representative to the calibrated rock physics model are plotted to correlate amplitudes to porosity, lithology and fluid saturation. Amplitudes were picked within areas of the bright spot anomalies and in the vicinity of well 15/9-13. The resulting AVO RPT is shown in Figure 6.3.6, with input presented in Appendix B.

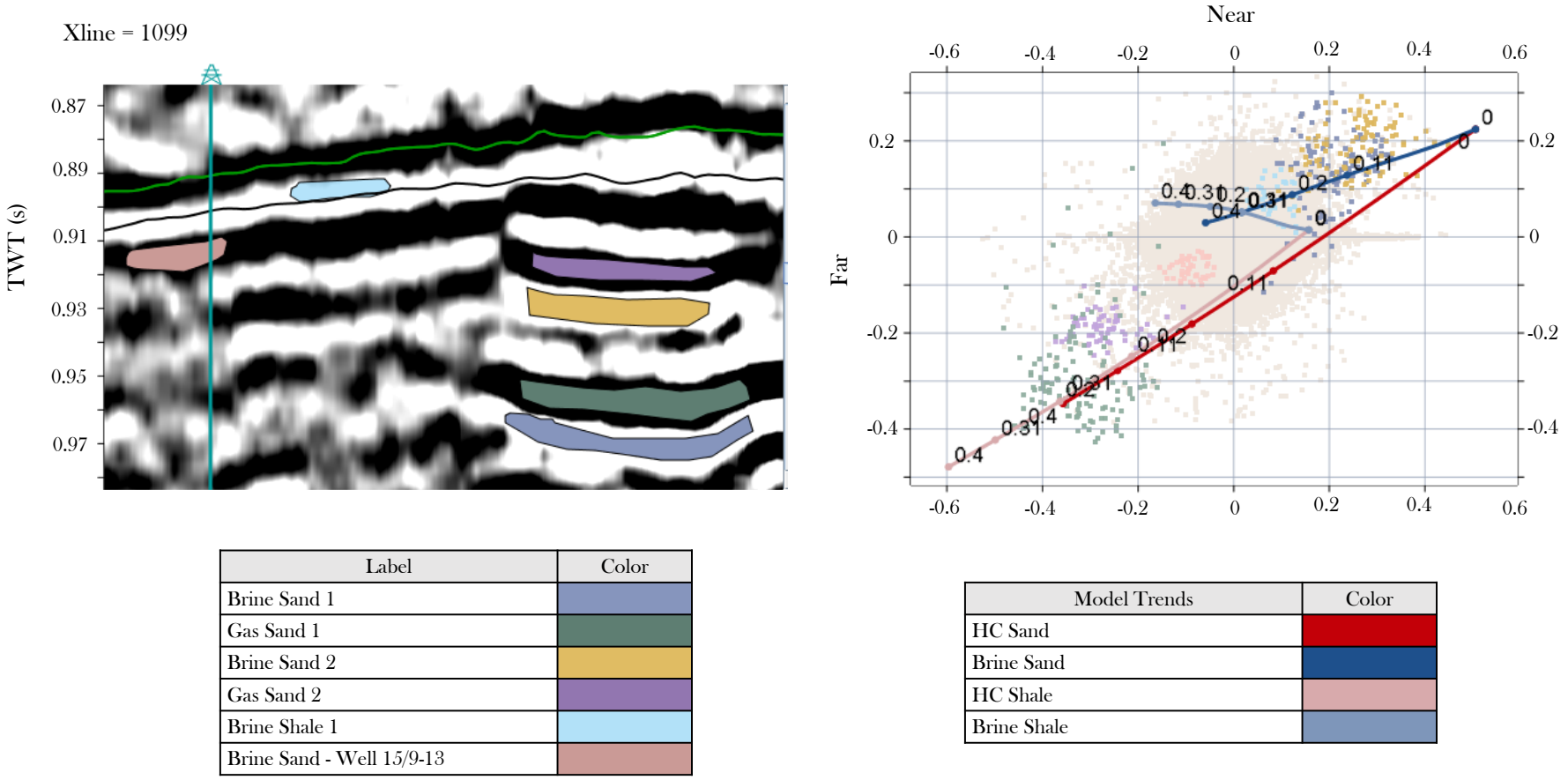

Figure 6.3.6: An AVO RPT (right) relating near to far stack responses for picked amplitudes within areas of the Utsira reservoir (left). The values represent amplitude strength (≥ |1|). The picked amplitude layers are colour-coded to the left, and are marked with the same colours in the AVO RPT plot. The trendlines for brine- and hydrocarbon saturated sandstone and shale are also distinguished with colours to the right, and plotted as a function of porosity (scaled from 0 to 1).

The AVO RPT has been used to calibrate scaling factors for near and far stacks to make the amplitude responses fit with trends of brine and hydrocarbon saturated shale and sand as a function of porosity. As a result, the negative amplitude anomalies interpreted as gas sands fall directly on the trend line of a highly porous and hydrocarbon saturated sandstone. However, these layers also coincide with the trendline of hydrocarbon saturated shales with intermediate porosities. Similarly, the amplitudes corresponding to the brine sands and shales are plotted towards the trendlines of a brine saturated sandstone and shale with intermediate porosities. The picked amplitude values cutting through well 15/9-13 are plotted somewhat between a highly porous and brine saturated sandstone, and a low porous and hydrocarbon saturated sandstone or shale. This gives an indication that the brine saturated sand layer cutting through well 15/9-13 might contain small fractions of gas.
The AVO RPT is however prone to error. The reliability of the AVO RPT is determined by the accuracy and quality of the calibration of scaling factors and the calibrated rock physics model from which the trend lines are derived. Thereby, to what extent the template is able to distinguish various lithologies, fluid saturation and porosities. By creating a classical RPT for the calibrated RPM this can be investigated further (Figure 6.3.7).

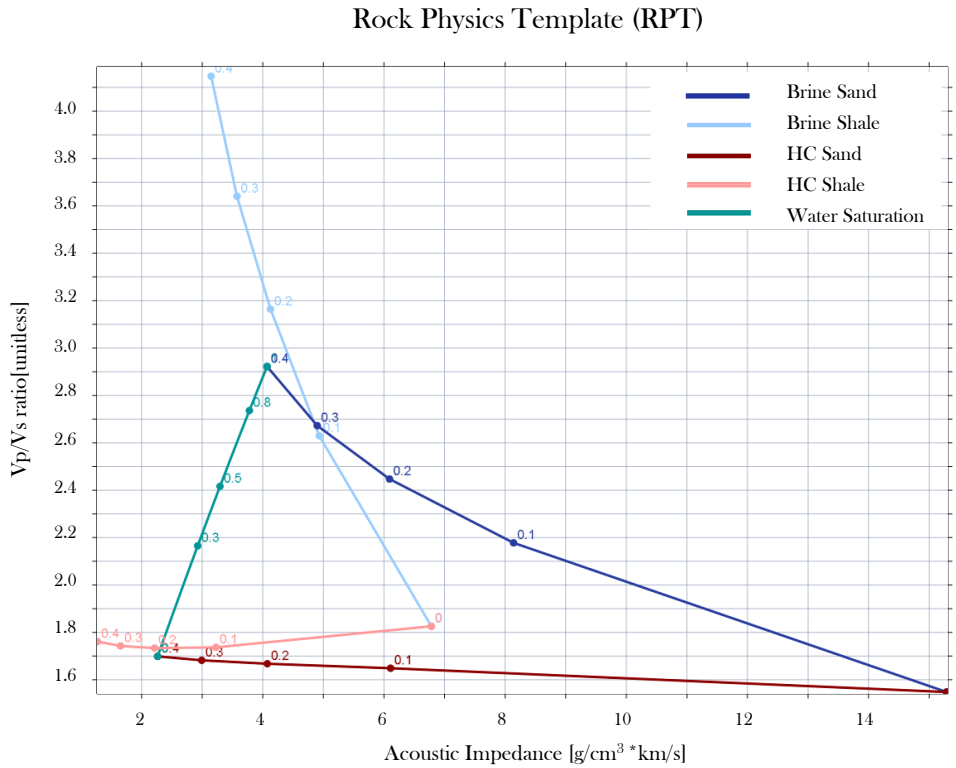

Figure 6.3.7: An RPT for the calibrated Utsira reservoir model. Vp/Vs ratio is plotted as a function of acoustic impedance. The dots plotted along the trendlines represent porosity, scaled from 0 to 1. The trendlines represent hydrocarbon sand (red) and shale (pink), brine saturated sand (blue) and shale (light blue), and water saturation (green).

The classical RPT highlights similar issues, and proves that distinguishing lithologies at the given depth of the Utsira reservoir are difficult, though fluid saturations and porosity are easily distinguished. This observation gives an indication that rock physical modelling for shallow subsurface reservoirs are useful for fluid predictions, but not necessarily for lithological predictions.

Figure 3.5.2 illustrates that shales reduces porosity more easily than sand due to mechanical compaction. Considering the fact that Utsira is a shallow reservoir, this therefore suggests that the softer shales with lower porosities have similar physical properties as the stiffer sands with higher porosity. This can help explain why the RPM has difficulties distinguishing lithologies, as there is a cross-over between the physical properties of shale and sand at the given depth. Furthermore, the enhanced sensitivity to fluid saturation is reasonable considering the loose rock frame and available pore space for fluids to occupy. As a result and despite its limitations, the AVO RPT is a useful tool to aid the interpretation of AVO effects in this case study as the lithology of the Utsira reservoir is known.

Ultimately, by combining both the near stack and far stack for the seismic surveys in ’94 and ’06, a full stacked difference section can be created. A stacked difference plot highlights the AVO anomalies occurring between the pre-injection phase and the mature injection phase respectively (Figure 6.3.8).

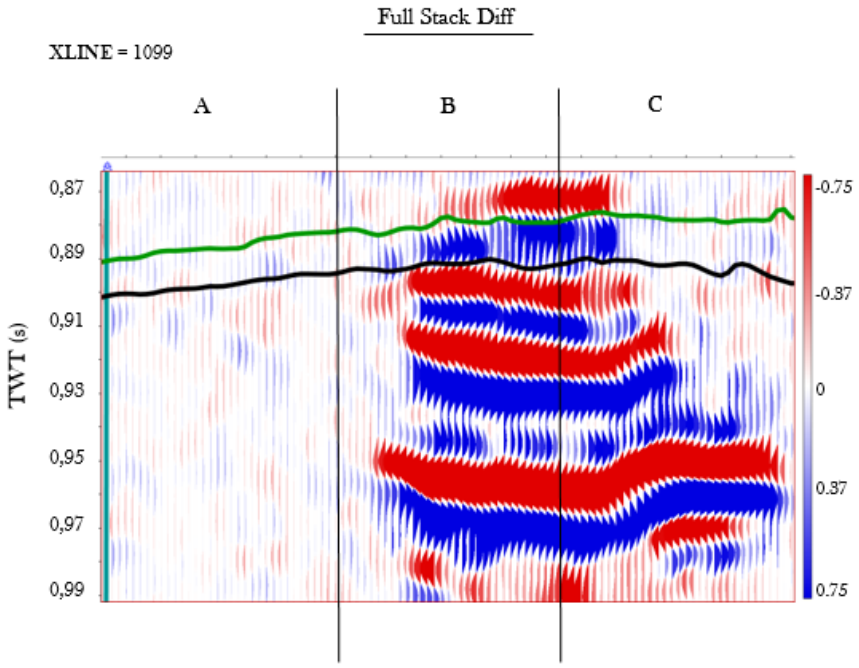

Figure 6.3.8: A full stacked seismic section of the difference between the ’94 and ’06 surveys. The strong reflections represent bright spots, and highlight the time-lapse effect of CO_2 injections on seismic amplitudes.

Considering that the amplitudes have increased significantly with time, and decrease with offset (Figure 6.3.5), the anomalies can be interpreted as bright spots and Class IV AVO anomalies. (Shadlow, 2014). Chadwick et al. (2010) also confirmed that the gas sands at Sleipner correspond to a Class IV AVO anomalies by plotting reflectivity as a function of incidence angle for various CO_2 layer thicknesses. Arts et al. (2004) also state that the pressure effect on amplitudes in the Utsira reservoir is marginal due to the thick and highly porous aquifer. Therefore, the time-lapse responses are exclusively influenced by fluid saturation. This was also observed in the AVO crossplot (Figure 5.4.1), as increased gas saturation yielded the strongest response. As a consequence, discriminating pressure and temperature effects from fluid effects on seismic responses is difficult for this case study due to the large influence of CO_2 saturation.

From a different perspective, the effect of cement can be neglected in this case study, as the reservoir is located at around 1 km depth, with a typical North Sea geothermal gradient of 35°C/km (Chadwick and Eiken, 2013). Neither has it been reported that the reservoir has experienced any subsequent uplift, or been influenced by active tectonics or volcanic intrusions, implying that the cementation process has not yet been initiated for the friable sand (Arts et al., 2008, Chadwick et al., 2004).

Moreover, Arts et al. (2004) state that the resolution of the seismic sections at Sleipner is able to detect local CO_2 accumulations in the order of a metre or less. This provides confidence when studying the reflections above the caprock of the Utsira reservoir, showing no similar amplitude anomalies on time-lapse seismic (Figure 6.3.3). Hence, no evidence of leakage has been observed and Utsira acts therefore as an ideal reservoir for carbon storage at Sleipner.

7 Discussion

This thesis has scrutinized time-lapse seismic monitoring of CO_2 injections at Sleipner by studying AVO effects for a confined area within the seismic surveys acquired in 1994 and 2006. Further, synthetic seismic of hypothetical scenarios have been created to correlate the observed AVO effects to various factors influencing the reflections and amplitudes. Full stack seismic surveys have also been studied to relate the observed amplitude anomalies to DHIs. The main objective has been to establish a correlation between AVO effects and changes in CO_2 saturation, temperature and pressure. The discussion emphasizes on the overall seismic trends caused by various factors including lithology, fluid saturation, porosity, temperature and pressure. Additionally, a discussion of amplitude attenuation and wavelet effect on seismic data is included. Finally, the reliability of the modeling results is briefly discussed.

7.1 CO_2 saturation effect on seismic properties

The modelling results of substituting brine with carbon dioxide using Gassmann were in correspondence with theory (Gelius and Johansen, 2010). Increasing the gas saturation within an originally brine saturated sandstone layer, reduces the bulk modulus and density considerably, while the shear modulus remains unaffected (Figure 6.3.4). Consequently, the V_p is reduced significantly and V_s is slightly increased, so that the velocity ratio is lowered. The results are reasonable because fluids have no resistance to shear forces, thus V_p is strictly controlled by the bulk modulus and density of the fluid, and V_s by the fluid density (Gelius and Johansen, 2010).
Due to the velocity changes of V_p and V_s, the acoustic impedance contrast between the layers above and below the gas saturated reservoir becomes larger, and the reflection coefficient increases. Thus, more energy is reflected at each interface creating brighter reflections with larger amplitudes. Observations have confirmed that the effect also increases with gas saturation, as both the AVO intercept and gradient increase negatively in the AVO crossplot (Figure 5.4.1). In case the caprock is softer than the reservoir unit originally, injecting gas into the reservoir would also induce a polarity change for the resulting reflection (Figure 5.6.1).

On another note, Arts et al. (2008) state that the carbon dioxide injected at Sleipner contain impurities of methane and heavier hydrocarbons causing large uncertainties to the density and solubility of the injected CO_2. The exact composition of various gases is not sufficiently known, however such impurities would lower the density of the gas compared to pure CO_2

(Chadwick et al., 2005). As the modelling with Gassmann assumed pure CO_2, this assumption is prone to error. Regardless, the error is presumably small considering the strong influence of gas on physical properties in general.
It is also worth considering that gases are dissolvable in both oil and brine under pressure. This implies that the physical properties of gas dissolved in brine or 'live' oil is more complex than what Wood's equation is suggesting. Hence, calculating fluid properties for homogenous mixtures with Wood's equation should be done with precaution.

7.2 Pressure and temperature effect on seismic properties

Figures 3.4.1 and 3.4.2 show that increasing the pore pressure of brine and CO_2 increase their physical properties, while the opposite apply to a temperature increase. The plots were based on Batzle and Wang's (1992) empirical relations for reservoir fluids and Span and Wagner's (1996) equation of state for CO_2. Since the confining pressure is held constant in the modelling procedure, a pore pressure increase reduces both the effective pressure and the elastic velocities. The elastic velocities are lowered as the weakening of the rock frame outweighs the stiffening of pore fluids due to the pore pressure increase. As a result, the net effect of solely increasing the pore pressure in the reservoir model was slightly reduced acoustic velocities and a slightly increased density for a gas saturated reservoir.
According to Avseth et al. (2005), the pressure effect on seismic velocities is also enhanced for unconsolidated sediments saturated with gas, indicating that pressure variations within the gas saturated Utsira reservoir influence reflections to a higher degree than if the reservoir had been brine saturated and cemented.

That the acoustic velocities are lowered with increasing pore pressure can explain why the amplitudes were very strong for all offsets in scenario 3, as both the gas saturation and pore pressure were increased, thus creating a larger acoustic impedance contrast between the interfaces. Though the contribution of the elevated pore pressure on the acoustic velocities is far less than the dense and supercritical CO_2.
Moreover, as the porosity was unaffected by the pore pressure increase in the modelling, the observed effect could be more extensive. Nevertheless, both Zweigel et al. (2004) and Chadwick and Eiken (2013) state that there were no indications of overpressure in the Utsira reservoir prior to injection, and that the possible overpressures related to the CO_2 injections are relatively small and insufficient to induce either dilation, incipient fractures or micro

seismicity. This implies that the observed amplitude anomalies in Figure 6.3.6 largely depend on the gas injections and less on the pore pressure increase. Hence, questions can be raised regarding the possibility of pore pressure being able to solely create amplitude anomalies, and to what extent the pressure needs to be raised for it to do so.
Regardless, temperature and pore pressure counteract, so a temperature increase would have the opposite effect on seismic amplitudes. Considering the large influence of gas saturation for shallow sandstone reservoirs, the effect of temperature alternations would also be weak.

7.3 Compaction effects on seismic properties

The compaction of rocks leads to porosity reduction. This either involves mechanical or chemical compaction. As porosity is reduced, the rock frame stiffens and the velocities and densities of rocks are increased. As the porosity was reduced in both scenario 2a and 2b, the observations were in correspondence with theory (Gelius and Johansen, 2010). However, the shale and cement fractions were also increased in these scenarios, so the results should be interpreted as a sum of all adjustments.
According to Avseth et al. (2005), increasing the shale fraction within a pure sandstone reservoir increases its physical properties, as the shale particles tend to clog pore throats and thereby reduce permeability and porosity. Furthermore, Avseth and Skjei (2011) state that cement increases the physical rock properties of a rock as it makes the rock frame more rigid and reduces porosity by occupying more pore space.

The seismic modelling of scenario 2 revealed that increasing the shale and cement fraction, as well as the porosity, weakened the amplitudes for the bottom reflector. At the same time it slightly strengthened the amplitudes for the top reflector. This implies that if the surroundings have a lower elastic impedance than the reservoir originally, the porosity reduction and shale - and cement increase would enhance the seismic reflections, while the opposite applies if the surroundings are stiffer.
Furthermore, Avseth et al. (2005) state that subsurface rocks are complex. Hence, it is possible to assume that the lithology and porosity may deviate slightly from well log measurements and core cuttings throughout the reservoir. Lateral variations in porosity and shale content help explain the observed amplitude variations in Figure 6.3.5.

Another aspect of compaction that was not covered by the RPMs used in this thesis involves pore geometry and the effect of fractures. The RPMs simply assume spherical pores. Avseth et al. (2014) introduced a rock physics model that accounts for the effect of altered rock texture, and this model is commonly referred to as the Kite-model. The modelling approach is shown in Figure 7.3.1.

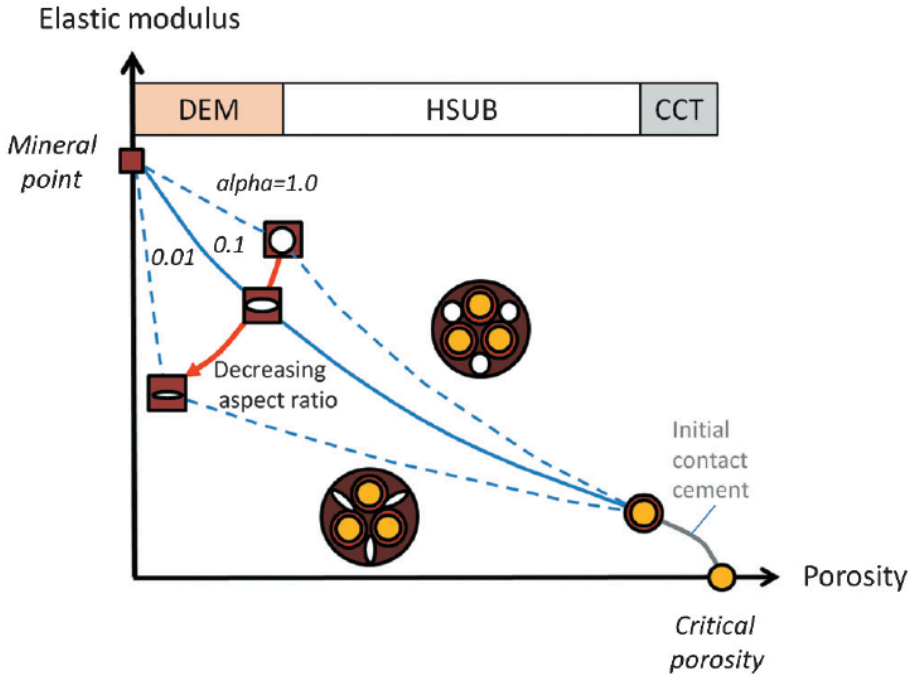

Figure 7.3.1: The modelling approach of the Kite-model, highlighting the effect of altered pore geometry on the elastic modulus of rocks. Source: Avseth et al. (2014).

Figure 7.3.1 illustrates that the elastic moduli of rocks are influenced by pore geometry, and that the effect of pore geometry increases with decreasing porosity. According to Gelius and Johansen (2010), the flatter pores are more compliant to deformation when imposed to stress, thus strengthening the pore fluids to a larger extent than spherical pores. As a result, the rock frame is weakened and the elastic properties are reduced. Consequently, injecting gas into fractures or flat pore spaces enhances the effect on velocities and density.
Nevertheless, Utsira represents a highly porous and major saline aquifer. This indicates that the amount of fractures is presumably small and stress build up can be considered negligible. Thus, the effect of pore geometry in this case study is insignificant. On the other hand, this could largely influence the seismic response of a deeper and low porous sandstone reservoir, as described in Avseth et al. (2014).

7.4 Amplitude versus offset responses

The AVO crossplot in Figure 5.4.1 shows that amplitude variations as a function of offset can be connected to various factors affecting the acoustic impedances of geological layers, and therefore seismic signatures and amplitude strength on time-lapse seismic. This includes variations in porosity, shaliness, pore pressure and gas saturation. Figure 5.4.2 also shows the AVO effect of increasing cement content.
As a result, seismic interpreters can correlate the observed amplitude variations with trends caused by the mentioned factors. However, the observed amplitude variations on time-lapse seismic are usually a result of various combinations of the mentioned factors (Avseth et al., 2005; Ivanova et al., 2013). For instance, injecting CO_2 into the reservoir would simultaneously increase the pore pressure, and an increase of cement content would simultaneously reduce the porosity. Therefore, to correlate amplitude variations to a single factor is difficult as it really is a sum of various factors. Nonetheless, it provides a good indication of what to expect, as each factor has a characteristic AVO signature (Figure 5.4.1). Furthermore, by combining the AVO analysis with other seismic attributes, e.g. AVO RPT or LMR, they can provide more certainty to the interpretations. However, a prerequisite is that the geological model is representative to the geological setting in order for the attributes to yield reliable results (Gelius and Johansen, 2010; Shadlow, 2014; Jensen et al., 2016b).

Moreover, Gelius and Johansen (2010) state that Class III and IV of the AVO anomalies are associated with gas sands in offshore settings. With this in mind, the positioning of the datapoints within the AVO crossplot seems reasonable with respect to Figure 4.2.2. It reveals that injecting CO_2 into the Utsira reservoir yields both a strong decrease in intercept and gradient, and that this trend continues with increasing gas saturation. Furthermore, by increasing the pore pressure in the reservoir the gradient increases, whereas the intercept remains almost unchanged. By reducing the porosity, and thereby compacting the reservoir rock, the intercept increases remarkably while the trend of a decreasing gradient is similar to increasing the gas saturation. Ultimately, increasing the shaliness in the reservoir has a similar AVO signature to a pore pressure increase, however it decreases the intercept to a larger extent. The results are in correspondence with other AVO/AVA related studies for gas sands and can therefore be considered reliable (Ivanova et al., 2013; Castagna et al., 1998; Avseth and Lehocki, 2016).

The modelled AVO responses in this thesis indicate that injecting CO_2 into the Utsira reservoir create Class III AVO anomalies on time-lapse seismic. On the other hand, the observed AVO anomalies on actual time-lapse seismic data from Sleipner indicate that the AVO anomalies correspond to Class IV as the amplitudes decrease with offset. The difference is most likely caused by the difference between the modelled properties of the caprock compared to the actual properties of the caprock. According to both Castagna et al. (1998) and Avseth and Lehocki (2016), a porous sand overlain by a high-velocity unit, such as a hard shale, creates Class IV AVO anomalies. Conversely, a reservoir overlain by a soft caprock creates Class III AVO anomalies. This is in correspondence with the fact that the caprock was represented as a peak on seismic from Sleipner, indicating that it was originally stiffer than the underlaying sands. This was in contrast to the modelling, which assumed a softer caprock. According to Avseth and Bachrach (2005), Class IV AVO signatures are also commonly observed in shallow and unconsolidated sediments as the velocity ratio is strongly affected by the reduced shear effect even though the elastic impedances are relatively weakly affected. As mentioned earlier, Chadwick et al. (2010) also confirmed that the amplitude anomalies correspond to Class IV AVO anomalies. As both the caprock and reservoir properties influence the AVO signature, prove the importance of including the correct shale trends for the geological setting, and accounting for the slip factor of unconsolidated sediments.

7.5 Amplitude attenuation and wavelet effects on AVO

Seismic waves lose energy with depth as their energy is either reflected at interfaces or converted to heat during transmission. Furthermore, higher frequency waves are rapidly attenuated with depth, decreasing the resolution of the seismic image. The attenuation of seismic waves is related to geometrical spreading and anelastic attenuation. Rocks containing gas also have lower quality factor (Q) values, implying that gas injections results in larger absorption and increased intrinsic attenuation of the elastic waves (Gelius and Johansen, 2010).

During the seismic modelling procedure, neither geometrical spreading or anelastic attenuation were included in order to preserve the true amplitude strength at each interface. However, the actual seismic from Sleipner is influenced by geometrical spreading and anelastic attenuation. This implies that the amplitude strength will decrease with depth, and if not accounted for, it will result in erroneous interpretations of AVO effects as the reflections do not display true amplitude values. This explains why it is crucial to do pre-processing of

seismic data to ideally obtain true amplitudes that are horizontally aligned along the zero-offset trace in time. The observed amplitude anomalies are then directly linked to factors influencing the seismic response and not by disturbances related to for example noise, interference and velocity estimation (Avseth et al., 2005; Gelius and Johansen, 2010). Nonetheless, as the AVO data from Sleipner were pre-processed it is possible to assume that amplitude recovery and similar processing techniques have been applied to minimize disturbances and optimalize the seismic for AVO-analysis. This also includes accounting for the velocity push-down effect for seismic reflections influenced by the presence of CO_2. The effect of including both geometrical spreading and anelastic attenuation on seismic amplitudes can be observed in Figure 7.5.1. A zero-phase Ricker wavelet of 60 Hz was used to enhance the attenuation effect on seismic amplitudes.

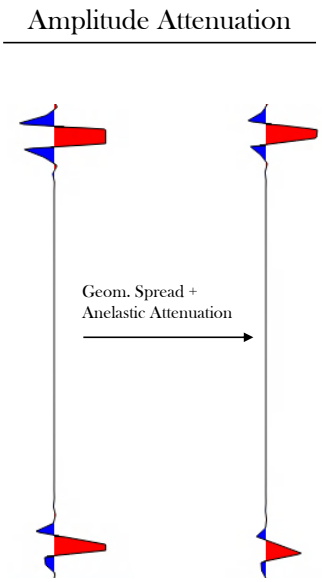

Figure 7.5.1: The effect of including geometrical spreading and anelastic attenuation on seismic amplitudes for the basis scenario (Figure 5.3.1). The left trace represent amplitudes without amplitude attenuation, while the right trace includes amplitude attenuation.

Shadlow (2014) also describes tuning as a potential pitfall for studying amplitude effects, as constructive interference enhances the amplitudes, while destructive interference weakens the amplitudes. The maximum amplitude strength as a result of tuning is related to wavelet frequency and layer thickness, and is commonly referred to as the tuning thickness. A zero-phase Ricker wavelet of 30Hz was used in the modelling procedure, and the interval velocity for the brine saturated Utsira reservoir was 2030 m/s. This gives a tuning thickness of 13 m (Shadlow, 2014).

A higher frequency wavelet would reduce the tuning thickness, so that thinner beds are revealed on the seismic image. However, since each layer within the reservoir model is 66 m thick, the effect of tuning can be neglected for the synthetic results. On the other hand, Arts et al. (2004) state that tuning effects occur on the seismic images from Sleipner, concealing the thin intra-layering shales. The presence of several thin intra-layering shales explains however the reason why several strong amplitude anomalies can be observed within the Utsira reservoir, as the intra-layering shales block upward migration of CO_2 and create several individual layers of gas sand.

Moreover, the polarity of the seismic represents another aspect of potential interpretation error as a reversed polarity would interpret hard geological events such as volcanic intrusions and limestones as bright spot anomalies. Therefore, by understanding the geological setting it can help to predict what type of DHI is expected so that such interpretations errors are avoided. The sea-bottom reflector can also be utilized as a reference to confirm polarity ambiguities as it represents a strong interface between seawater and sediments. The aspect of polarity between the seismic from Sleipner and the synthetic results were addressed in the previous chapter (Figure 6.3.1).

7.6 Reliability of the results

The seismic modelling results are synthetic, thus the reliability of the results can be evaluated accordingly. Firstly, the well measurements from Well 15/9-13 were inconsistent and contained uncertainties in specific intervals related to density and velocities. Several assumptions were made in order to modify and calibrate usable well log data. Based on the fact that the calibrated rock physics model was based on calibrated well log data from Well 15/9-13, the RPM is prone to error as the majority of measurements are based on assumptions. Chadwick et al. (2004) also stated that due to the large spacing of wells within the area and the lack of core material from which to derive measurements of the physical properties of the rock, limits the availability to construct a detailed reservoir model.

From a different perspective, the input in the RPM was compared with similar studies at Sleipner characterizing both the Utsira reservoir and overburden in terms of physical properties and conditions (Chadwick and Eiken, 2013; Chadwick et al., 2004; Arts et al., 2008; Rabben and Ursin, 2011). Additionally, data versus model were cross-plotted to ensure model integrity (Appendix B). The rock physics model provide a good fit for the bulk

modulus in the reservoir zone, while the overburden is slightly overpredicted and the sequence below is slightly underpredicted. The density provide a perfect fit for all three units as it is derived from the calibrated porosity log. The shear modulus provided a mediocre fit between data and model as the S-wave velocity was derived empirically from the P-wave velocity log.

Moreover, rock physical models are not able to account for every detail of a complex subsurface (Box, 1976). Details that may include shales with varying mineral composition and elastic properties, anisotropy or chemical interactions between grains and fluids (Batzle and Wang, 1992; Avseth et al., 2005). The models also assumes pure fluid saturations of either CO_2 and brine. Arts et al. (2008) state that the injected CO_2 contains impurities. This indicates that the modelling of fluid effects are erroneous. As a consequence, the modelled acoustic impedances and reflectivities might slightly deviate from their actual values.

Nonetheless, Jensen et al. (2016a) suggest using the friable sandstone model to predict physical properties as this model provides the most reliable results for shallow and unconsolidated sands. Avseth et al. (2005) also recommend using this modelling approach with respect to the geological setting at Utsira, thus providing confidence to the results presented in this thesis.
Ultimately, the modelling provided robust results as both the seismic signatures and AVO trends were in correspondence with theory and similar AVO studies (Avseth et al, 2005; Avseth and Lehocki, 2016; Ivanova et al., 2013; Chadwick et al., 2010; Shadlow, 2014; Castagna et al., 1998). The results can therefore be considered reliable and useful to similar studies involving carbon sequestration in shallow and unconsolidated sands.

8 Conclusion

8.1 Conclusions

- The amplitude anomalies occurring on time-lapse seismic from Sleipner correspond to Class IV AVO anomalies, and can be characterized as seismic bright spots. The amplitudes were exclusively influenced by gas saturation, and less by pore pressure and temperature alternations. Distinguishing CO_2 saturation from pressure and temperature effects are therefore difficult.

- CCS has the potential to play a key role in an interconnected system between the fossil fuel and renewable sector, by storing large quantities of anthropogenic emissions in the subsurface while simultaneously being able to produce clean hydrogen energy.

- Time-lapse seismic monitoring ensures storage capacity and efficiency, thus the integrity of carbon storage.

- Rock physics and seismic modeling are able to predict the seismic response of various hypothetical geological scenarios related to the sequestration of carbon dioxide. This is useful to predict time-lapse responses of CO_2 injections. However, a prerequisite is that the RPM is representative to the geological setting under consideration.

- Seismic attributes, e.g. AVO intercept versus gradient, can improve the interpretation of AVO effects as various factors influencing the physical properties of an effective rock, thus the seismic response, have characteristic AVO signatures (Figure 5.4.1). Though in reality it can be challenging to distinguish each contribution as it is usually a sum of various factors.

- It is crucial to understand the physical principles of grains and fluids and the geological setting of an area of interest when doing seismic interpretation to avoid pitfalls, as it connects geophysical responses to geology.

- It is important to be aware of potential errors related to the pre-processing of seismic data, as it might cause disturbances to the true amplitude values, thus affecting the reliability of the AVO-analysis.

8.2 Further research

Several aspects related to carbon sequestration and seismic monitoring were not covered in this thesis. Aspects that could be interesting for further studies involve the effect of injecting gas into tight and low porous sandstones, as such reservoirs would be largely influenced by pore geometry (Figure 7.3.1). Other areas of interest involve the effect of anisotropy and its influence on seismic signatures, and chemical interactions between grains and fluids. Ultimately, the effect of gas impurities related to methane and heavier hydrocarbons causing large uncertainties to the density and solubility of the injected CO_2.

9 References

Aki, K.I., Richards, P.G., 1980. *Quantitative seismology: Theory and methods*. W.H. Freeman & Co.

Andersen, C., Johansen, T.A., 2010. *Test of rock physics models for prediction of seismic velocities in shallow unconsolidated sands: a well log data case.* Geophysical Prospecting, Vol. 58. 1083-1098. DOI: 10.1111/j.1365-2478.2010.00870.x

Anderson, J. et al., 2005. *Underground geological storage.* In Metz, B. (ed.). *IPCC Special Report on Carbon Dioxide Capture and Storage*. Cambridge University Press. ISBN-13 978-0-521-86643-9.

Avseth, P., 2010. *Explorational Rock Physics – The Link Between Geological Processes and Geophysical Observables.* In Bjørlykke, K. (ed.). *Petroleum Geoscience: From Sedimentary Environments to Rock Physics*. Springer-Verlag Berlin Heidelberg. 403-426. DOI 10.1007/978-3-642-02332-3_19.

Avseth, P., Bachrach, R., 2005. *Seismic properties of unconsolidated sands: Tangential stiffness, Vp/Vs ratios and diagenesis.* Society of Exploration Geophysicists. DOI: 10.1190/1.2147968.

Avseth, P. et al., 2014. *Rock-physics modeling guided by depositional and burial history in low-to-intermediate-porosity sandstones*. Geophysics. Vol. 79 (2). DOI: 10.1190/GEO2013-0226.1

Avseth, P., Lehocki, I., 2016. *Combining burial history and rock-physics modeling to constrain AVO analysis during exploration*. The Leading Edge. Vol. 35 (6). 936-942. DOI: 10.1190/tle35060528.1.

Avseth, P., Mukerji, T., Mavko, G., 2005. Quantitative Seismic Interpretation: *Applying Rock Physics Tools to Reduce Interpretation Risk.* Cambridge University Press. ISBN: 9780521816014

Avseth, P., Skjei, N., 2011. *Rock physics modeling of static and dynamic reservoir properties – a heuristic approach for cemented sandstone reservoirs.* The Leading Edge. Vol. 30 (1). DOI: 10.1190/1.3535437

Arts, R. et al., 2004. *Seismic monitoring at the Sleipner underground CO_2 storage site (North Sea).* Geological Society of London. Special Publications. Vol. 233. 181-191. DOI: 10.1144/GSL.SP.2004.233.01.12.

Arts, R. et al., 2008. *Ten years' experience of monitoring CO_2 injection in the Utsira Sand at Sleipner, offshore Norway.* First Break, Vol. 26, 65-72.

Batzle, M. and Wang, Z., 1992. *Seismic properties of pore fluids.* Geophysics 57, 1396-1408

Benjaminsen, C., 2019. *Dette må du vite om fangst og lagring av CO_2.* SINTEF. Available at: https://www.sintef.no/siste-nytt/dette-ma-du-vite-om-ccs-karbonfangst-og-lagring/ Accessed: 02.11.20

Berge, U. et al., 2016. *Carbon Capture and Storage*. Zero Emission Resource Organization (ZERO). Available at: https://zero.no/wp-content/uploads/2016/06/carbon-capture-and-storage.pdf Accessed: 27.10.20.

Bjørlykke, K., 2015. *Petroleum Geoscience: From Sedimentary Environments to Rock Physics*. Springer – Verlag Berlin Heidelberg. ISBN 978-3-642-02331-6

Box, G., 1976. *Science and statistics.* Journal of the American Statistical Association. Vol. 71 (356). 791–799.

Bredesen, K., 2012. *Figure 1.1* [Photography]. Available at: https://bora.uib.no/bora-xmlui/handle/1956/7462 Accessed: 07.11.20

Brown, P. et al., 2020. *The Role of Carbon Capture and Storage in a Carbon Neutral Europe.* Carbon Limits AS and THEMA Consulting Group. Available at: https://www.regjeringen.no/contentassets/971e2b1859054d0d87df9593acb660b8/ Accessed: 28.10.20

Bøe, R., et al., 2002. *CO_2 point sources and subsurface storage capacities for CO_2 aquifers in Norway.* Norges Geologiske Undersøkelse (NGU). ISSN: 0800-3416

Castagna, J., Swan, H., Foster, D., 1998. *Framework for AVO gradient and intercept interpretation.* Geophysics. Vol. 63 (3). 948-956. DOI: 10.1190/1.1444406.

Chadwick, R. A., Arts, R., Eiken, O., 2005. *4D seismic quantification of a growing CO_2 plume at Sleipner, North Sea.* British Geological Survey. 1385-1399.

Chadwick, R.A., Eiken, O., 2013. *Offshore CO2 storage: Sleipner natural gas field beneath the North Sea.* In: Gluyas, M., Jon, S. (ed.). *Geological Storage of Carbon Dioxide (co2): geoscience, technologies, environmental aspects and legal frameworks.* British Geological Survey. 227-253.

Chadwick, R.A. et al., 2008. *Best Practice For The Storage Of CO_2 In Saline Aquifers: Observations and guidelines from the SACS and CO2STORE projects.* British Geological Survey. Vol. 14. 1-267.

Chadwick, R.A. et al., 2004. *Geological reservoir characterization of a CO_2 storage site: The Utsira Sand, Sleipner, northern North Sea.* Energy. Vol. 29. 1371-1381.

Chadwick, R.A. et al., 2010. *Quantitative analysis of time-lapse seismic monitoring data at the Sleipner CO2 storage operation.* The Leading Edge. Vol. 29 (2). DOI: 10.1190/1.3304820

Coleman, D. et al., 2005. *Transport of CO_2*. In Metz, B. (ed.). *IPCC Special Report on Carbon Dioxide Capture and Storage*. Cambridge University Press. ISBN-13 978-0-521-86643-9.

The Comet Program, 2010. *Soil Texture Classification*. [Photography]. Available at: http://ftp.comet.ucar.edu/memory-stick/hydro/basic_int/runoff/navmenu.php_tab_1_page_4.1.0.htm Accessed: 20.01.21

Coninck, H. et al., 2010. *Carbon Capture and Storage in Industrial Applications.* United Nations Industrial Development Organization. Available at: https://www.unido.org/sites/default/files/2010-12/synthesis_final_0.pdf Accessed: 29.10.20

Dvorkin, J., Nur, A., 1996. *Elasticity of high-porosity sandstones: Theory for two North Sea data sets.* Geophysics. Vol. 61 (5). 1363–1370.

Equinor, 2020. *Carbon capture, utilisation and storage (CCS and CCUS).* Equinor. Available at: https://www.equinor.com/en/what-we-do/carbon-capture-and-storage.html. Accessed: 07.09.20.

Equinor, 2019. *CO2 Capture* v2 [Photography]. Available at: https://communicationtoolbox.equinor.com/brandcenter/en/equinorbc/component/default/22936 Accessed: 28.10.20

Furre, A.K. et al., 2016. *20 years of monitoring CO2-injection at Sleipner*. Energy Procedia. Vol. 114. 3916-3926.

Ganguli, S., 2017. *Rock Physics Modeling of Ankleshwar Reservoir: A CO2 EOR Perspective.* In: Integrated Reservoir Studies for CO2-Enhanced Oil Recovery and Sequestration. SpringerLink. 71-98. ISBN: 978-3-319-55843-1.

Gardner, G.H.F., Gardner, L.W., Gregory, A.R., 1974. *Formation velocity and density – The diagnostic basis for stratigraphic traps.* Geophysics. Vol. 39. 770-780.

Gassmann, F., 1951. *Elasticity of porous media: Uber die elastizitat poroser medien.* Vierteljahrsschrift der Naturforschenden Gesselschaft, Vol. 96, 1-23.

Gassnova, 2020. *CCS comprises the capture, transport and storage of CO_2 emissions.* [Photography]. Available at: https://www.norskpetroleum.no/en/environment-and-technology/carbon-capture-and-storage/ Accessed: 13.11.20

Gelius, L. J. and Johansen, T. A., 2010. *Petroleum Geophysics.* UniGeo: GeoClass. Available at: https://geoclass.no/

Gierzynski, A., 2016. *Phase Diagram for CO_2.* [Photography]. Available at: https://www.researchgate.net/figure/Phase-diagram-for-CO2 Accessed: 11.12.20

Gregersen, U., Michelsen, O., Sorensen, J., 1997. *Stratigraphy and facies distribution of the Utsira Formation and the Pliocene sequences in the northern North Sea.* Marine and Petroleum Geology. Vol. 14. 893-914.

Halland, E. et al., 2011. *CO_2 Storage Atlas Norwegian North Sea.* Norwegian Petroleum Directorate (NPD). Available at: https://www.npd.no/globalassets/1-npd/publikasjoner/atlas-eng/co2-atlas-north-sea.pdf Accessed: 13.11.20

Hellevang, H., 2015. *Carbon Capture and* Storage. In: Bjørlykke, K. (ed.). *Petroleum Geoscience: From Sedimentary Environments to Rock Physics – Second Edition.* Springer – Verlag Berlin Heidelberg. ISBN: 9783642341311

Hermanrud, C. et al., 2009. *Storage of CO_2 in saline aquifers – Lessons learned from 10 years of injection CO_2 into the Utsira Formation in the Sleipner area.* Energy Procedia. Vol. 1. 1997-2004. DOI: 10.1016/j.egypro.2009.01.260

Herzog, H., Golomb, D., 2004. *Carbon Capture and Storage from Fossil Fuel Use*. Encyclopedia of Energy, Vol.1 (6562). 277-287. DOI: 10.1016/B0-12-176480-X/00422-8

Hill, R., 1963. *Elastic properties of reinforced solids: Some theoretical principles*. Journal of the Mechanics and Physics of Solids. Vol. 11, 357–372.

Holmås, H. E. et al., 2019. *Hvordan gjøre CO2-fangst og -lagring lønnsomt*. Multiconsult. DOI: 10209499-TVF-RAP-001.

IEA, 2019. *Global Energy & CO2 Status Report 2019*. International Energy Agency, Paris. Available at: https://www.iea.org/reports/global-energy-co2-status-report-2019. Accessed: 07.09.20

IPCC, 2014. *Climate Change 2014: Synthesis Report.* Contribution of Working Groups I, II and III to the Fifth Assessment Report of the Intergovernmental Panel on Climate Change [Core Writing Team, R.K. Pachauri and L.A. Meyer (eds.)]. IPCC, Geneva, Switzerland, 151 pp.

IPCC, 2013. *Climate Change 2013: The Physical Science Basis.* Contribution of Working Group I to the Fifth Assessment Report of the Intergovernmental Panel on Climate Change [Stocker, T.F., D. Qin, G.-K. Plattner, M. Tignor, S.K. Allen, J. Boschung, A. Nauels, Y. Xia, V. Bex and P.M. Midgley (eds.)]. Cambridge University Press, Cambridge, United Kingdom and New York, NY, USA, 1535 pp.

Ivanova, A. et al., 2013. *Seismic modeling of the AVO/AVA response to CO2 injection at the Ketzin site, Germany.* Energy Procedia. Vol. 40. 490-498.

Jensen, E. H. et al., 2016a. *Rock.XML – Towards a library of rock physics models.* Computers & Geosciences. Vol. 93. 63-69. DOI:10.1016/j.cageo.2016.04.011

Jensen, E.H. et al., 2016b. *Quantitative interpretation using inverse rock-physics modeling on AVO data.* The Leading Edge, Vol. 35 (8). 677-683.

Jullum, M. and Kolbjørnsen, O., 2016. *A Gaussian-based framework for local Bayesian inversion of geophysical data to rock properties.* Geophysics, Vol. 81 (3). DOI: 10.1190/geo2015-0314.1

Kalam, S et al., 2020. *Fig. 8* [Photography]. Available at: https://media.springernature.com/lw685/springer-static/image/art%3A10.1007%2Fs13202-020-01028-7/MediaObjects/13202_2020_1028_Fig8_HTML.png?as=webp Accessed: 12.04.21

Kearey, P., Brooks, M., Hill, I., 2002. *An Introduction to Geophysical Exploration, 3rd Edition.* Blackwell Science Ltd. ISBN: 978-0-632-04929-5.

Kirby, G., Chadwick, R., Holloway, S., 2001. *Depth mapping and characterization of the Utsira Sand Saline Aquifer, Northern North Sea.* British Geological Survey. Commissioned Report. Vol. 1 (233). 1-26.

Landrø, M., 2010. *4D* seismic. In Bjørlykke, K. (ed.). *Petroleum Geoscience: From Sedimentary Environments to Rock Physics*, Springer-Verlag Berlin Heidelberg. 427-444. DOI 10.1007/978-3-642-02332-3_19.

Levina, E. et al., 2013. *Technology Roadmap: Carbon Capture and Storage*. International Energy Agency (IEA). Available at: https://www.iea.org/reports/technology-roadmap-carbon-capture-and-storage-2013 Accessed: 13.11.20.

Lumley, D., 2010. *4D seismic monitoring of CO2 sequestration*. The Leading Edge, Vol. 29 (2). 150–155. DOI: 10.1190/1.3304817

Låg, M. et al., 2009. *Health effects of different amines and possible degradation products relevant for CO_2 capture*. Folkehelseinstituttet. ISBN: 978-82-8082-322-9-2

Mavko, G., Mukerji, T., Dvorkin, J., 2009. *Rock Physical Handbook: Tools for Seismic Analysis of Porous Media*. Cambridge University Press. ISBN: 9780521861366

Moe, A. et al., 2020. *A Trans-European CO_2 Transportation Infrastructure for CCUS: Opportunities & Challenges.* Zero Emission Platform. Available at: https://zeroemissionsplatform.eu/wp-content/uploads/A-Trans-European-CO2-Transportation-Infrastructure-for-CCUS-Opportunities-Challenges-1.pdf Accessed: 29.10.20

NASA, 2020. *Direct Measurement of Atmospheric CO_2: 2005-present.*[Photography]. Available at: https://climate.nasa.gov/vital-signs/carbon-dioxide/ . Accessed: 05.09.20.

Nguyen. P., Nam, M., 2011. *A review on Methods for Constructing Rock Physics Model of Saturated Reservoir Rock for Time-Lapse Seismic.* Geosystem Engineering, Vol. 14 (2). 95-107.

Northern Lights Project, 2020. *Northern Lights – Part of the full-scale CCS project in Norway*. NLP. Available at: https://northernlightsccs.com/en/about Accessed: 15.11.20

NPD, 2021a. *Wellbore 15/9-13*. Norwegian Petroleum Directorate. Available at: https://factpages.npd.no/nb-no/wellbore/PageView/Exploration/Wdss/45 Accessed: 15.02.21

NPD, 2021b. *Interactive map.* [Photography]. Available at: https://www.norskpetroleum.no/en/interactive-map-quick-downloads/interactive-map/ Accessed: 15.04.21

Odegaard, E., Avseth, P., 2004. *Well log and seismic data analysis using rock physics templates*. First Break. Vol. 22. 37-43.

Onyebuchi, V., 2018. *A systematic review of key challenges of CO_2 Transport via pipelines*. Cranfield University. DOI: 10.1016/j.rser.2017.06.064

Pales, A. et al., 2019. *Exploring Clean Energy Pathways: The Role of CO2 Storage*. International Energy Agency (IEA). Available at: https://www.iea.org/reports/the-role-of-co2-storage Accessed: 13.11.20.

Rabben, T. E., Ursin, B., 2011. *AVA inversion of the top Utsira Sand reflection at the Sleipner Field*. Geophysics. Vol. 76 (3). DOI: 10.1190/1.3567951

Reuss, A., 1929. *Berechnung der Flie_grenzen von Mischkristallen auf Grund der Plastizitatsbedingung fur Einkristalle.* ZAMM - Journal of Applied Mathematics and Mechanics / Zeitschrift fur Angewandte Mathematik und Mechanik. Vol. 9 (1). 49-58.

Rutherford, S.R., Williams, R.H., 1989. *Amplitude-versus-offset variations in gas sands.* Geophysics. Vol. 54 (6). DOI: 10.1190/1.1442696.

Sandø, I., Munkvold, O., Elde, R., 2009. *4D Geophysical Data*. GEO ExPro. Vol. 6 (5).

Satyapal, S., 2017. *Hydrogen: A Clean , Flexible Energy Carrier*. Energy Efficiency & Renewable Energy. Available at: https://www.energy.gov/eere/articles/hydrogen-clean-flexible-energy-carrier Accessed: 29.10.20

Schlumberger, 2019. *Time-lapse 4D Analysis and Interpretation.* Schlumberger. Available at: https://www.slb.com/reservoir-characterization/seismic/seismic-reservoir-characterization/time-lapse-4d-analysis-and-interpretation Accessed: 08.09.20

Shadlow, J., 2014. *A description of seismic amplitude techniques.* Exploration Geophysics. Vol. 45 (3). 154-163. DOI: 10.1071/EG13070

Solomon, S., 2007. *Carbon Dioxide Storage: Geological Security and Environmental Issues – Case Study on the Sleipner Gas Field in Norway.* The Bellona Foundation. 1-128.

Span, R. and Wagner, W., 1996. *A New Equation of State for Carbon Dioxide Covering the Fluid Region from Triple-Point Temperature to 1100K at Pressures up to 800 MPa.* Journal of Physical and Chemical Reference Data, Vol. 25 (6), 1509-1596.

Stub, S. Ø. et al. 2019. *New business models for carbon capture and storage.* Zero Emission Resource Organisation (ZERO). Available at: https://zero.no/wp-content/uploads/2019/09/rapport-eng-ccs-v6.pdf Accessed: 15.10.20.

Størset, S. Ø. et al., 2018. *Industrielle muligheter og arbeidsplasser ved CO2-håndtering i Norge.* SINTEF. ISBN: 978-82-14-6887-0.

Voigt, W. 1928. Lehrbuch der Kristallphysik. Teubner, Berlin, 962.

Walpole, L. J. (1966a). *On bounds for the overall elastic moduli of inhomogeneous systems–I.* Journal of the Mechanics and Physics of Solids. Vol. 14. 151–162.

Walpole, L. J. (1966b). *On bounds for the overall elastic moduli of inhomogeneous systems–II.* Journal of the Mechanics and Physics of Solids. Vol. 14. 289–301.

Walton, K., 1987. *The effective elastic moduli of a random packing of spheres.* J. Mech. Phys. Solids. Vol. 35. 213-226.

Wiggins, R., Kenny, G. S., McClure, C.D., 1984. *A method for determining and displaying the shear-wave reflectivities of a geological formation.* European Patent Application 0113944.

Wood, A.W., 1955. *A textbook of Sound*. The MacMillan Co., New York. 360 pp.

ZEP, 2011. *The Costs of CO_2 Capture, Transport and Storage*. Zero Emission Platform. Available at: https://zeroemissionsplatform.eu/wp-content/uploads/Overall-CO2-Costs-Report.pdf Accessed: 29.10.20

Zweigel, P. et al., 2000. *Prediction of migration of CO_2 injected into an underground depository: reservoir geology and migration modelling in the Sleipner case (North Sea).* In Williams, D. et al. (ed.). *Greenhouse Gas Control Technologies, Proceedings of the 5th International Conference on Greenhouse Gas Control Technologies.* CSIRO Publishing. 360-365.

Zweigel, P. et. al., 2004. *Reservoir Geology of the Utsira Formation at the first industrial-scale underground CO_2 storage site (Sleipner area, North Sea).* Geological Society of London, Special Publications. Vol. 233. 165-180.

Appendix A

Generalized elastodynamic wave equation

$$\rho \frac{\partial^2 u_i}{\partial t^2} - \frac{\partial}{\partial x_l}\left(c_{ijkl}\frac{\partial u_k}{\partial x_j}\right) = 0 \tag{A1}$$

t = time, c_{ijkl} = fourth order elastic stiffness tensor, u = displacement vector.

Generalized version of Hooke's law for a solid isotropic medium

$$\sigma_{xz} = 2\mu\varepsilon_{xz} \tag{A2}$$

$$\sigma_{yz} = 2\mu\varepsilon_{yz} \tag{A3}$$

σ = stress, ε = strain.

Walton's Contact Theory

In order to derive effective elastic rock properties at the critical porosity point with Walton's (1987) contact theory, the model requires input about Poisson's ratio, coordination number and critical porosity, in addition to the Lamé coefficient of the material and the confining pressure:

$$K_{walt} = \frac{1}{6}\left[\frac{3(1-\phi_c)^2 C^2 P}{\pi^4 B^2}\right]^{\frac{1}{3}} \tag{A4}$$

where K_{walt}, ϕ_c, C, P represent bulk modulus, critical porosity, coordination number and pressure. B is a constant given by equation (3.18).

$$B = \frac{1}{4\pi}\left(\frac{1}{\mu} + \frac{1}{\mu+\lambda}\right) \tag{A5}$$

Where μ and λ represent the shear modulus and Lamé coefficient. The effective shear modulus is calculated by incorporating a friction factor (f) in combination with a weighted average between the upper and lower effective shear modulus of Walton's theory:

$$\mu_{walt*} = f\mu_{W+} + (1-f)\mu_{W-} \quad \text{(A6)}$$

where μ_{W+} and μ_{W-} are expressed through the bulk modulus (K_{walt}) and Poisson's ratio (v) of the effective solid:

$$\mu_{W+} = \frac{3}{5}K_{walt} \ , \qquad \mu_{W-} = \frac{3}{5}K_{walt}\frac{5-4v}{2-v} \quad \text{(A7)}$$

Contact Cement Theory

The contact cement theory established by Dvorkin and Nur (1996) describes the elastic moduli of cemented sediments:

$$K_{CCT} = \frac{1}{6}C(1-\phi_{cr})M_c S_n \quad \text{(A8)}$$

$$\mu_{CCT} = \frac{3}{5}K_{CCT} + \frac{3}{20}C(1-\phi_{cr})\mu_c S_\tau \quad \text{(A9)}$$

$$M_c = p_c V_{p_c}^2 \quad \text{(A10)}$$

$$\mu_c = p_c V_{s_c}^2 \quad \text{(A11)}$$

where ϕ_{cr}, p_c , V_{s_c}, V_{p_c} are the critical porosity, density, and P -and S-wave velocities of the cement constituent. M_c and μ_c are the compressional and shear modulus of the cement constituent. S_τ and S_n are parameters that are related to the normal and shear stiffness, and varies with type of cement, grain properties and the amount of cement.

The contact cement model assumes that all grain contacts will be cemented as cementation initiates, hence the stress sensitivity vanishes for minor cement volumes (<10%) (Avseth and Skjei, 2011).

Coefficients for plane-wave R_{pp}

The ray parameter p is defined below.

$$p = \frac{sin\theta_1}{V_{p1}} = \frac{sin\theta_2}{V_{p2}} = \frac{sin\phi_1}{V_{p1}} = \frac{sin\phi_2}{V_{p2}} \quad \text{(A12)}$$

where θ_1 and θ_2 are the incidence and reflection angles respectively. ϕ_1 and ϕ_2 are the porosities in the respective layers.

The remaining coefficients in equation (4.1) are defined below.

$$a = \rho_2(1 - 2V_{s2}^2\rho^2) - \rho_1(1 - 2V_{s1}^2\rho^2) \tag{A13}$$

$$b = \rho_2(1 - 2V_{s2}^2\rho^2) + \rho_1 V_{s1}^2\rho^2) \tag{A14}$$

$$c = \rho_1(1 - 2V_{s1}^2\rho^2) + 2\rho_2 V_{s2}^2\rho^2) \tag{A15}$$

$$d = 2(\rho_2 V_{s2}^2 - \rho_1 V_{s1}^2) \tag{A16}$$

$$D = EF + GH\rho^2 \tag{A17}$$

$$E = b\frac{cos\theta_1}{V_{p1}} + c\frac{cos\theta_2}{V_{p2}} \tag{A18}$$

$$F = b\frac{cos\phi_1}{V_{s1}} + c\frac{cos\phi_2}{V_{s2}} \tag{A19}$$

$$G = a - d\frac{cos\theta_1}{V_{p1}}\frac{cos\phi_2}{V_{s2}} \tag{A20}$$

$$H = a - d\frac{cos\theta_2}{V_{p2}}\frac{cos\phi_1}{V_{s1}} \tag{A21}$$

where indices 1 and 2 represent the layers above and below a reflecting interface.

Appendix B

The original well log 15/9-13 before and after modifications is shown below, in addition to data versus model crossplots for bulk and shear modulus and density in the interval of interest. This includes the caprock, reservoir rock and below, from 750 – 1100 m depth. Ultimately, the input used to create the AVO RPT plot are presented.

Well 15/9-13

Original

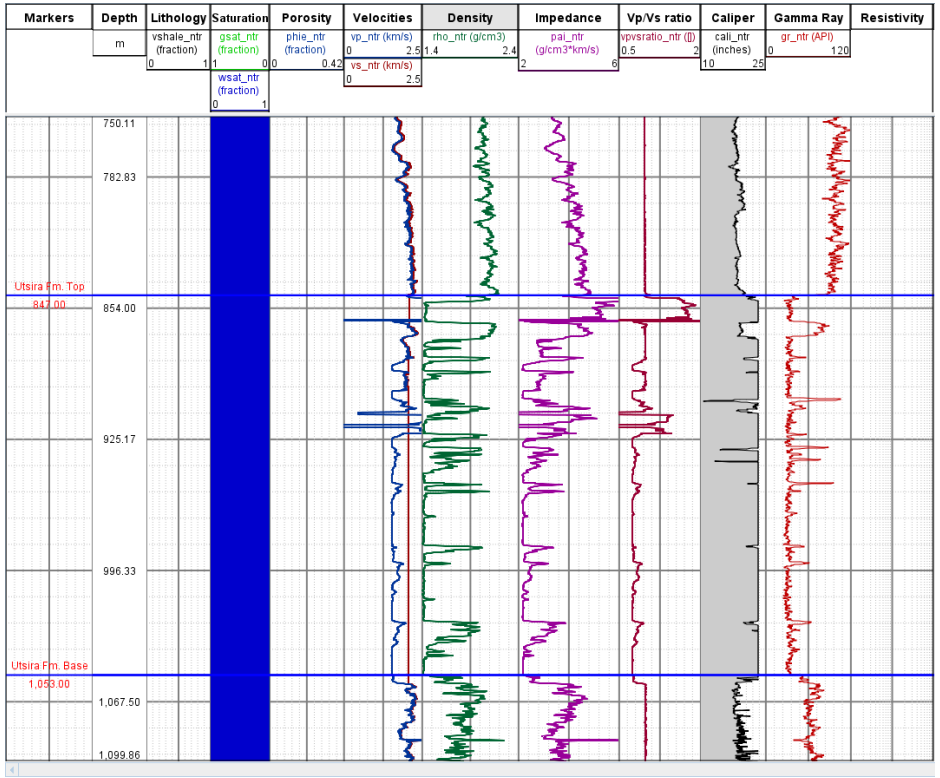

Modified

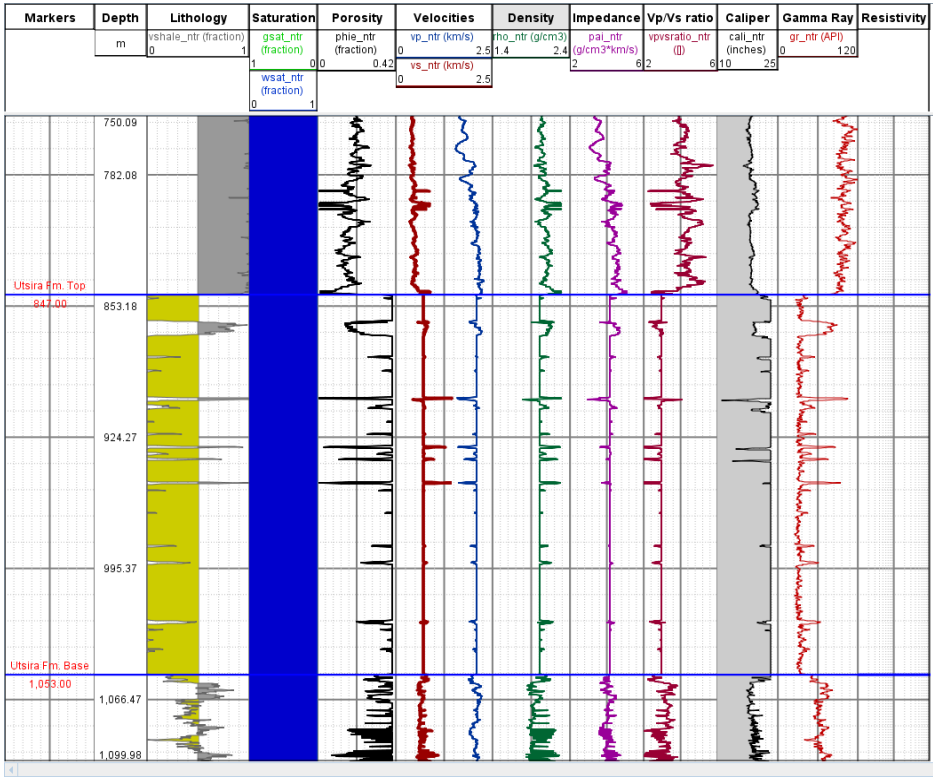

Data versus Model

Bulk Modulus:

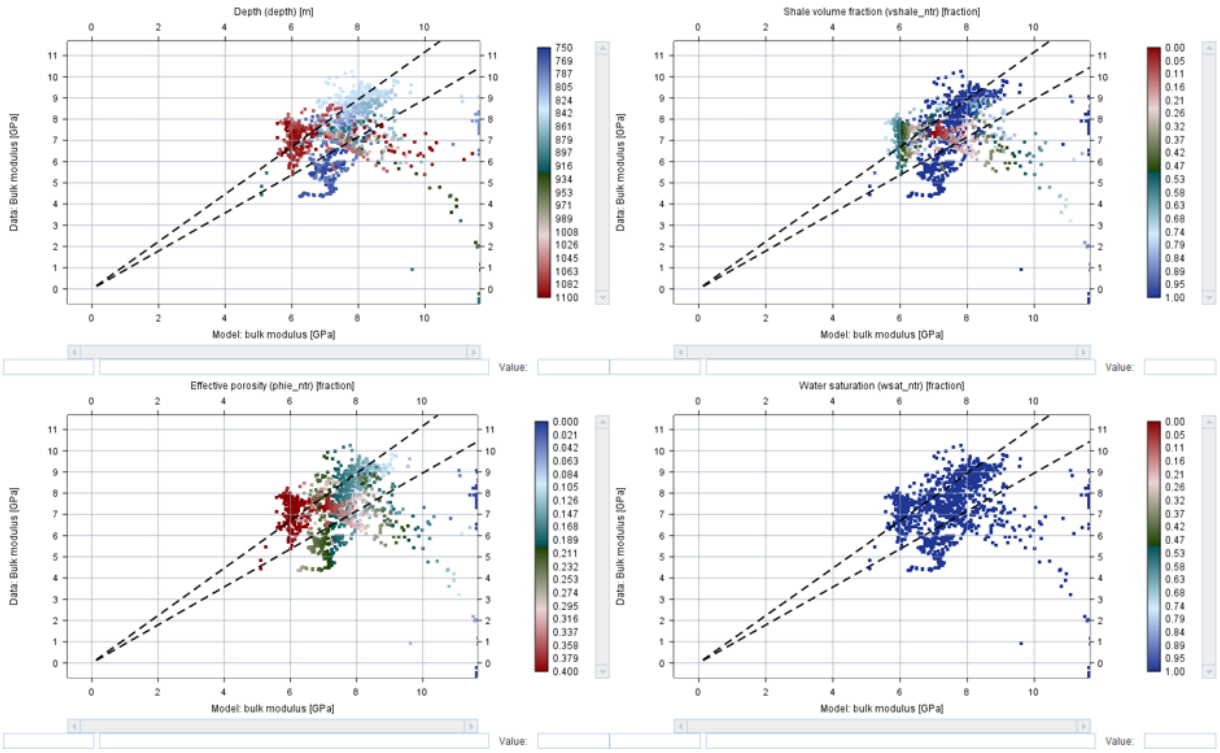

Density:

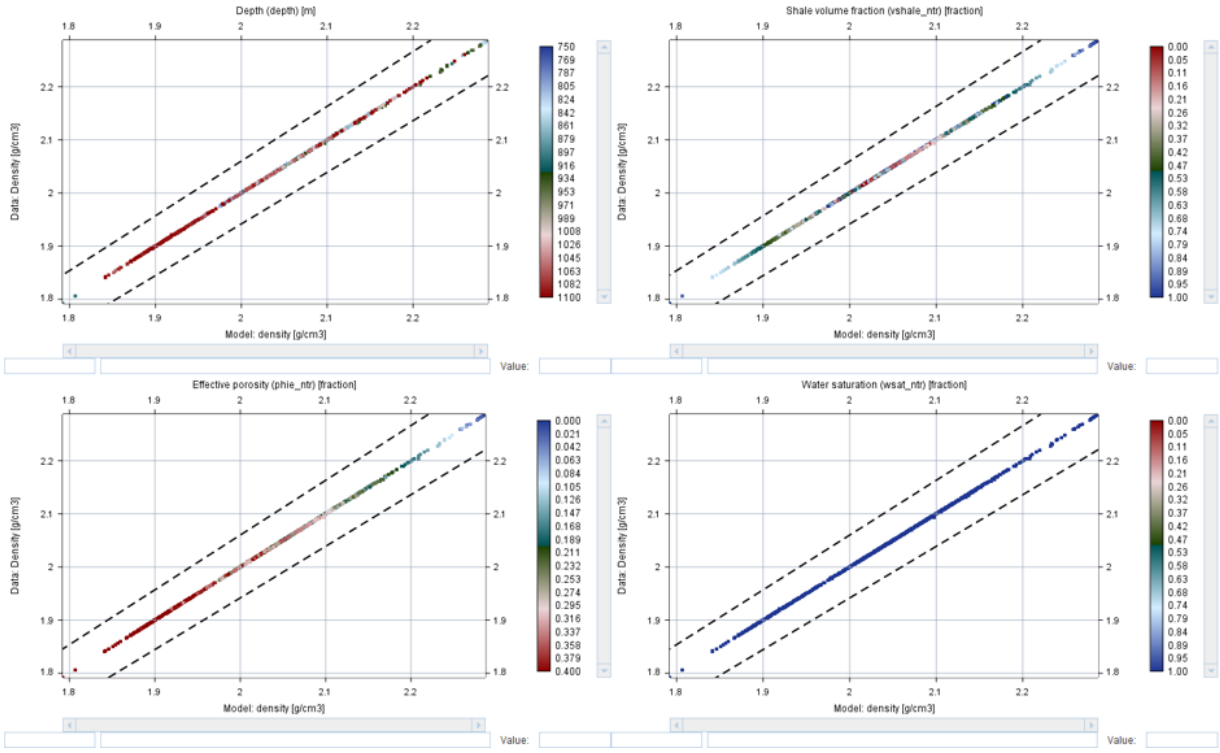

Shear Modulus:

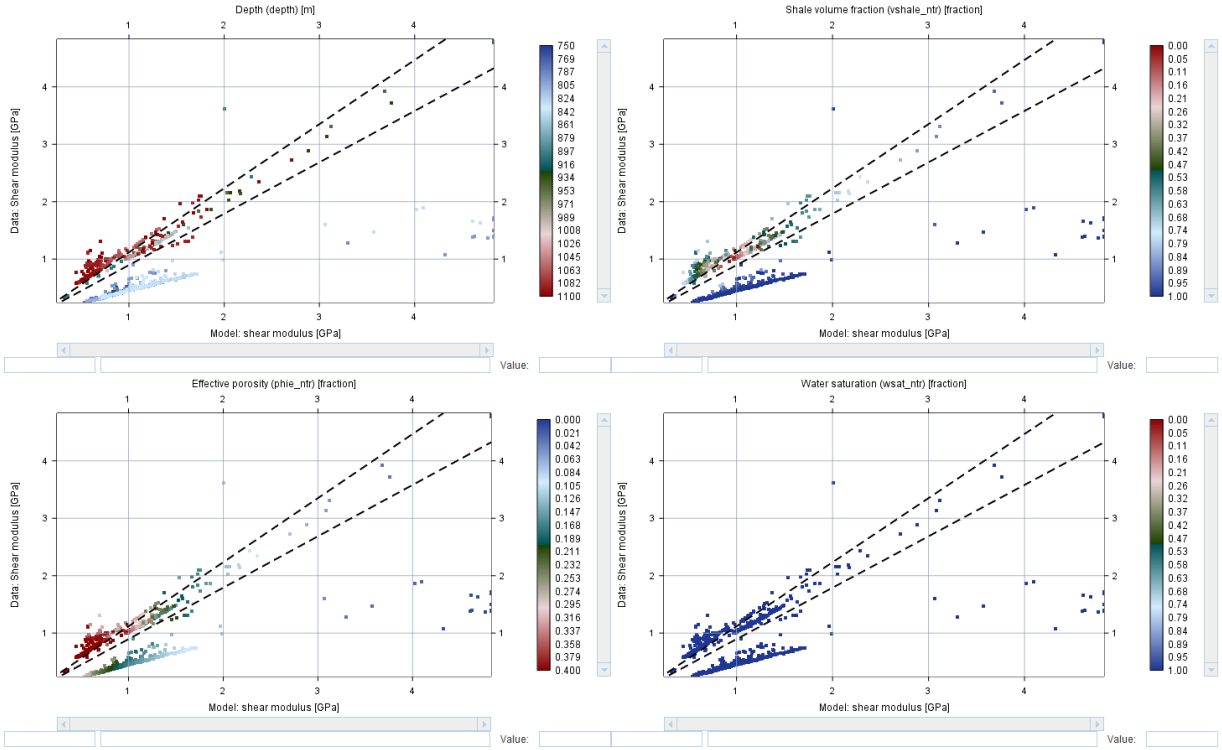

AVO RPT Input: